Wireless Communication with Medical Implants: Antennas and Propagation

Anders J Johansson

June 2004

Abstract

With the increased sophistication of medical implants, there is a growing need for flexible high-speed communication with the implant from outside the body. Today the communication is done by an inductive link between the implant and an external coil at a low carrier frequency. Extended range and communication speed are possible to achieve by increasing the carrier frequency and the bandwidth. One frequency band that is available for this application is the newly standardized 400 MHz MICS band, which has the benefit of being reserved mainly for medical and metrological applications. In addition, the 2.45 GHz ISM band is a possibility, but has the drawback of being heavily used by other applications, such as wireless computer networks and microwave ovens.

In order to assess the usability of wireless communication with medical implants, we have investigated the design of implantable antennas to be used in the body. Both theoretical limits and practical designs of the antennas are described. The SAR levels of the implanted antennas have been calculated and have been found to be at a safe level. We have investigated the wave-propagation from the implanted antenna to the outside, and its dependence on the position of the patient's limbs and the size of the body. Full wave 3D-simulations of the wave propagation are feasible, as the radio link between the patient and a base station placed in the same room is very short in terms of wavelengths in the MICS band. We have simulated the wave propagation in a furnished room and compared the results with measurements of the same room. The results from these investigations are evaluated in terms of their impact on the link budget for a prototype MICS system. From these calculations conclusions on the necessary complexity of the transceivers are drawn, such as the need for both spatial and polarization diversity to fully exploit the potential of the communication link.

Acknowledgements

Without a lot of people this thesis would never have come to be. To name you all and not to forget anybody is the hardest task I have in writing this thesis. It is not only hard, I think it is impossible.

I will begin with thanking You, the reader of this thesis. Most probably you are the one that, at one crucial point, gave me inspiration for yet another day of pushing the boundaries of knowledge a little bit further out.

But still a few have to be named.

I really must thank my advisors, Professors Anders Karlsson and Ove Edfors, for their time, patience and inspiration.

My master thesis students (in order of appearance) Luz Picasso Brun, Patrick Jansson, Martin Kvistholm, Vangel Cukalevski and Magnus Söderberg for making some of the more tedious parts of the research easier for me.

St. Jude Medical for their involment in the project and their financial support which made this project possible.

And here I could continue with a number of pages with names, but I will refrain. They would have included, in no particular order:

Everyone at the department. You have given ground support, companionship in despair and inspiration to go on. Thank you.

My family and all of my friends. Without whom I would never have finished this task. And even more important: not even started it. Thank you.

To be able to write a PhD-thesis is to have travelled along a long and winding road. To write the acknowledgement is to try to tell which stepping stones along the way that were the most important ones. Which is pointless, as they were all used.

Thank You All.
Anders J Johansson
Lund
May 2004

Preface

This research has been performed within the Competence Centre for Circuit Design at Lund University. It has also been supported by St. Jude Medical Inc. in Järfälla, Sweden. The work has been done in cooperation between the Radio Systems Group and the Electromagnetic Theory Group at the Department of Electroscience at Lund University.

My main contributions to the field are the investigations of antennas for medical implants, the simulations of the performance of such an antenna in different body shapes and arm positions, and the simulation, measurement and analysis of the spatially variation of the 400 MHz channel in an indoor environment. From these results, the link budget of a medical telemetry system can be estimated, and some conclusions about the necessary complexity of the system can be drawn. Furthermore, I have developed a hybrid model that facilitates the formulation of tissue simulating liquids. Other data is taken as common knowledge within the field, and is not referenced.

I have had great help from master thesis projects, which I have formulated, specified and supervised, and which have helped me carrying out some parts of the project.

Papers which are accepted or submitted :

- Johansson, A. and Karlsson, A. *"Wave-Propagation from Medical Implants - Influence of Arm Movements on the Radiation Pattern"*

  Proceedings of Radiovetenskaplig konferens (RVK'02), Stockholm, Sweden, 2002

- Johansson, A. J, *"Wave-Propagation from Medical Implants - Influence of Body Shape on Radiation Pattern"*

  Proceedings of the Second Joint EMBS/BMES Conference, Houston, TX, USA 2002.

- Johansson, A. J, *"Simulation and Verification of Pacemaker Antennas"*

  Proceedings of the 25th EMBS Conference, Cancun, Mexico 2003.

- Johansson, A. J, Picasso, L. B. and Jansson, L. J. P. *"Indoor Wave-propagation in the 403.5MHz MICS Band: simulations and measurements"*

  Submitted for publication. IEEE Transactions on Biomedical Engineering.

- Johansson, A. J, *"Comparison between the MICS Standardized Phantom and an anatomical Phantom"*

  Submitted for publication. IEEE Transactions on Biomedical Engineering.

- Johansson, A. J, *"Performance of a Radiolink Between a Base Station and a Medical Implant Utilizing the MICS Standard"*

  Submitted for publication. 26th EMBS Conference, SF, USA, 2004

Contents

Chapter 1

Introduction

The primary goal application of this research has been communication to the heart pacemaker. This is the most common active medical implant in use today. The pacemaker has a genuine need for communication, both for transmitting new settings to the pacemaker and to receive measurements and statistics from it.

1.1 The pacemaker

The first implantation of a self-contained heart pacemaker into a human was made by Åke Senning in 1958. He implanted a device, made and designed by Rune Elmqvist, into a patient[1]. This device worked for three hours and was replaced the next day by a new one, which worked for a week. The patient, Arne Larsson, survived these first tests and lived for another 43 years, having then received a total of 23 different pacemakers in his life [2]. An updated version of the pacemaker was implanted into a patient in Uruguay in February 1960 [1]. This device still worked when the patient died of infection after 9 1/2 months[2]. At the same time another self-contained pacemaker was developed by W. Greatbatch in USA [3]. This design used non-rechargable batteries, contrary to the Elmqvist design. Greatbatch did the first animal experiments in May 1958 and the first human implantation in April 1960 [3]. Today fabrication of pacemakers is an industry with a market of over 600.000 units per year [3]. The pacemakers have been developed so that they not only are able to correct heart block and arrhythmias, but also, in some versions, are able to defibrillate the heart and thus move it from a life threatening state to a normal one [4].

The modern pacemaker mainly consists of two parts: a main unit and one or more leads. The main unit contains the battery, electronics for pulse forming and sensing of the heart, and also other sensors and communication means. The lead is attached to the main unit and carries electrical signals to and from the heart. The lead may contain one or more electrical wires inside, and the pacemakers usually use one or two leads. The main function of the pacemaker

is to make the heart beat in an orderly fashion. To accomplish this it senses the existing electrical activity, if any, in the heart and generates electrical impulses to make the heart beat, if the spontaneous activity is absent.

1.2   Existing communication methods

There is a need for communication with the pacemaker from the outside. Different operating parameters of the pacemaker may be changed, and diagnostic data may be read out from the pacemaker. The advances in memory technology also make it probable that future pacemakers will store larger amounts of data to be transferred to the treating physician.

Today the communication is achieved over an inductive link. A small coil is placed inside the case of the pacemaker, and a larger coil is placed upon the chest of the patient, directly on top of the pacemaker. The inductive coupling between these two coils is then used to transfer data to and from the pacemaker. The link is usually at half-duplex (only in one direction at any one time). The speed is typically low, an example given in [4] is at 512 b/s. Higher speeds are achievable, but the low carrier frequency limits the available data bandwidth severely.

1.3   Radio communication

There are a number of advantages if the communication with the implant can be moved to a higher carrier frequency. The first one is an increase in bandwidth, which makes it possible to achieve a higher bitrate. The second one is that a higher frequency gives rise to a propagating electromagnetic wave, which makes the system usable at longer ranges. A longer communication range makes a number of new user scenarios possible. A couple of examples of these will be described here:

1.3.1   Hospital checkup

A pacemaker patient returns regularly to the hospital for checkups, where his status and the status of the implant are checked. Today the patient has to be still for some time in order to place the external coil on top of his pacemaker, and to read the status information. If the parameters of the pacemaker need to be changed the procedure has to be repeated.

If, instead, the communication with the pacemaker is done with RF technology and over a range of a couple of meters, the data from the patient can be read already while the patient is waiting in the lounge. When the patient enters the doctor's office, the data is already present on the computer screen of the receiving station. In this case the readout can be done during a couple of minutes, allowing for lower bit rates. If only a shorter operating range is achieved, the readout can be made in the physicians office, while the patient tells about his wellbeing.

1.3.2 Home care

Some patients may require more frequent checks than can be made practically at the hospital, for instance once every day. Then a home care unit can be placed in the patient's home. The unit communicates with the medical implant and can be connected to the telephone system, or the internet, and send regular reports to the physician at the hospital. The inductive technology is not well suited for the home care situation since the patient must place the coil fairly accurately and keep it there for some period of time. RF technology would instead make it possible to have the patient sitting in a chair facing the home care unit and pressing a button for the data link to be set up. The home care unit could be placed at the bedside table and read data every night when the patient is sleeping, and make the surveillance more convenient. In an extension this can be used for continuous monitoring of patients. However, that would require either a very energy efficient transfer mode, or an intelligent pacemaker that only uses the wireless communication link to send alarms and data when needed.

1.4 Telemedicine

Telemedicine is defined as the use of telecommunications to provide medical information and services [5]. The home care system described above goes within this definition. One example of this is the Biotronic Home Monitoring® System where the pacemaker transmits statistics to a small external unit that can be worn at the belt [6]. This unit is also equipped with a GSM telephone and relays the data to the physician's office. The data transfer is unidirectional, and is thus not a full implementation of the MICS standard, but it uses the same frequency band.

The use of continuous monitoring of pacemakers is illustrated by the company PDSHeart, whose main business is to connect patients at home with their physicians. The data transfer from the pacemaker is probably done by an inductive link, and the data is uploaded by the wired telephone network. It is easy to visualize the added benefit by using a (relative) long-range wireless transfer mode from the pacemaker.

1.5 Other implants

Today there is a number of other implants in use and in development. Examples are brain pacemakers for treatment of Parkinson's decease [7], implantable drug pumps [8], cochlea implants [7], artificial eyes [7], muscle stimulators [7] and nerve signal recorders for use with robotic prostheses [9].

All of these implants need some kind of data transfer, either in one or in two directions. Neither inductive nor RF is the best for all of them as the power requirements; range and speed differ between the different applications. However, for some of them an RF link would give the same advantages as it

does to the heart pacemaker. One example is that the remote controls for contemporary brain pacemakers must be placed on top of the implant, which is placed in the chest with a lead leading to the brain, in order to work [8].

1.6   Percutaneous connections

A possible solution to the problem with the low bandwidth of the inductive link is to use a percutaneous electrical connector, i.e., a connector that goes through the skin of the patient. Such a connector can easily be envisioned to be able to sustain transfer speeds in the Gb/s range. The problem with percutaneous connectors is that they make a pathway for infections to enter into the body, and then follow the implanted leads to, for example, the brain. What is needed is a material to which the skin will adhere and grow into, thus making the connector an integral part of the skin itself. To our knowledge, no such connector exists today. Percutaneous connectors are used in research applications [10].

Chapter 2

Communication Methods

There are different technologies possible for wireless communication with an implanted object. In this chapter, we present the main methods, and describe their function.

2.1 Electromagnetic methods

Today an electromagnetic link is used between the implanted pacemaker and an external programmer. The pacemaker incorporates a small coil inside the closed metal housing. An external coil is placed on the chest of the patients, on top of the implanted pacemaker, as in Figure 2.1. The two coils are inductively coupled to each other, since they are colinear. The inductive coupling serves as the communication channel.

The communication link uses 175 kHz as the carrier frequency and transmits data at a speed of up to 512 kb/s [4]. The range of communication is in principle constrained to "touch" range, where the external coil housing must touch the patient's chest. The placement of the external coil is often guided by indicators on the external coil, as the link is sensitive to the position of the external coil. This makes the procedure time consuming. At these low frequencies the magnetic field is more or less unaffected by the case of the implant and by the body. Thus, the field couples through the case of the pacemaker so that the coil of the pacemaker can be mounted inside the case. The attenuation in the
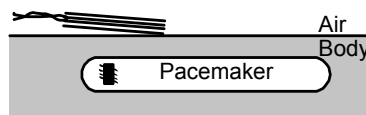

Figure 2.1: Illustration of a pacemaker with an internal telemetry coil and an external coil, which communicate by inductive coupling.

Material	σ_e (S/m)	Skin Depth δ		
		170 kHz	403.5 MHz	2.45 GHz
Copper	5.8×10^7	280 μm	5.8 μm	2.4 μm
Titanium	2.3×10^6	800 μm	16 μm	6.7 μm
Water	[11]	13 m	0.87 m	0.024 m
Seawater	$\sigma_{DC} = 5$,[11]	0.6 m	0.013 m	0.007 m
Muscle Tissue	0.37/0.79/1.74 [12]	2.2 m	0.052 m	0.022 m

Table 2.1: Calculated skin depths. The values for destilled water, seawater and muscle tissue are found in the references given in the table.

case is related to the skin depth in the material. The skin depth is the depth at which the electric field has been attenuated by a factor of e^{-1} or 0.368. This is often calculated as

$$\delta = \sqrt{\frac{2}{\omega \mu \sigma_e}} \qquad (2.1)$$

where σ is the conductivity of the material and μ is the permeability. Equation 2.1 is only valid for good conductors, where $\sigma/\omega\varepsilon \gg 1$. This will not be true for all of the materials discussed in this thesis. The skin depth is defined by calculating the attenuation as $e^{-\alpha z}$, where α is the attenuation constant. In Equation 2.2 the general form of the propagation constant γ is given.

$$\gamma = \alpha + j\beta = j\omega\sqrt{\mu\varepsilon_e}\left(1 + \frac{\sigma_e}{j\omega\varepsilon_e}\right)^{1/2} \qquad (2.2)$$

The permeability μ, the permittivity ε_e and the conductivity σ_e are discussed in Section 4.1.1. As α is the real part of γ, we generalize the expression of the skin depth to

$$\delta = \frac{1}{\alpha} = \frac{1}{\text{Re}\,[\gamma]} \qquad (2.3)$$

Equation 2.3 can be solved numerically and the results are given in Table 2.1. The permeability of vacuum $\mu_0 = 4\pi \times 10^{-7}$ Vs/Am is valid for most of the materials presented here. The case should be thinner than the skin depth in order not to reduce the coupled energy too much. The fact that the low frequency fields penetrate the case is advantageous in the sense that it minimizes the number of electrical wires, which have to be routed from the inside to the outside of the case. The main drawback of the inductive link is that the low frequency limits the available bandwidth and this results in a low data rate. The external coil must be placed fairly accurately in order to get a reliable link. This adds to the complexity of the communication procedure. The dielectric data for water is calculated using Equation F.2 in Appendix F, with data from [11] for 403.5 MHz and 2.45 GHz.

2.2 MICS standard

The European Telecommunications Standards Institute (ETSI)[13] has stan-
dardized the Medical Implant Communication System (MICS) in [14]. The
ETSI document lists two principal fields of application for the standard. The
first one is for telecommunication between a base station and an implanted de-
vice. The second one is for telecommunication between medical implants within
the same body. The standard does not explicitly mention the third possible use:
telecommunication between medical implants in different bodies. This applica-
tion is today fairly farfetched but there are possible applications, such as mesh
networking in order to increase the effective communication range.

The frequency band allocated is 402 MHz to 405 MHz. The maximum
emission bandwidth to be occupied is 300 kHz. The maximum bandwidth is
for the complete session. If the system uses separate frequencies for up- and
down-link, the two link bandwidths must not add up to more than 300 kHz.
This implies that in order to get high data throughput a half-duplex scheme
should be adopted, where only one device transmits at a time. If full duplex
is necessary, the available bandwidth for each direction will be less, and this
implies a lower data bandwidth for each direction. Note that in the case of
a half duplex solution the up- and down-link do not have to share the same
frequency band. Separate RX and TX bands, each with a bandwidth of 300
kHz, may be used as long as they are not used simultaneously.

The 300 kHz bandwidth is an emission limit: the power at the band edges has
to be 20 dB below the maximum level of the modulated output. The resolution
bandwidth of the measurement should be 1 % of the emission bandwidth of
the device under test. The maximum power limit is set to 25 μW Equivalent
Radiated Power (ERP), i.e., the maximum field-strength in any direction should
be equal to, or lower than, what a resonant dipole would give in its maximum
direction at the same distance, with the dipole being fed with a signal of 25 μW.
This is to be measured with the medical implant inside a human torso simulator,
described later in this thesis. There is some confusion about the power level.
The ITU-R recommendation [15] sets a level of 25 μW Equivalent Isotropic
Radiated Power (EIRP), which equals a level 2.2 dB lower than the ERP level
set in the ETSI MICS-standard. The FCC in the USA has set the limit to
EIRP=25 μW [16], and the same level is proposed for Australia [16]. We have
used the lower level of EIRP=25 μW, or EIRP=-16 dBm, for the calculations
in this thesis.

The MICS standard test procedure for measuring the ERP from the implant
placed in the torso simulator discusses two cases. In both cases the implanted
device is mounted on a plastic grid , either in a horizontal or in a vertical
position. It is not clear from the text in the standard document when the second,
vertial, position is to be used. We have interpreted the test case as to orient
the implant as it will typically be placed in a patient. There is no simulator
standardized for implants primarily used in arms, head or legs. According to
the standard, all implants, regardless of their final position in the body, should
be tested in the same torso simulator.

The frequency band specified for MICS is already in use. The Meteorological Aids Service (METAIDS), which primarily is used by weather balloons transmitting data down to the earth, uses the same spectrum allocation today. For this reason the MICS system is specified to be used only indoors.

2.3   2.4 GHz ISM band

The 2.4 GHz ISM-band is a potential band to be used for medical implant communication. It is the same band that is used today by a variety of services, e.g., WiFi and Bluetooth, both used by computer equipment. In addition, cordless telephones and household microwave ovens operate in this frequency band.

According to ETSI EN 300 328 [17], the maximum EIRP is -10 dBW (100 mW). The system should be spread spectrum, either Frequency Hoping Spread Spectrum (FHSS) or Direct Sequence Spread Spectrum (DSSS). In the case of FHSS, at least 15 separate non-overlapping channels should be used. In the case of DSSS, the maximum power density is -20dBW/MHz EIRP. The frequency band available is from 2.4000 GHz to 2.4835 GHz.

The test protocol described in EN 300 328 is not intended for implanted devices. As an example the protocol states that the batteries should be removed during testing, and have the device run from a test power source. This is very hard to implement in a pacemaker that is welded airtight during the manufacturing process. Neither is any provision given for a human phantom of any kind.

One disadvantage with this band is that it is shared with all the other users of the same band. This places great demands on inter-operability and security. The penetration into the human body is also less than at 400 MHz. From Table 2.1 we find that the generalized skin depth is only 22 mm compared to 52 mm at 400 MHz.

2.4   Acoustic link

It is possible to communicate with medical implants by means of acoustic waves. Remon Medical uses ultrasound communication in order to read out data from an implanted sensor [18][19]. The sensor is powered by the incoming ultrasound energy. The use of acoustic waves is a well-known method for communication, and has been used by the oil industry for some time. The communication between the drill head at the bottom of the hole and the surface is done by modulating the pressure of the returned water from the drill head [20].

Acoustic transmission of information from medical implants has been used previously in pacemakers; an example is that some pacemakers have had an alarm buzzer that gave an audible warning to the patient in the case of low battery voltage. Also some ICDs use acoustic beeps for communicating the status of the device [21].
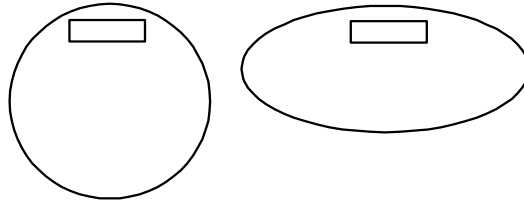
Figure 2.2: Illustration of the influence of the curvature in the MICS phantom on the distance to the edge of the phantom.

2.5 Optical link

An optical link is conceivable since skin and tissue have a low, but nonzero, transmission of visible light. Communication to an implant that is placed close to the skin could be possible. Transmission out from the implant might be prohibitive in terms of power. In both cases, the outside transceiver probably has to be placed very close to the patient.

2.6 Phantoms

In order to test the adherence of an implantable communication system to a standard, some kind of physical human torso simulator is necessary. Testing of systems in humans is not practical in development work. Furthermore, it is ethically questionable, especially if used for technical testing and development of small subsystems[22].

The MICS standard defines a physical phantom. This is an acrylic plastic cylinder with a diameter of 30 cm. The wall thickness should be 0.635 cm (=1/4 inch). It is to be filled with tissue simulating liquid to a height of 76 cm. The medical implant should be placed on a plastic grating at a height of 38 cm inside the cylinder, and at a distance of 6 cm from the sidewall. Any flexible antenna from the implant should be placed along the wall at the same height and distance. Other wires should be coiled and placed adjacent to the implant. Our interpretation is that the implant should be placed on the grid in the same orientation as it would be in a human torso, i.e., the pacemaker model is placed standing on its edge.

The advantage of using such a simple phantom as the MICS phantom is that it is easy to build, manage and use. The drawback is that it is not very anthropomorphic. It resembles the chest of a human, but it has a constant curvature, in contrast to the human who is mostly flat on the front and back sides. One consequence of this is that a flat implant will be closer to the wall of the phantom at the edges, whereas the same implant in a human would have the same distance to the skin over the whole side that is closest to the skin. The difference is illustrated in Figure 2.2.

The specification that the implant should be placed 6 cm from the sidewall of the phantom reduces this problem, but introduces a discrepancy between the placement in the phantom and the placement in an actual implantation. In the case of pacemakers, the implant is most often placed subcutaneously between the fat and the pectoral muscle beneath the collar bone. This gives an implantation depth of between 0.5 cm and 8 cm, depending on the patient [23]. In the phantom the implant is placed deeper, and this introduces a larger loss to the signal due to the lossy nature of the tissue simulating liquid. Since the MICS standard is written in order to guarantee non-interference with existing users of the same part of the frequency spectrum, this may be an issue. It might be that all the actual implanted cases will have a higher EIRP than is measured in the type approval procedure. Another drawback with the specified MICS phantom is that it only roughly models the chest of a *male* human. The female anatomy is not modelled accurately.

There are medical implants placed at other positions in the body that also can benefit from an RF communication link. Examples are cochlea implants, which are typically mounted on the scull subcutaneous above the ear dwith an electrode going to the cochlea, and myoelectric sensors for control of prostheses, which probably will be mounted inside the residual muscles controlling the missing limb [9]. The existing MICS phantom models these other implantation sites very poorly, and gives erroneous results for the EIRP.

For development work the phantom has the disadvantage of not incorporating any fat or skin layer. The electromagnetic properties of fat are very different from those of muscle and skin. This implies that the thickness of the fat layer influences the properties of a subcutaneous placed antenna. This is investigated in more detail in Chapter 4. With regard to phantoms for development, a changeable fat layer would be suitable in order to evaluate its influence on the antenna parameters. A good antenna should work within some given specification, regardless of the thickness of the fat layer. In the literature there are recipes for tissue simulating liquids for muscle, brain, lung and bone tissue [24]. There are also descriptions of polyacrylamide solutions, which simulate fat tissue, but only at lower frequencies [25]. In an ongoing project, we are developing recipes for simulated fat tissue and skin tissue, preferable in a semi-rigid form such as a latex material. These recipes are not finalized at this moment. With these additional tissues more advanced phantoms may be designed. We propose a layered phantom to test how antenna characteristics depend on the thickness of the fat layer. It consists of a container with a square cross-section of 50 cm x 50 cm and a height of 40 cm. The container is filled to a height of 40 cm with a liquid simulating human muscle tissue. On top of this, a dielectric material is placed that simulates the fat layer, and on top of that, another dielectric material is placed, simulating skin. The medical implant to be tested can be placed in any of the tissues, or at any of the interfaces between them. The edge of the fat layer needs to be lined with an absorber, as in Figure 2.3, in order to reduce the effect of the resonator that it will otherwise form. The relatively large size of the phantom is due to that it should be several wavelengths long. The wavelength of 400 MHz in the muscle tissue is approximately 9 cm.
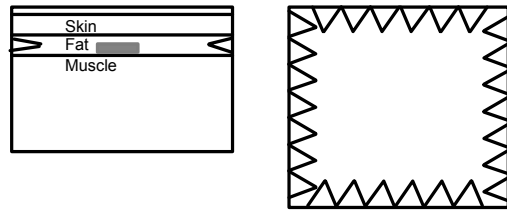
Figure 2.3: Illustration of the side and top view of the proposed flat phantom. The sawtooth edge illustrates the necessary absorption material in the fat layer. The grey box illustrates the implant to be tested.

Chapter 3

Link Budget I

In this chapter we take a first look at a link budget for the MICS system. The link budget provides the framework for the research presented in this thesis, where we have investigated and refined the various assumptions. In Chapter 8 we return to the link budget and repeat the calculations with the results from our investigations.

3.1 Fading

The general definition of *fading* is that it is the variation, of the field strength at the receiver position, over time[26]. The path loss between the implant and the base station will vary with the patient and with the surroundings. Reflections against the walls, floor, ceiling and other surfaces in the room give rise to a standing wave pattern in the room. The gain of the implant antenna is not isotropic but varies in different directions. Thus, variations will be found between different patients, consultations and also during one consultation if the patient moves during the transmissions. The variations of the path loss constitute different types of fading when they occur over time [26], as is the case with patient movement. These variations are investigated in the following chapters.

3.2 ITU-R

The International Telecommunication Union has discussed the interference issues between MICS and the Meteorological Aids Systems (Metaids) in the document ITU-R SA.1346 [15]. It includes a link budget calculation for a MICS system. The purpose of the calculations is to show that the MICS system works when operated at power levels that minimize the risk of the Metaids system being disturbed by harmful interference. An overview of the link budget is given in Table 3.1.

Uplink from implant	ITU-R	Maximum from MICS
BW	200 kHz	
TX Power	-2 dBm	15.5 dBm
Antenna Gain	-31.5 dBi	
EIRP	-33.5 dBm	-16 dBm
Free Space Loss 2m	30.5 dB	
Fade Margin	10 dB	
Excess Loss	15 dB	
Base station antenna gain	2 dBi	
Received power at base	-87 dBm	-69.5 dBm
Receiver noise at input	-101 dBm	
Downlink to implant	**ITU-R**	**Maximum from MICS**
BW	25 kHz	
TX Power	-22 dBm	-18 dBm
Antenna Gain	2 dBi	
EIRP	-20 dBm	-16 dBm
Free Space Loss 2m	30.5 dB	
Fade Margin	10 dB	
Excess Loss	15 dB	
Body antenna gain	-30.5 dBi	
Received power in body	-106 dBm	-102 dBm
Receiver noise at input	-121 dBm	

Table 3.1: Link Budget from ITU-R document

3.2.1 Uplink

The bandwidth in the ITU-R calculations is 200 kHz. The maximum available bandwidth in the MICS standard is 300 kHz. The benefit of using a lower bandwidth is that the noise into the receiver is lower. The thermal noise power is proportional to the bandwidth [27] as

$$N = kTB \qquad (3.1)$$

where the Boltzmann constant $k = 1.38 \times 10^{-23}\,\mathrm{J\,K^{-1}}$, T is the absolute temperature in Kelvin, and B is the effective noise bandwidth, which is approximately equal to the modulation bandwidth. The unit of N is then (W).

The transmitted, or TX, power from the implant is set to -2 dBm, or 600 μW. The TX power level is not directly given by the MICS standard. It depends on the results from the link budget calculations, and on the available power from the battery and the performance of the circuitry. The only limit is that the EIRP must be below the maximum power set in the MICS standard. The gain from the implant antenna is set to -31.5 dBi. Together this gives an EIRP of -33.5 dBm, which has a margin of 17.5 dB to the MICS standard. A plausible reason for this margin is that a low output power from the implant has been chosen in order to conserve the battery in the implant.

The path loss is taken as free space loss, which equals 30.5 dB for a path length of 2 m. This model for wave propagation is very simple. Strictly, it is only valid for a transmitter and a receiver far away from each other (=far field conditions) in an infinite empty space. Communication between two satellites is a practical example of where it is a good model. The model is shown in Equation 3.2, where λ is the wavelength and d is the distance between transmitter and receiver.

$$\mathit{Free\ Space\ Loss} = \left(\frac{\lambda}{4\pi d}\right)^2 \qquad (3.2)$$

In addition to this theoretical path loss a fading margin of 10 dB is given. An additional factor, representing excess losses, is then added. This is supposed to include patient orientation, antenna misalignment, non-line of sight conditions and polarization loss. The fading loss and the excess loss factors have been thoroughly investigated in our research.

The gain of the receiver antenna at the base station is set to +2 dBi, corresponding to a dipole antenna. (The dipole antenna has a theoretical gain of +2.15 dBi [28].) This gives a total received power at the input of the base station of -87 dBm. The noise level at the same point is calculated as a received noise level of +20 dB over the thermal noise floor, and added to that the noise figure of the base station receiver, which is set to 4 dB.

3.2.2 Downlink

The parameters for the downlink to the implant are similar to the ones given for the uplink. One difference is that the bandwidth is given as 25 kHz. No

reason for the reduced bandwidth is given. The communication to the implant is often limited to the updating of a few operating parameters[4]. Thus, a reduced communication speed is acceptable, which would mitigate the impact of the higher noise figure given for the implanted receiver. In the calculations this noise figure is set to 9 dB. Furthermore, the output power from the base station is given as -22 dBm. This gives an EIRP of -20 dBm, or 10 μW. In [15] it is explained that an additional margin has been chosen in order to guarantee interference-free operation together with the Metaids devices.

The proposed link budget uses FSK modulation, of unspecified type, in both uplink and downlink. If we assume coherent FSK, the corresponding bitrates become approximately 200 kbit/s up from the implant and 25 kbit/s down. This is taken with an efficiency of 1 bit/s/Hz [29].

3.2.3   Discussion

Most of the numbers in the ITU-R link budget are given without any references. Critical ones are the gain of the implanted antenna and the indoor wave propagation characteristics at the MICS band, as these are non-classical. We have concentrated our research on clarifying these points. The link budget also includes two added margins in order to guarantee the performance of the link: a fading margin and an excess loss parameter. These are in the ITU-R document given without any further references. We have tried to quantify the variations of the path loss to see if the given margins are at realistic levels. The definition of fading includes a variation over time. As this will depend on the movement of the patient and other objects, and as the speed and the frequency of these movements have not been studied by us, we prefer to give the values as excess losses. These have to be included in the link budget in order to have a corresponding coverage.

The noise performance of the receivers is dependent on the chosen technology and the amount of current that is available from the power supply. This depends on design criteria such as operating environment, price, size, estimated lifetime etc. These choices are essential when designing a product, but in absence of a definitive design, we can only make educated guesses on these numbers. They are, therefore, not the primary focus of this investigation.

Chapter 4

Wave Propagation into Matter

It is known that an object onto which an antenna is attached influences the performance of the antenna. If the antenna is covered in order to protect it from the environment, for example with a radome, this will also affect the performance. Accordingly, when we insert an antenna into an object, such as is the case with a medical implant with an antenna inserted into a patient, we cannot separate the antenna from the surrounding object. When we study its performance, we cannot separate the antenna from the object to which it is attached nor from its radome. This requirement is only loosened if the wavelength is much shorter than the size of the object, where we then only have to include the parts of the object that are close to the antenna. It follows that the body covering the implanted antenna has to be accounted for when evaluating the far field radiation characteristics of an antenna operating in the MICS band. At 403.5 MHz the wavelength in air is 0.74 m and about 0.09 m in the body. In a sense, the body will be a very large, lossy, non-stationary radome which extends all the way from the absolute near zone of the antenna to, at least in some directions, the far zone. Thus, we cannot discuss or design the antenna without investigating the electromagnetic properties of the body. For the same reason we cannot evaluate the absolute influence of the body without discussing a certain antenna implementation.

We start by investigating the case of a plane wave incident onto a human body. There we can study the available electric and magnetic fields inside the human body. Their amplitude and phase are dependent on the frequency and the structure of the body.

4.1 Maxwell's equations

The basis for antenna design and wave propagation is Maxwell's equations. We have used the following frequency domain formulation:

$$\bigtriangledown \cdot \vec{D} \;=\; \rho \tag{4.1}$$

$$\bigtriangledown \cdot \vec{B} \;=\; 0 \tag{4.2}$$

$$\bigtriangledown \times \vec{E} \;=\; -j\omega \vec{B} \tag{4.3}$$

$$\bigtriangledown \times \vec{H} \;=\; \vec{J} + \vec{J}_s + j\omega \vec{D} \tag{4.4}$$

Here $\vec{D}$ is the electric flux density, $\vec{E}$ is the electric field, $\vec{B}$ is the magnetic flux density, $\vec{H}$ is the magnetic field, ρ is the charge density and $\vec{J}$ is the current density. $\vec{J}_s$ is the added source current density on the antenna. Only linear isotropic materials are considered, and thus the constitutive equations read:

$$\vec{D} \;=\; \varepsilon \vec{E} \tag{4.5}$$

$$\vec{H} \;=\; \frac{\vec{B}}{\mu} \tag{4.6}$$

$$\vec{J} \;=\; \sigma \vec{E} \tag{4.7}$$

The permittivity, ε, the permeability, μ, and the conductivity, σ, are in general complex and frequency dependent.

In an infinite homogenous space the electric field at radius r from an antenna can be obtained by solving Maxwell's equations for $\vec{E}(\vec{r})$ [30]:

$$\vec{E}(\vec{r}) = -j\omega\mu \left(\overline{I} + \frac{1}{k^2} \bigtriangledown \bigtriangledown \right) \cdot \iiint_V \frac{e^{-jk|\vec{r}-\vec{r}'|}}{4\pi |\vec{r}-\vec{r}'|} \vec{J}_s(\vec{r}') \, dv' \tag{4.8}$$

where $\overline{I}$ is the identity operator, i.e., $\overline{I} \cdot \vec{J} = \vec{J}$. Furthermore, r is the distance from the antenna, V is the volume containing the antenna and k is the complex wavenumber defined as

$$k = \omega\sqrt{\mu\varepsilon_c} \tag{4.9}$$

where ε_c will be defined in Equation 4.12. This formula is useful if we know the currents in the volume V. The solution is valid even if the medium is lossy, i.e., for complex wavenumbers k. In most cases the currents are not known $a\ priori$ and numerical methods, e.g., finite difference time domain (FDTD) or method of moments (MoM), must be used to calculate the electric field from a certain implementation.

4.1.1   Matter

In order to investigate the design of implanted antennas for higher frequencies we need to define the electromagnetic properties of the materials. Classical antenna theory mainly deals with antennas placed in vacuum or in air. That is, antennas that are placed in a non-conducting environment with a permittivity of $\varepsilon_0 = 8.854 \cdot 10^{-12} \,\mathrm{F\,/\,m}$. When we place the radiating structure in a material

with a higher permittivity, and with non-zero conductivity, some of the classical theory must be revisited in order to revise the usual simplifications used in antenna design.

The permittivity ε and the conductivity σ are defined in Equation 4.5 and 4.7. They are, in the general case, complex quantities that are expressed in their real and imaginary parts as

$$\varepsilon = \varepsilon' - j\varepsilon'' \tag{4.10}$$
$$\sigma = \sigma' - j\sigma'' \tag{4.11}$$

The complex permittivity ε_c of a medium is then defined as

$$\varepsilon_c = \varepsilon_e - j\frac{\sigma_e}{\omega} \tag{4.12}$$

Here the effective permittivity ε_e and the effective conductivity σ_e are defined as

$$\varepsilon_e = \varepsilon' - \frac{\sigma''}{\omega} \tag{4.13}$$
$$\sigma_e = \sigma' + \omega\varepsilon'' \tag{4.14}$$

The permittivity ε_e is often scaled with the the permittivity of vacuum $\varepsilon_0 = 8.854 \cdot 10^{-12}$ as in

$$\varepsilon_{er} = \frac{\varepsilon_e}{\varepsilon_0} \tag{4.15}$$

The loss due to conductivity in the matter is often expressed as a dissipation factor $Diss$ or a loss tangent $\tan\delta$. They are defined as

$$Diss = \tan\delta = -\frac{\mathrm{Im}\,[\varepsilon_c]}{\mathrm{Re}\,[\varepsilon_c]} = \frac{\sigma_e}{\omega\varepsilon_e} \tag{4.16}$$

where $\mathrm{Re}[]$ and $\mathrm{Im}[]$ denote real and imaginary part, respectively.

4.2 Material data and measurements

When we measure the permittivity of a material, we get the complex permittivity ε_c. By measuring only at a single frequency we cannot separate the conductivity $\frac{\sigma}{\omega}$ from the lossy imaginary permittivity ε''. Measurement probes, such as the Agilent 89010, only give the real part ε_{er} and the loss tangent $\tan\delta$.

The imaginary parts of ε and σ are due to time lags in the electromagnetic response of the materials [31]. Specifically, ε'' is due to the polarization response of the material and σ'' is mainly due to time lag in the conduction response caused by large ions.

4.2.1   Tissue data

The effective permittivity ε_{er} and conductivity σ_e of different human tissues that are relevant for medical implants are given in Table 4.1. All data is given for a frequency of 403.5 MHz and are from [12]. Notice that fat tissue is markedly different from both skin and muscle tissue in that it has a much lower permittivity and conductivity.

Tissue	ε_{er}	σ_e (S/m)
Muscle	57.1	0.797
Fat (non infiltrated)	5.6	0.041
Lung	23.8	0.375
Skin (dry)	46.7	0.690
Skin (wet)	49.8	0.670
Bone Cancellous	22.4	0.235
Brain grey matter	57.4	0.739
Brain white matter	42.0	0.445

Table 4.1: Dielectric parameters for human tissue at 403.5 MHz

4.2.2   Simulated Tissues

In order to test antenna performance of an implanted antenna in the lab, we make use of tissue simulating liquids. These are the same as those used for measurement of the specific absorption rate (SAR) in evaluation of mobile handsets. The MICS standard references an article [24] in which four different materials are defined. These are recipes for making tissue-simulating liquids representing muscle tissue, brain tissue and lung tissue. In addition, a recipe for making a material simulating bone suitable for casting is given. The recipes for muscle and brain tissue simulations are summarized in Table 4.2. HEC is the short name for Hydroxyethylcelloluse, which is an inert substance that absorbs water and increases the viscosity of the solution. Details on how the different substances influence the electromagnetic properties of the mixture are given in Appendix F.

By comparing Table 4.1 and Table F.1 we see that there are differences in the values. In the simulations presented in this thesis, values have been used from either of the two tables depending on what is being investigated. If the object of interest is the behavior of the design in an actual human, the data given by Gabriel was used. If comparisons with measurements in the physical

Tissue	Water	Sugar	Salt (NaCl)	HEC
Muscle	52.4%	45.0%	1.4%	1.0%
Brain	40.4%	56.0%	2.5%	1.0%

Table 4.2: Recipies for tissue simulating liquids.

Material	ε_{er}	σ_e(S/m)
Muscle	62.5	0.9
Brain	50.3	0.75

Table 4.3: Permittivity and conductivity at 403.5 MHz for the simulated tissue materials used in this thesis.

phantom were involved, the synthetic material data was used.

4.3   One-dimensional FDTD simulations

The simplest model of the human body is the following: the body is modelled as a block of muscle tissue with a certain thickness, and extending to infinity in the other two dimensions. By this simplification, we are able to simulate the influence of tissues such as skin, fat and muscle by an efficient one-dimensional FDTD analysis (for a description of FDTD see Appendix D). The results in this section are for the MICS mid band frequency of 403.5MHz, and the corresponding tissue parameters are given in Table 4.1.

The interesting phenomena to investigate are the behavior of the electric and the magnetic components of the electromagnetic field when a plane wave meets simplified body models. Figure 4.1 shows the magnitude of the electric and the magnetic field, normalized with the incoming plane wave amplitude. The surface of the body slab was placed at 1.000 m and the thickness of the slab was 144 mm, which is the thickness of a human body at the level of the fourth vertebrae, taken from [32]. The well known, cf. [33][34], node of the electric field and the anti-node of the magnetic field on the outside of the body are clearly visible. This is one of the reasons why pagers often use magnetic antennas oriented perpendicular to the body [34]. Inside the body block, we have a dominating propagating wave which is attenuated due to the conductivity of the muscle tissue. The magnetic field is strengthened at the surface between the body block and the air, which implies that a magnetic antenna may be beneficial also for pacemaker applications. The pacemaker is implanted close to the skin, typically between the subcutaneous fat tissue and the major pectoralis muscle at the chest, just below the collarbone.

A more complex model was simulated in order to investigate the influence of the fat layer between the skin and the muscle layer. Simulations were done with the same body block as in Figure 4.1, but now with a fat layer and a cover of 3 mm skin on each side. Simulations were done with fat layers of thicknesses 0, 5, 10, 25 and 50 mm. The resulting E and H plots are shown in Figure 4.2 and Figure 4.3. There is a dependence on the thickness of the fat layer, but in these simulations the variation is not larger than 2 dB at the interface between the fat layer and the muscle tissue, which is the probable placement of the pacemaker antenna.

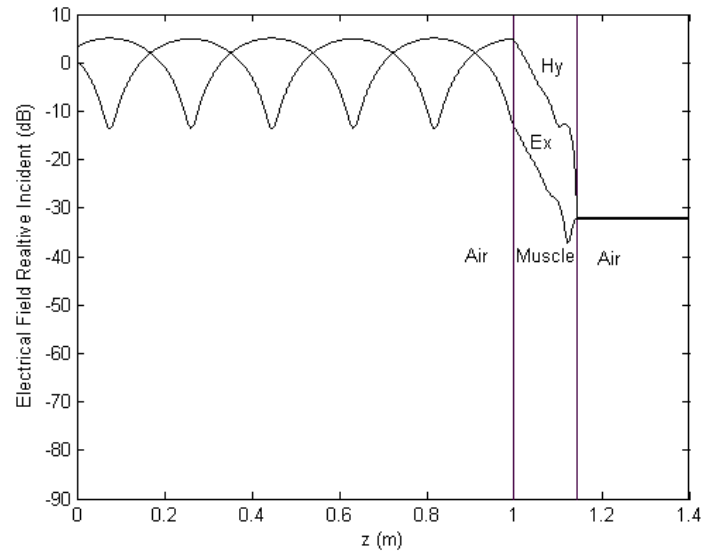The apparent discontinuity of the magnetic field is due to the current density in the skin, i.e.,

Figure 4.1: The RMS electric and the magnetic fields when a plane wave travelling in the positive z-direction hits upon a simple 1D phantom.
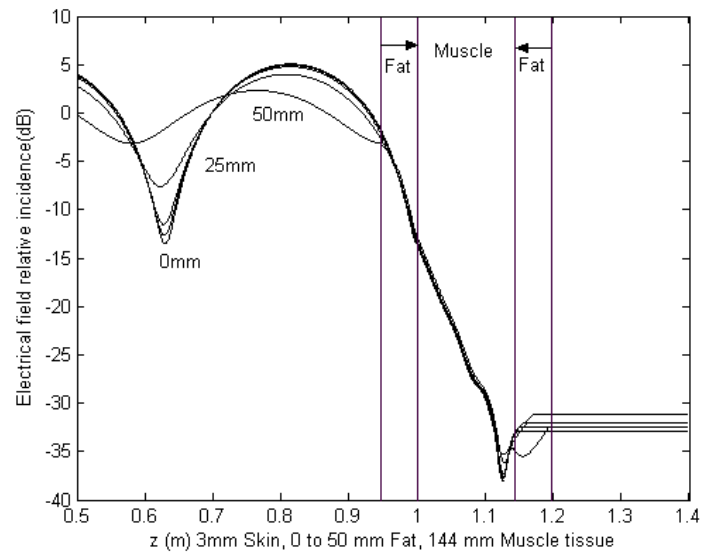

Figure 4.2: Electrical field strength dependence on fat layer thickness.
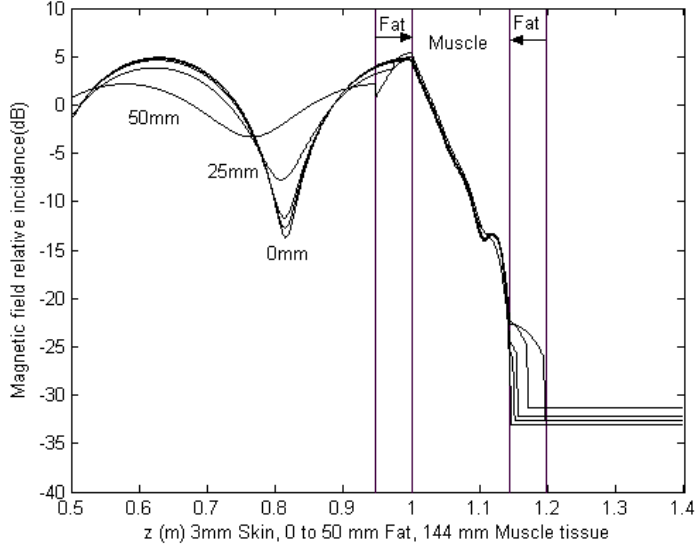
Figure 4.3: Magnetic field strength dependence on fat layer thickness.

$$\hat{n} \times (\vec{H}_{air} - \vec{H}_{fat}) = \vec{J}_{skin} \cdot d_{skin} \qquad (4.17)$$

where

$$\vec{J}_{skin} = \sigma_{skin} \cdot \vec{E}_{skin} \qquad (4.18)$$

is the current density in the skin and d_{skin} is the thickness of the skin. This is a fairly good approximation since $d_{skin} \ll \lambda$.

Another investigation was done where we added a lung to the model. The dimensions of the lung come from [32]. This model is even less realistic than the previous ones as the lung in the body is far from a slab-like formation. The simulations were done in order to investigate if the low-loss low-permittivity part that the lung represents, would significantly alter the properties at the depths where a medical implant would be placed. The results are shown in Figures 4.4 and 4.5. There are no large differences at the interface between the fat and the muscle layer between the two versions, with and without the lung, of the simulated body. The level of the E-field is here between -13.6 dB and -14.7 dB at the muscle interface.

The simulations were repeated for a frequency of 2.45 GHz, corresponding to the popular ISM (Industrial Scientific and Medical) license free band used for Bluetooth [35] and wireless local area networks, or WLAN [36]. Simulations for a structure with a homogenous muscle layer, a 3mm outer skin layer and a 5mm fat layer were carried out. The results are shown in Figures 4.6 and 4.7,
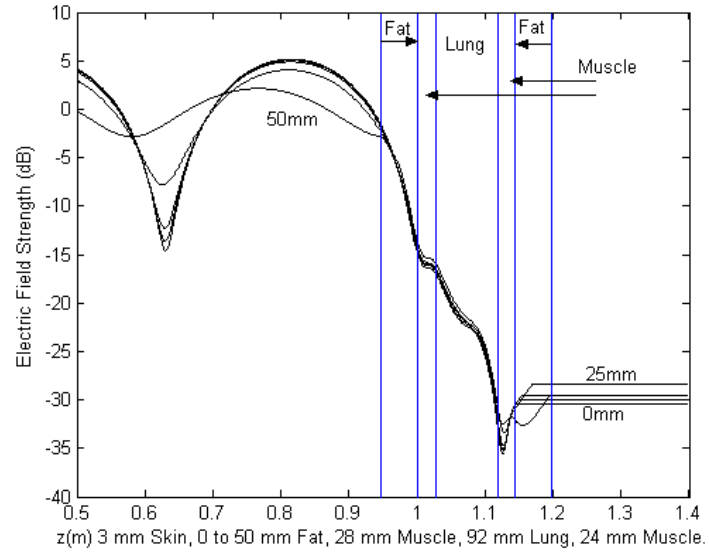
Figure 4.4: Electric field strength dependence on fat layer thickness.
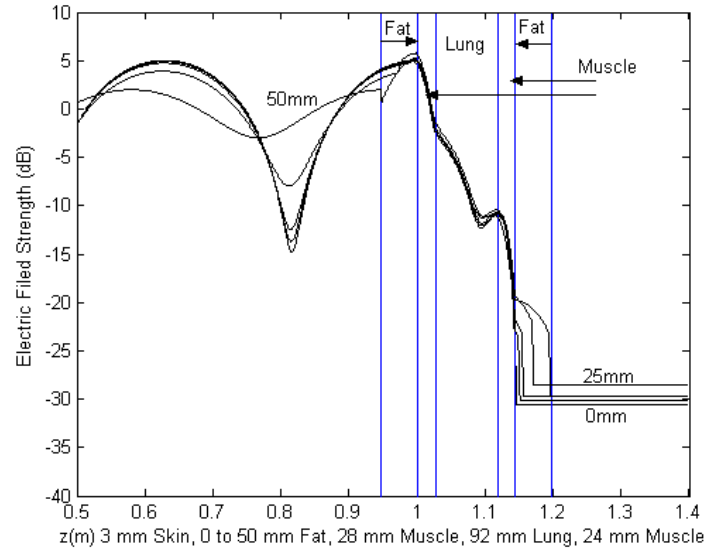

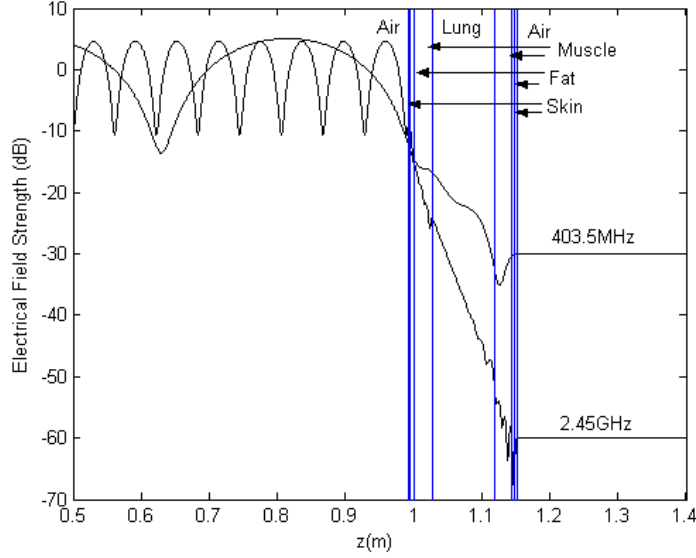Figure 4.5: Magnetic field strength dependence on fat layer thickness.

Figure 4.6: Electric field strength dependence on frequency.

together with the corresponding results for 403.5 MHz. The amplitude of the electric fields in Figure 4.7 are comparable for the two frequencies at the point where a pacemaker is implanted, i.e., at the 1.0 m mark. The higher frequency is attenuated more when propagating through the body, and thus the lower frequency is better for implants placed deeper inside the body.

4.4 Analytic investigation of a layered structure

King and Smith have made calculations on "Transponder Antennas In and Near a Three-Layered Body" in [37]. They have investigated a layered half-space of skin, fat and muscle tissue. The third layer, the muscle tissue, is extending to infinity in the z-direction. The incident field is typically a plane wave at normal incidence

$$\vec{E}_y^i = E_{y_0} e^{-jkz} \hat{y} \tag{4.19}$$

The calculations are done with a skin thickness of 5 mm and a fat thickness of 10 mm. Only the amplitude of the electric field was calculated. The amplitude of the electric field was obtained by calculating the transfer function $G(z, \omega) = E_y(z, \omega)/E_{y_0}$. In this case, the tissue parameters are quite different from those used in the one-dimensional simulations, as can be seen in Table 4.4.
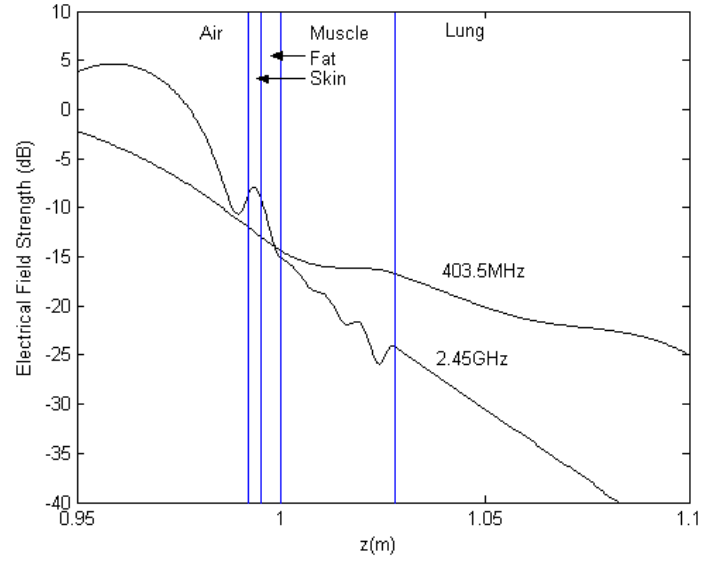
Figure 4.7: Closeup on the surface where the plane wave is reflected.

Tissue	ϵ_r	σ_e (Si/m)	$\tan \delta$	k
Skin	48	0.85	0.80	61.9-j21.8
Fat	6.0	0.059	0.44	20.9-j4.5
Muscle	53	1.14	0.97	66.6-j27.2

Table 4.4: Parameters from King et.al. 1980

Param	value
C_1'	0.254-j0.097
C_1''	0.043-j0.042
C_2'	0.466+j0.028
C_2''	-0.155-j0.161
C_3	0.196-j0.161
C_0	-0.702-j0.139

Table 4.5: Coefficients from King et.al 1980.

The amplitude of the electric field inside the different layers is calculated from the following equations:

$$E_{yo}(z,\omega) = E_y^i(0,\omega)e^{-jk_0z}; -\infty \leq z \leq 0 \tag{4.20}$$

$$E_{y1}(z,\omega = C_1'e^{-jk_1z} + C_1''e^{jk_1z}; 0 \leq z \leq a \tag{4.21}$$

$$E_{y2}(z,\omega) = C_2'e^{-jk_2z} + C_2''e^{jk_2z}; a \leq z \leq c \tag{4.22}$$

$$E_{y3}(z,\omega) = C_3e^{-jk_3(z-c)}; c \leq z \leq \infty \tag{4.23}$$

Here $z = 0$ is the position of the air to skin interface, $z = a$ is the position of the skin to fat interface and $z = c$ is the fat to muscle interface. It is quite straightforward to obtain the coefficients by utilizing the boundary conditions, i.e., that the electric and magnetic fields are continuous at all interfaces. The derivations are presented in Appendix C. The coefficients given in the article [37] are repeated in Table 4.5.

The equations were evaluated in Matlab and the result is plotted in Figure 4.8 together with the corresponding result from a one-dimensional FDTD simulation. The results show that the FDTD simulations and the analytical solution from King et.al. in [37] agree. The interesting case for medical implant applications is an antenna inside a human shaped lossy object. The search of an analytic solution to this problem was not considered an effective use of time. Instead FDTD simulations were used to investigate the more complicated cases. This will be reported in Chapters 5 and 6.

4.5   Two-dimensional simulations

A two-dimensional simulation can be done by studying an infinite cylinder. The cylinder is layered in the same fashion, and with the same thicknesses, as in Figure 4.4. By using expansions of the incident field, the internal fields, and the reflected field in cylindrical waves the results shown in Figures 4.9 and 4.10 were obtained. The analysis for the two-dimensional case is presented in Appendix C. When the incident E-field is parallel to the cylinder axis, the results correspond
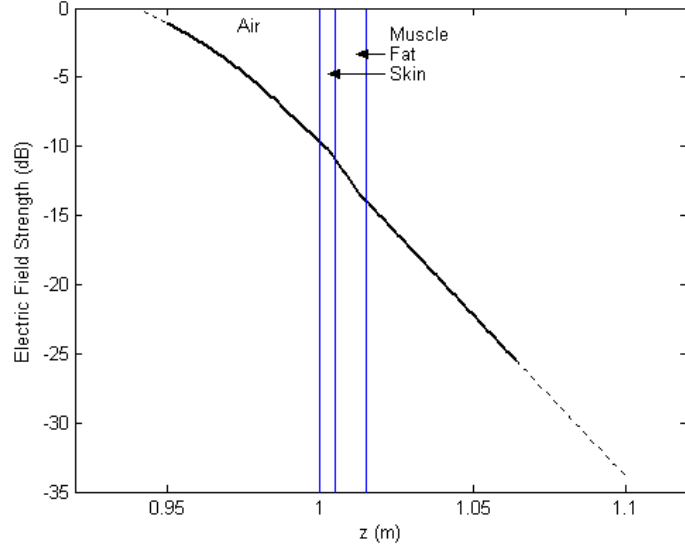
Figure 4.8: Comparison between calculations after King (solid curve) and 1D FDTD simulations (dotted curve).

well with the 1D simulations. The reduction of the H-field due to the current in the skin layer is apparent. A new effect is that the electromagnetic waves curve around the cylinder and give rise to an interference pattern on the backside of the cylinder. The second case where the incident E-field is perpendicular to the cylinder axis, gives a result that differs more from the 1D simulations. Here the incoming E-field is not aligned to the cylinder, which thus will not agree well with the infinite planar surface in the 1D simulations.

4.6   Conclusion

From the results in this chapter, we conclude that the amplitudes of the E- and H-fields inside a dielectric body depend both on the depth and on the exact composition of the body. A layered structure gives rise to variations in the E-field due to reflections. The same is true for the H-field. The exact field that an implanted antenna operates in will thus depend on the thickness of the fat layer, which varies between individuals and with time. The thickness of the muscle layer behind the implant will also influence the wave propagation. This shows that antennas for medical implants must either be insensitive to this kind of varying operating conditions, or be designed with an appropriate margin to operate within the specifications in all instances.
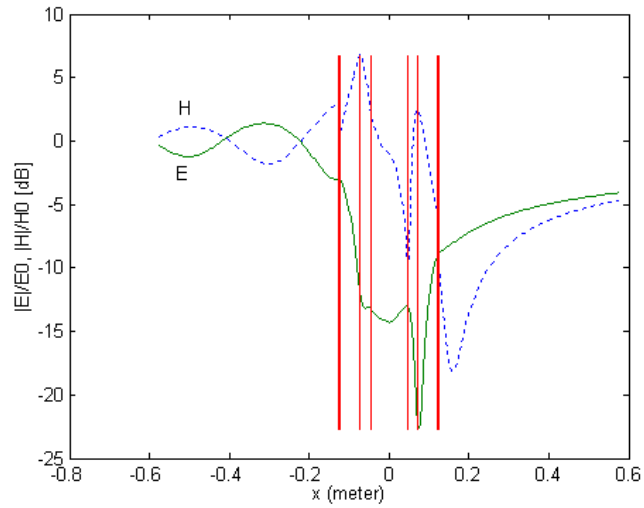
Figure 4.9: E- and H-field for a layered cylinder of skin-fat-muscle-lung-muscle-fat-skin. the incident E-field is parallel to the cylinder axis.
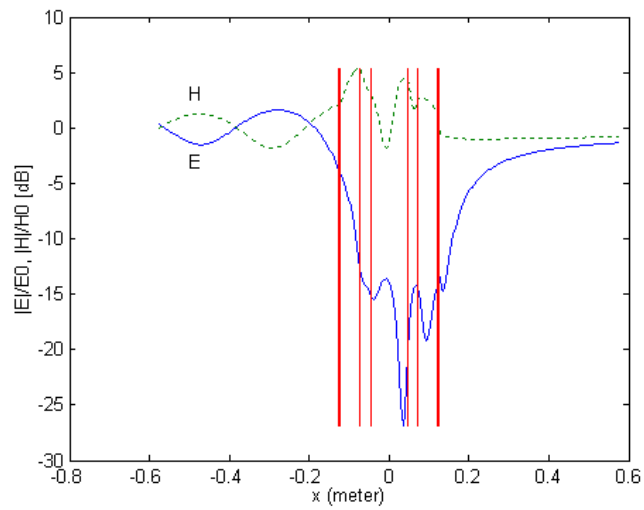

Figure 4.10: E- and H-field for a layered cylinder of skin-fat-muscle-lung-muscle-fat-skin. The incident H-field is parallel to the cylinder axis.

Chapter 5

Antenna Design

Antenna design is a mature science today, and an engineering discipline with a large number of design manuals available, e.g. [28][38][39]. All these books have one thing in common: they mainly describe antennas placed in a non-conducting surrounding with a relative permittivity of 1, or close to 1. In other words, they describe antennas placed in vacuum or air. The only structure that is typically found close to the antenna is a radome, which is made of low loss materials with low permittivity. When the antenna is placed inside a human body, we have a completely different situation. The antenna is surrounded by a lossy material with high permittivity. There are two instances in classical antenna applications where similar conditions occur: buried antennas and submarine antennas. Buried antennas are closely related to the beverage antenna, developed by H. Beverage, C. Rice and E. Kellogg in 1923[40]. The theory of buried antennas was developed in order to cover the applications of submarine communication at VLF, and geophysical prospecting. In addition, the need to communicate from bunkers built during the cold war added interest to the field in the period 1960-1970 [41]. At that time, the main interest was in low frequency applications, and the general simplification was a lossy half-space with the buried antenna, with the other half-space being air. King and Smith wrote the book "Antennas in Matter" in 1981 which sums up this field[31]. Onward, from 1980, not many articles have been published about "buried antennas", "underwater antennas" or submarine communication.

Submarine communication at low frequencies uses trailing wire antennas [42]. Other antenna systems for submarines are located in the tower, or sail, and are used when this part of the submarine is above the surface of the water. Towed buoys with antennas are also used. The design of an efficient underwater antenna, for a frequency band with high information transfer properties, is hard. This can be seen in that newly tested autonomous underwater vehicles, designed to locate and destroy sea mines, all incorporate a mast in order to keep the antennas, used to communicate with the mother ship, above the water [43].

High frequency antennas dedicated to medical implants are rare in the literature. One well-reported design is shown in [44] and a couple of patents

have been granted, [45][46][47]. Apart from these we have found very little in the literature. If we expand the search to "biomedical telemetry" there is much more published, but mostly for low frequencies, and utilizing inductive coupling. However, the design of antennas for biomedical telemetry is not well published either. The systems themselves are described, both in classic texts such as those by Mackay[48] and Caceres[49], and in published articles. The systems described in the books use mainly coil antennas, as they use low frequencies for transmission. Most of the commercially available implantable systems today from Advanced Telemetry Systems [50] use coil antennas, although some use wire antennas similar to the trailing wire antennas for submarines. The wire antennas are often used for aqueous animals. Subcutaneously implanted wire antennas are also used for birds. No information about the design of these wire antennas is given.

5.0.1 What is the antenna?

When we look at the antenna implanted in a lossy and finite body, the definition of the extent of the antenna needs to be discussed. The naïve view is that the antenna is what is attached to the implant, which is then inserted into the patient. This disregards the influence of the implants on the antenna characteristics. Furthermore, the analysis of the radio link will have to consider a wave propagating from the antenna through the body into the air and over to the base-station antenna. This propagation is hard to characterize, especially as it is hard to characterize the radiation pattern from the implant itself. The radiation characteristics are influenced by the tissues in the near-field of the antenna, and thus vary between different patients.

If we now look at the system from the outside, we can define the implant antenna characteristics as the sum of the implant antenna, the implant itself *and* the body. This is what we will see as a radiating structure when the radiating implant is in place. It is of this structure that we can measure the gain and the efficiency. The complication is that we then have to include the body shape and the actual placement of the implant in the analysis. However, this is no real change, since we always have to make sure that the antenna works when placed where it will actually be used. It also leads to the added complexity that the link budget will not have a fixed gain of the implant antenna. The gain, the directivity, and the efficiency will vary with the patient. These variations must be taken into account by adding them to the link budget calculations.

5.1 Antenna efficiency calculations in matter

The definition of the efficiency of an antenna inside a lossy matter is not obvious, as the far-field is attenuated to zero due to the losses. The standard definition of antenna gain is $G(\theta, \phi) = \eta D(\theta, \phi)$ where η is the efficiency factor [28]. $D(\theta, \phi)$ is the directivity of the antenna and is defined from the normalized power pattern P_n as

$$D\left(\theta,\phi\right) = \frac{P_n\left(\theta,\phi\right)}{P_n\left(\theta,\phi\right)_{\text{average}}} = \frac{\left|\vec{F}\left(\theta,\phi\right)\right|^2}{\left|\vec{F}\left(\theta,\phi\right)\right|^2_{\text{average}}} \tag{5.1}$$

where $\vec{F}\left(\theta,\phi\right)$ is the far-field amplitude.

The normalized power pattern P_n is defined from the Poynting vector, $S = \vec{S}\cdot\hat{r}$, as

$$P_n\left(\theta,\phi\right) = \frac{S\left(\theta,\phi\right)}{S\left(\theta,\phi\right)_{\text{max}}} = \frac{\left|\vec{F}\left(\theta,\phi\right)\right|^2}{\left|\vec{F}\left(\theta,\phi\right)\right|^2_{\text{max}}} \tag{5.2}$$

This definition also applies to antennas inside lossy media. What does not apply is the normal intuitive definition of the pattern as taken in the (extreme) far-field. This since the radiating power of an antenna inside a lossy medium is attenuated by the matter as it propagates outward. This has the consequence that the position of the origin is important, as it influences the shape of the pattern [51].

The far-field amplitude is defined as

$$\vec{F}\left(\theta,\phi\right) = \lim_{|k|r\to\infty}\vec{E}\left(r,\theta,\phi\right)kre^{jkr} \tag{5.3}$$

From Equation 4.8 it is seen that for a homogenous space, with a source current density $\vec{J}_s\left(\vec{r}\right)$ in a volume V_s, the far-field amplitude is given by [30]

$$\vec{F}\left(\theta,\phi\right) = -j\omega\mu k\left(\overline{I}-\widehat{rr}\right)\cdot\int_{V_s}e^{jk\hat{r}\cdot\vec{r}'}\vec{J}_s\left(\vec{r}'\right)dv' \tag{5.4}$$

The definition of the efficiency of an antenna inside a lossy medium has to be adopted from the one used in air. The usual way of defining antenna efficiency is

$$\eta_{lossless} = \frac{P_{radiated}}{P_{accepted}} \tag{5.5}$$

Here $P_{accepted}$ is the power that is accepted by the antenna, i.e., the input power to the antenna subtracted with the reflected power from the antenna. In the case of an antenna in matter we have to modify this definition, as the quantity $P_{radiated}$ will vary with the radius r. The radiated power has the r-dependence

$$P\left(r\right) = P_0 e^{-2\,\text{Im}[k]r} \tag{5.6}$$

where r is the radius at which we calculate the power.

We define the efficiency of an antenna in a lossy matter as

$$\eta_{lossy} = \frac{P_0}{P_{accepted}} \tag{5.7}$$

This definition is valid also for a lossless medium, and hence we can use the notation η for both lossy and lossless media. When the gain is given without any direction stated, the maximum gain is implied. The same applies to the directivity. The gain of antennas both in air and in matter is thus defined as

$$G = \eta D \tag{5.8}$$

In order to measure or calculate P_0 we use

$$P_0 = \mathrm{Re} \oint_S \vec{S}(r, \theta, \phi) \, e^{2\,\mathrm{Im}[k]r} \cdot \widehat{r} dS \tag{5.9}$$

The surface S is a sphere in the far-zone of the antenna with the center at the origin. $\vec{S}(r, \theta, \phi)$ is the complex Poynting vector

$$\vec{S}(r, \theta, \phi) = \frac{1}{2} \vec{E}(r, \theta, \phi) \times \vec{H}^*(r, \theta, \phi) \tag{5.10}$$

The surface S is not constrained to be a sphere. It can be any closed surface that encloses the antenna and is in the far-zone. To illustrate this we notice that the far-zone is characterized by that there is no $\widehat{r}$-component of the amplitude vectors $\vec{E}$ and $\vec{H}$ and

$$\vec{E}(r, \theta, \phi) = \vec{F}(\theta, \phi) \frac{e^{-jkr}}{kr} \tag{5.11}$$

$$\vec{H}(r, \theta, \phi) = Z_m^{-1} \widehat{r} \times \vec{E}(r, \theta, \phi) \tag{5.12}$$

Here $Z_m = \sqrt{\mu/\varepsilon_c}$ is the wave impedance. The corresponding Poynting vector reads

$$\vec{S}(r, \theta, \phi) = \frac{1}{2} Z_m^{*-1} \left| \vec{F}(\theta, \phi) \right|^2 \frac{e^{-2\,\mathrm{Im}[k]r}}{|k|^2 \, r^2} \widehat{r} \tag{5.13}$$

Let S_a be an arbitrary closed surface that encloses the antenna and that is in the far-zone of the same antenna. We denote the outward pointing normal unit vector by $\widehat{n}$. Let S be a spherical surface that encloses the surface S_a. We denote the volume between S and S_a with V. From Gauss' theorem we get

$$\oint_{S_a} \vec{S}(r, \theta, \phi) \, e^{2\,\mathrm{Im}[k]r} \cdot \widehat{n} dS = -\int_V \bigtriangledown \cdot \left(\vec{S}(r, \theta, \phi) \, e^{2\,\mathrm{Im}[k]r} \right) dV$$
$$+ \oint_S \vec{S}(r, \theta, \phi) \, e^{2\,\mathrm{Im}[k]r} \cdot \widehat{r} dS \tag{5.14}$$

The volume integral is zero since

$$\bigtriangledown \cdot \left(\vec{S}(r, \theta, \phi) \, e^{2\,\mathrm{Im}[k]r} \right) = \frac{1}{2} Z_m^{*-1} \left| \vec{F}(\theta, \phi) \right|^2 \frac{1}{r^2} \frac{\partial}{\partial r} r^2 \left(\frac{1}{|k|^2 \, r^2} \right) = 0 \tag{5.15}$$

Thus

$$\text{Re} \oint_{S_a} \vec{S}(r, \theta, \phi) e^{2\,\text{Im}[k]r} \cdot \hat{n} dS = P_0 \qquad (5.16)$$

In this way, it is possible to calculate the efficiency of the antenna by integrating the Poynting vector numerically over an arbitrary closed surface in the far-zone.

The problem of measuring the efficiency of the antenna in an homogenous medium is not very important for the MICS application, since most of the time we are interested in systems which communicate from the inside of a lossy medium to a device outside in air. Thus, the relevant measurements of the system include the lossy body and efficiency measurements can be done utilizing a liquid phantom, as described elsewhere in this thesis. However, in the development of different antennas, it is interesting to be able to compare them by efficiency, especially since there is a large risk of the accepted power being absorbed by the surrounding lossy liquid in the near-field, and not giving rise to a useful far-field.

To summarize, we now have three complementary definitions of radiation efficiency for an antenna. All three follow the general definition of

$$Radiation\ Efficiency = \frac{Power\ Out}{Power\ Accepted} \qquad (5.17)$$

The three different cases are with the antenna in air, the antenna in an infinite body of lossy matter and the antenna in a finite body of lossy matter that is placed in air. The last one follows from the first, if the finite body with the internal antenna is treated as one large antenna.

5.2 Antennas in matter

When we place an antenna in matter there is a number of things that change in comparison with the antenna in air. One difference is that the wavelength changes, which is due to the change in ε_e and σ_e, cf. Equations 4.13 and 4.14. The wavelength in the material is shorter since the wave propagation speed is lowered. The reduction becomes

$$\lambda_m = \frac{\lambda_0}{\text{Re}\left[\sqrt{\varepsilon_{er} - j\frac{\sigma_e}{\omega\varepsilon_0}}\right]} \qquad (5.18)$$

One other difference is that losses in the material will affect both the near-field and the the wave propagation. Our main interest is small antennas for medical implants. The electromagnetic field from a small antenna in a lossy material can be expressed in terms of the currents in the antenna. Equation 4.8 can be used to discuss some fundamental aspects of small antennas in matter. First we assume that the volume V is a sphere with a radius a. Outside the sphere the electric field can always be expressed as a multipole expansion. The expansion reads

$$\vec{E}\left(\vec{r}\right) = \sum_{l=1}^{\infty} \sum_{m=0}^{l} \sum_{\tau=1}^{2} a_{\tau ml(even)} \vec{u}_{\tau ml(even)}\left(\vec{r}\right) + a_{\tau ml(odd)} \vec{u}_{\tau ml(odd)}\left(\vec{r}\right) \quad (5.19)$$

which follows from Equation 4.8 and an expansion of the Green function in spherical waves. The details can be found in [52] and [53]. Every term in the sum constitutes an outward propagating spherical wave, here called a partial wave. The explicit expressions for the partial waves $\vec{u}_{\tau ml}\left(\vec{r}\right)$ are given in the Appendix B. The partial waves constitute a complete orthogonal set of vector waves on a spherical surface. That means that we can obtain any radiation pattern by a suitable set of partial wave amplitudes $a_{\tau ml}$. This can be achieved by designing the currents in the volume V that give this set. Observe that there is no limit to the size of the volume V, i.e., the antenna can be arbitrarily small. This goes against common antenna design thumb rules, where antennas with higher directivity always have a larger size. The answer to this contradiction is that the high directivity small antenna has very large losses, i.e., the small, compact high directivity antenna has a very low gain. The $l-$value is linked to the angular variation of the field, as can be seen in the expression in the Appendix B. In [52] and [53] it is shown that the optimal directivity of an antenna with a maximum index $l_{\max}$, i.e., for which

$$\vec{E}_r\left(\vec{r}\right) = \sum_{l=1}^{l_{\max}} \sum_{m=0}^{l} \sum_{\tau=1}^{2} a_{\tau ml(even)} \vec{u}_{\tau ml(even)}\left(\vec{r}\right) + a_{\tau ml(odd)} \vec{u}_{\tau ml(odd)}\left(\vec{r}\right) \quad (5.20)$$

is bounded by

$$D \leq l_{\max}\left(l_{\max} + 2\right) \quad (5.21)$$

Equation 5.21 shows that in order to get a large directivity D we need to have a large l. From Equation B.10 we get that in the near-zone, $kr \ll 1$, the partial wave of index l is proportional to

$$\vec{u}_{\tau ml}\left(\vec{r}\right) \sim \begin{cases} (kr)^{-l-1} & \text{when } \tau = 1 \\ (kr)^{-l-2} & \text{when } \tau = 2 \end{cases} \quad (5.22)$$

The corresponding power flow is proportional to $(kr)^{-2l-3}$. This shows that the near-field grows rapidly with l. That implies that the electric and magnetic energies that are stored in the near-zone grow rapidly with l. The stored energy is linked to a reactive power flow and does not contribute to the radiation from the antenna. As we needed a large $l-$value to get a large directivity, we get large reactive near-fields around the antenna, which implies large non-radiating currents in the antenna. Since the metal in the antenna has a finite conductivity, the non-radiating currents give rise to an ohmic loss in form of heat. This, in turn, leads to the low gain of the high directivity small antenna.

This result still holds when we add losses to the matter in which the antenna is placed. The large near-fields will then be an even larger problem. As the surrounding matter is lossy, the wavenumber k is complex and the reactive fields are not purely reactive and will lose energy to the matter. This power loss is non-radiating since it consists of ohmic losses in the near-field of the antenna, i.e., heat. The antenna in a lossy matter thus loses power in three ways: ohmic losses in the antenna, ohmic losses from the near-field in the matter and radiated power. The radiated power will be attenuated by the lossy matter and converted to heat as it propagates. The accepted power in Equation 5.17 then reads

$$P_{accepted} = P_{ohm} + P_{nearfield} + P_0 e^{-2\,\mathrm{Im}(ka)} \qquad (5.23)$$

where a is the radius of a lossless sphere, in which the antenna is confined. The radiated power loss is independent of l, while the other two increase with l. Thus in the case of antennas in a lossy matter, one should keep the $l-$value low, which gives a low-directivity antenna. The dipole variants all have $l = 1$, and are to prefer. The power loss in the near-zone can be reduced by using an insulator around the antenna. One can give a rule of thumb for antennas in a lossy matter that

The most power efficient small antenna in a lossy matter is the dipole with as thick an insulation as possible.

This can be illustrated by the graphs in Figure 5.1, after [52]. They are calculated by numerical evaluation of the multipole expansions in muscle tissue at 400 MHz. Figure 5.1 illustrates that dipole antennas are more efficient than higher order antennas, and that magnetic antennas are more efficient than electric ones. It also illustrates that the thicker the insulation surrounding the antenna is, the more efficient is the antenna. A magnetic dipole antenna should have at least 2 mm of insulation, an electric 4-6 mm.

We now restrict the discussion to dipoles. The dipole antennas only create partial waves with $l_{\mathrm{max}} = 1$. The maximum directivity of such an antenna is 3, according to Equation 5.21. There are three main choices of dipoles: the electric dipole, the magnetic dipole and the combined dipole. The magnetic dipole is the most power efficient antenna, if we do not take the ohmic losses in the antenna into account. It is typically a coil which is resonated at the correct frequency by an external capacitor to get a resistive antenna impedance. The directivity of the magnetic antenna is 1.5, or 1.8 dB [28]. The electric dipole is less power efficient since the near-field is stronger. This is in practice compensated by the lower ohmic losses in the antenna, as the currents there are lower. The electric dipole can be made resonant by connecting an inductor in series with the antenna. The directivity of the electric dipole is the same as for the magnetic dipole, 1.5. The third type of dipole is the most common; it is the combination of an electric and a magnetic dipole. This can be made resonant in itself by a proper combination of the two dipoles. The common resonant half-wave dipole is such an antenna. Placed in free space it is efficient since both the magnetic and the electric parts radiate, which keeps the non-radiating currents low. A directivity of 3 can only be achieved when the electric and magnetic dipole moments are perpendicular
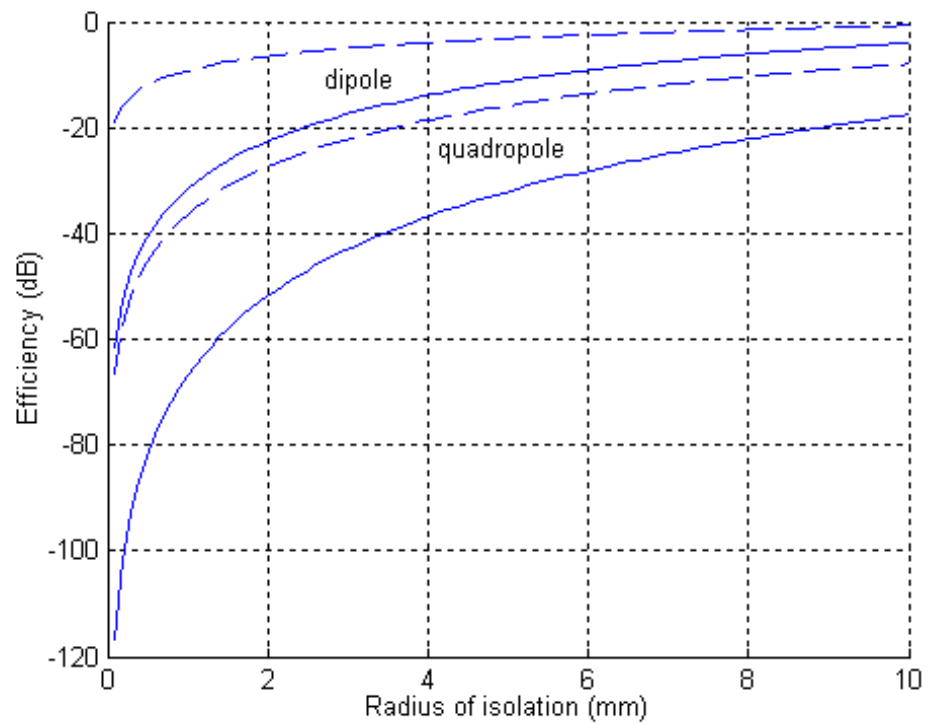
Figure 5.1: The efficiency of an antenna inside a lossless sphere of radius a inside muscle tissue. Solid lines are for electric vs. dashed for magnetic antennas. Dipoles have $l = 1$ and quadropoles have $l = 2$.
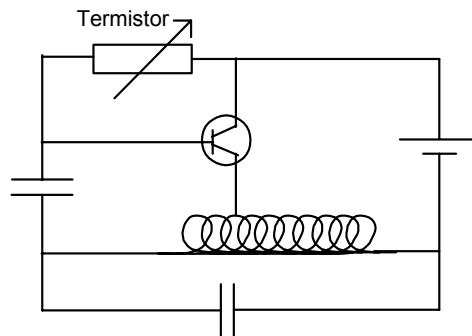
Figure 5.2: Schematic of simple circuit which transmitts a frequency which is dependent on the temperature.

to each other. From this discussion, we can draw the conclusion that in a lossy matter we should use one of the following two types:

1. A resonant dipole antenna.
2. A magnetic dipole antenna.

In the case of the medical implant antenna the conditions change. The main difference is that we do not have an infinite lossy body in which the antenna is placed, but instead a finite body placed in a surrounding of air (and clothes, furniture, houses etc.). Furthermore, we will operate the antenna close to a conducting pacemaker case. To analyze this analytically would be too complex, which makes it necessary to use numerical simulations. We have investigated both types of the above recommended antennas by simulations and measurements. In addition, we have looked at the wire antenna, which is a classical antenna for implants.

5.3 Implantable antennas

There is a number of different antenna designs that may be used for medical implants. As mentioned above, coil antennas are used for biomedical telemetry at low frequencies [54]. They are a good choice since they are compact when used in short distance links combined with a low carrier frequency. One classic design is to use the tuning coil of the oscillator as the antenna, and thus get the antenna for free. An example, taken from [54] is shown in Figure 5.2.

We have investigated a number of different antenna designs, which mainly are resonant electric antennas, in contrast to the coil antenna, which is a magnetic antenna. The main objective has not been to find the best antenna for use in a medical implant, but to get a valid figure for a reasonable antenna performance to be expected from a medical implant. We have also aimed at getting an understanding of how the human body influences the antenna design. The common use of polar plots in order to show the characteristics of an antenna

is not useful when the antenna is in a lossy matter [51]. The shape of the gain
plot depends on where on the antenna the origin of the plot is taken. In the
MICS application the far field gain is influenced by the shape of the body into
which the antenna is implanted, which will be shown in the next chapter.

We have investigated the following types of antennas:

- Dipole

- Wire

- Circumferential quarter wave

- Circumferential PIFA

- Patch

- Magnetic coil antenna

5.3.1   Method

In order to investigate the antennas both measurements and simulations were
used. The simulations were done with the FDTD method, described in Appen-
dix D. We used the program SEMCAD, by Shmid & Partner AG [55]. This
program implements an FDTD-code that uses non-uniform grids in order to
reduce the memory requirements. SEMCAD has been shown to give results
in good agreement with measurements [56]. The simulations of the antennas
were done with both continuous wave excitation and transient excitation. The
results presented are from the transient simulations. The simulation volume was
bounded by absorbing boundary conditions, ABC. We used 6 perfectly matched
layers as ABC.

The measurements were made with a physical implementation of our pace-
maker model, shown in Figure 5.3. The antenna was connected to an SMA-
connector inside the case, which was connected with a cable to a network an-
alyzer. The measurements were made in a phantom as specified in the MICS
standard [14], and filled with muscle tissue simulating liquid according to [24].

5.3.2   Wire antenna

One of the antennas used for implants is the wire antenna [54][50]. The basic
function is the same as the classical long-wire antenna [57], with some differ-
ences. The long wire antenna is sometimes placed on pylons above the ground
and uses the earth as a reflector, or as a part of a lossy waveguide structure.
In the case of the Beverage antenna, Figure 5.4, there is a load connected be-
tween the wire and the ground at the end of the antenna in order to minimize
the reflections. This connection is not common in the implantable case in the
references cited above.

Since the medium surrounding a wire antenna in matter is lossy, the travel-
ling wave is attenuated as it travels along the wire. When the wave is reflected

Figure 5.3: The physical implementation of our pacemaker model, here with the circumference antenna.
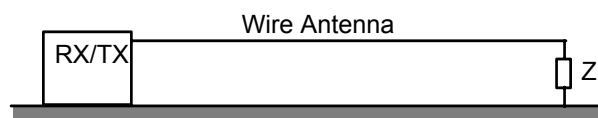

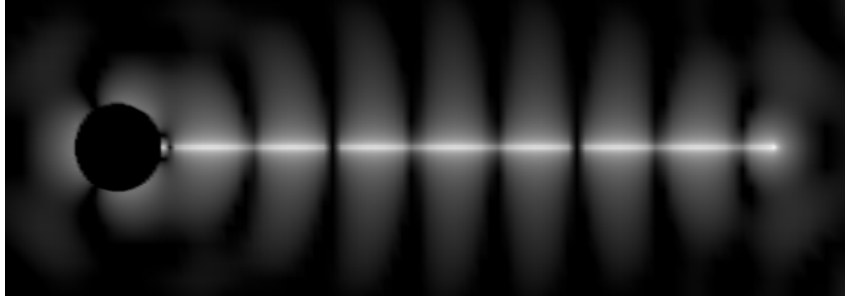Figure 5.4: Side view of a Beverage antenna.

Figure 5.5: The instantaneous electric field around a wire antenna in lossless muscle tissue, $\varepsilon_r = 62.5$. The simulated antenna is 360 mm long and it is fed with a 403.5 MHz signal.

at the end of the wire antenna it will travel back towards the feed point. Thus the impedance at the feed point depends on the length of the antenna, and of the reflection at the furthest end.

The un-insulated bare wire antenna in a medium with $\varepsilon_r \neq 1$ and $\sigma_r \neq 0$ is the first structure we study. The phase velocity of the electromagnetic wave in the wire is the same as the phase velocity in the medium outside: $v_p = v_c$, where v_p is the phase velocity in the wire antenna and v_c is the phase velocity in the matter surrounding the antenna. This makes the antenna a so called slow wave structure [28].

The phase velocity in the medium is

$$v_c = \frac{c_0}{\sqrt{\varepsilon_{er}}} \tag{5.24}$$

where ε_{er} is defined in Equation 4.15.

Figure 5.5 shows the instantaneous magnitude of the electric field around a wire in a loss-less medium. The wave fronts are circular and meet the wire at 90 degrees. The wave is reflected at the end of the wire antenna and forms a standing wave pattern that is visible in Figure 5.6. The simulated antenna is 360 mm long and it is fed with a 403.5 MHz signal.

In Figure 5.7 the same thing is illustrated, but this time for a wire in a medium with a conductivity $\sigma_e = 0.9$ S/m. Here the wave fronts still meet the wire at 90 degrees, which indicates that it is a slow wave structure. The amplitude of the field is attenuated along the wire and the standing wave pattern in the wire is much less pronounced than in the case of the loss-less medium. The impedance of this antenna is quite independent of the length of the wire.

If we surround the wire antenna with an insulation with a much lower permittivity than the surrounding matter we alter the phase velocity in the wire. The loss per unit length is lower as the lossy matter is now removed from the region of the strongest near-field. Thus, the reflection has a larger impact on the impedance. Now the antenna compromises a fast wave structure with
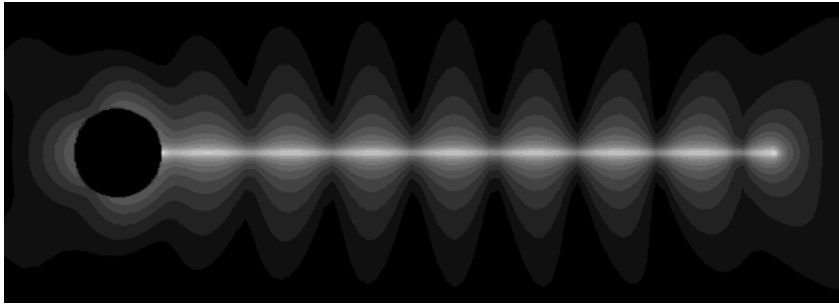
Figure 5.6: The RMS value of the electric field around a wire antenna in a lossless muscle tissue, $\varepsilon_r = 62.5$. The simulated antenna is 360 mm long and it is fed with a 403.5 MHz signal.
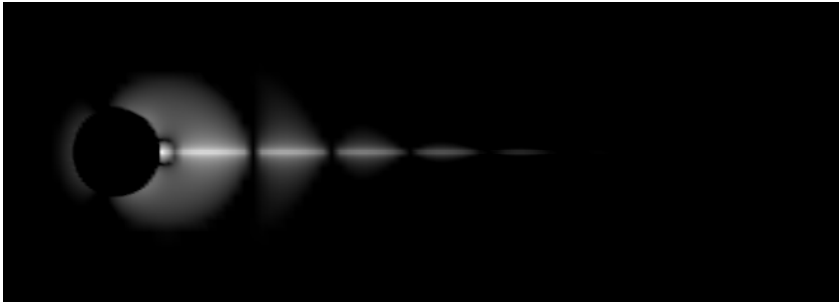

Figure 5.7: The instantaneous value of the electric field around a wire antenna in muscle tissue, with $\varepsilon_r = 62.5$, $\sigma = 0.9$. The simulated antenna is 360mm long and it is fed with a 403.5MHz signal.
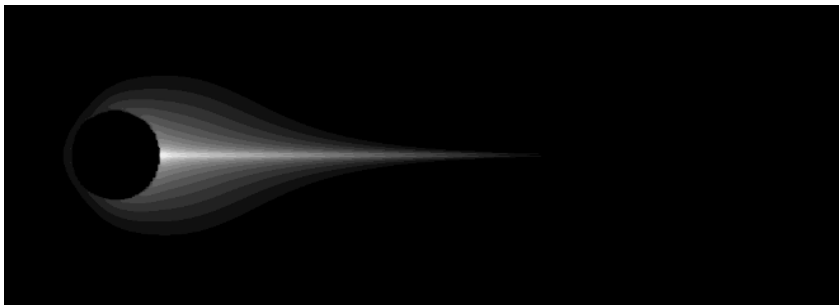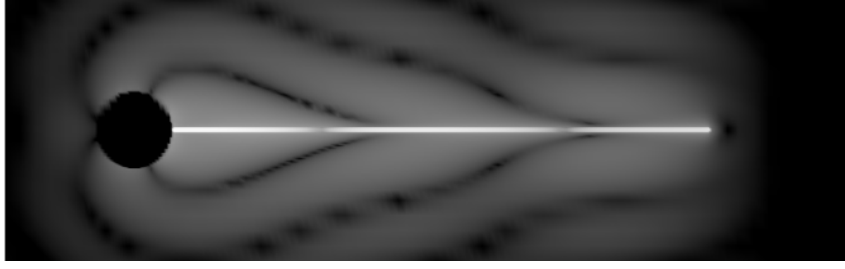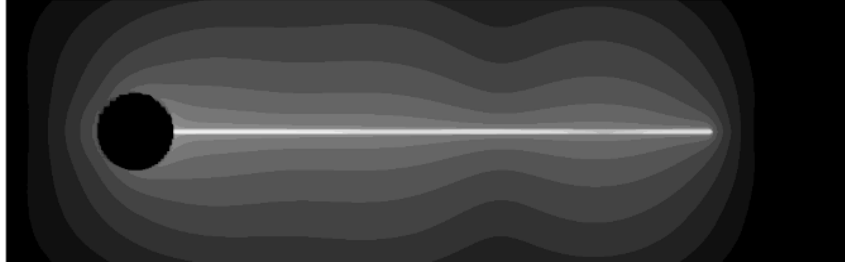

Figure 5.8: The RMS value of the electric field around a wire antenna in muscle tissue, with $\varepsilon_r = 62.5$, $\sigma = 0.9$. The simulated antenna is 360mm long and it is fed with a 403.5MHz signal.

Figure 5.9: The instantaneous electric field around an isolated wire antenna in muscle tissue, with $\varepsilon_r = 62.5$, $\sigma = 0.9$. The simulated antenna is 360mm long and it is fed with a 403.5MHz signal.

Figure 5.10: The RMS value of the electric field around an isolated wire antenna in muscle tissue, with $\varepsilon_r = 62.5$, $\sigma = 0.9$. The simulated antenna is 360mm long and it is fed with a 403.5MHz signal.

$v_p > v_c$. This is clearly seen in Figure 5.9 where the fields around an isolated wire in a lossy matter is illustrated. Here the wave fronts are at an angle of less than 90 degrees from the wire as the phase front moves faster in the wire than in the matter. The fast wave structure is common in leaky wave designs of antennas[28]. Due to the reduced loss, the reflected wave has a non-negligable amplitude when it reaches the feed point, and along the antenna we have a standing wave pattern, as is visible in Figure 5.10.

In a lossy matter the insulated wire antenna can be treated as a coaxial waveguide [31]. The lossy matter acts as the outer conductor. This waveguide has a propagation constant γ which is influenced both by the dielectric properties of the insulation, and by the properties of the surrounding matter. In [58] an approximate solution to the input impedance of the insulated wire antenna is presented. The impedance of the wire antenna is

$$Z_{wire} = Z_0' \coth \gamma l \tag{5.25}$$

where l is the length of the wire, and γ is the complex propagation constant approximated by

	Re[Z]	Im[Z]
Un-insulated Wire Antenna	30	3
Insulated Wire Antenna	50	-8

Table 5.1: Measured impedances of the wire antennas.

$$\gamma \approx \sqrt{-\omega^2 \mu_2 \varepsilon_2} \left(1 - \frac{j\pi/4 + \ln\left(0.89\sqrt{2}\frac{a_{out}}{\delta}\right)}{\ln\frac{a_{out}}{a_{in}}}\right)^{1/2} \tag{5.26}$$

Here μ_2 and ε_2 are the electromagnetic properties of the insulation, a_{out} and a_{in} are the outer and inner radii of the insulator and δ is the skin depth in the surrounding material. The characteristic impedance Z_0' is in [58] approximated by

$$Z_0' = \left(\frac{1}{2\pi} \ln \frac{a_{out}}{a_{in}}\right) \frac{\gamma}{j\omega\varepsilon_2} \tag{5.27}$$

and the skin depth is, as shown in Chapter 2

$$\delta = \frac{1}{\text{Re}\left[\gamma_s\right]} \tag{5.28}$$

where γ_s is the complex propagation constant of the surrounding material. The approximation in Equation 5.26 is valid if the propagation constant for the lossy outer medium is much greater than the line propagation constant γ. The approximation is said to be valid if $a_{out}/\delta < 0.1$.

For a wire antenna inserted into the muscle simulating liquid, with the wire dimensions of $a_{out} = 1.5$ mm, $a_{in} = 1$ mm, $l = 0.36$ m, and with $\varepsilon_2 = 2$ at $f = 403.5$ MHz, Equation 5.25 gives an antenna impedance of

$$Z_{wire} = 54 - j12 \ \Omega \tag{5.29}$$

The approximation is valid since

$$a_{out}/\delta = 0.03 < 0.1 \tag{5.30}$$

Measurements

A wire antenna of length 360mm was mounted on the pacemaker mock-up described earlier. The impedance of the antenna was measured with the antenna placed in the MICS phantom filled with the muscle liquid. The results are shown in Table 5.1. The impedance for the insulated wire agrees well with the calculated value in Equation 5.29. The Smith charts of the measurements are presented in Figure 5.12 and 5.11.
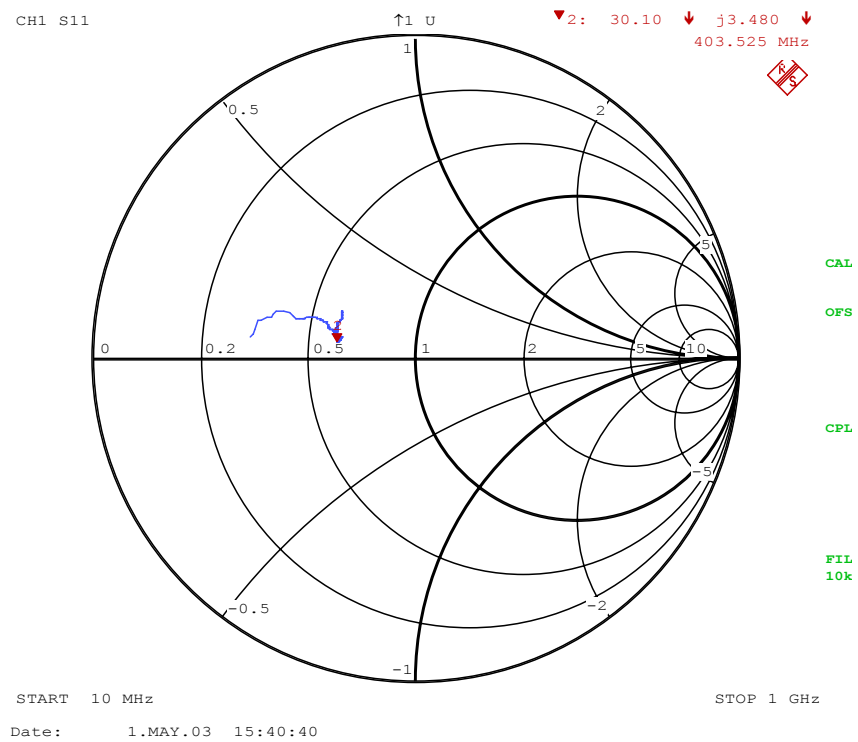
Figure 5.11: Smith chart from the measurement of the unisolated wire antenna in the simulated muscle tissue. The chart shows that the impedance is close to 50 Ω at 403.5 MHz. The frequency is swept between 10 MHz and 1 GHz.
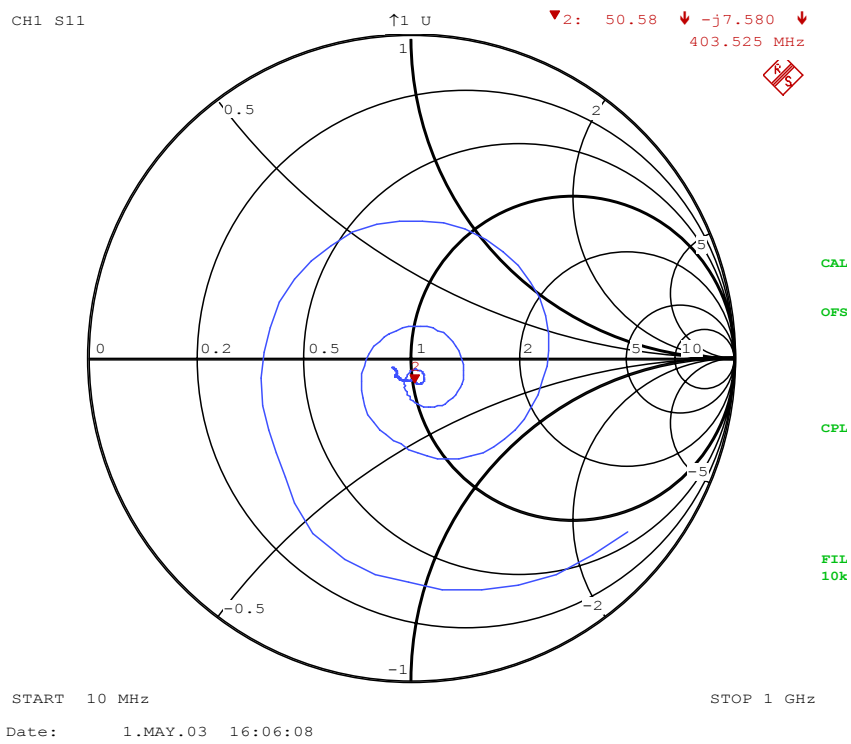
Figure 5.12: Smith chart of the measurement for the isolated wire antenna in the simulated muscle tissue. The chart shows that the impedance is very close to 50 Ω at 403.5 MHz. The frequency is swept between 10 MHz and 1 GHz.

Comments

In the case of communication with an implanted pacemaker the lead wire to the heart is a potential antenna. The insulated antenna in matter may be matched with a load resistor connected to the conducting medium in order to reduce or eliminate the reflection [31]. This makes the wire antenna in matter similar to the Beverage antenna described earlier. If the outermost conductor in the lead wire from the pacemaker to the heart would be used as an antenna, the electric connection between the lead wire and the heart muscle tissue at the end constitutes a terminating impedance for the antenna. The value of this terminating impedance at 400 MHz is unknown, and will probably change over time as the contact point is encapsulated by the body in the chronic implantation phase. If the lead wire were used as the antenna it would be beneficial to be able to use any lead wire, as these are typically chosen separately from the pacemaker. Since the reflections from the end of the antenna are reduced by the resistive connection to the heart tissue, the influence of the antenna's length on the impedance is reduced. The high frequency electrical properties differ between manufacturers, with different mechanical design of the spiralled flexible wire inside the pacemaker lead, and variations of the insulation thickness. The design of the electric connection between the wire and the heart tissue does also vary considerably [4]. Thus, there will be a variation of the antenna characteristics of the lead wire between manufacturers and over time. Another drawback of using the lead as the antenna is that one of the failures experienced in pacemakers is lead wire breakage. If the same wire is used as the antenna in the communication link, the cause of the failure will be hard to determine by simple means. From an engineering viewpoint it is better to separate the diagnostic tools from a known failure mode.

5.3.3   Circumference antenna

The circumference antenna is a compact antenna that is mounted around the edge of the pacemaker case. The antenna is similar to the one described in patent [46]. We have investigated this antenna mounted around the model pacemaker consisting of a 50 mm cylinder. We have also qualitatively verified the function of the antenna when mounted around a pacemaker case from St. Jude Medical. The circumference antenna is an attractive antenna in that it conforms to the shape of the medical implant onto which it is placed. Thus, it does not influence the mechanical properties of the implant to a large degree.

The analysis of the circumference antenna follows from the monopole quarter wave antenna in air. From [59] we get the relation between an antenna in air and the same antenna in a material with complex μ_c and ε_c as

$$\frac{1}{Z_m} Z\left(\omega, \varepsilon_c, \mu_c\right) = \frac{1}{Z_0} Z\left(n\omega, \varepsilon_0, \mu_0\right) \tag{5.31}$$

where

$$n = \left(\frac{\mu_c \varepsilon_c}{\mu_0 \varepsilon_0}\right)^{1/2} \tag{5.32}$$

$$Z_0 = \left(\frac{\mu_0}{\varepsilon_0}\right)^{1/2} \tag{5.33}$$

$$Z_m = \left(\frac{\mu_c}{\varepsilon_c}\right)^{1/2} \tag{5.34}$$

In the lossless case we only change the real part of the permittivity ε_c from ε_0 to $\varepsilon_e = n^2 \varepsilon_0$, where now $n = \sqrt{\varepsilon_e/\varepsilon_0} = \sqrt{\varepsilon_{er}}$ and Equation 5.31 then simplifies to

$$Z(\omega, \varepsilon_e) = \frac{1}{\sqrt{\varepsilon_{er}}} Z\left(\sqrt{\varepsilon_{er}}\omega, \varepsilon_0\right) \tag{5.35}$$

For a mid band frequency of 403.5MHz, the wavelength in air is $\lambda_0 = 0.74$ m. A quarter wave antenna will then have a theoretical length of 0.185 m. Equation 5.35 gives that this corresponds to a resonance frequency of 51 MHz if the same antenna is inserted into a lossless liquid, with $\varepsilon_e = 62.5$. The antenna has to be shortened by a factor of $\left(\sqrt{\varepsilon_{er}}\right)^{-1}$ in order to keep the resonance frequency fixed. In the lossy case the resonance angular frequency becomes complex, according to Equation 5.31, corresponding to a damped resonance. However, the shortening of the antenna is still a fairly good approximation. This would give an antenna length of 23 mm with the antenna in the lossy muscle liquid.

The impedance of a quarter wave monopole antenna is dependent on the shape and size of the ground plane, but is typically around 40 Ω at resonance[40]. The real part of the impedance for the bare quarter wave antenna is 5 Ω at resonance, according to Equation 5.35. The antenna thus has a low impedance. The practical antenna described below is longer since it is surrounded by an insulator, which decreases the effective ε_c that the antenna sees. The impedance should be higher, but the added effects of the capacitive coupling between the antenna and the ground plane counteracts this effect. This design of an antenna is also called a bent monopole or inverted L-antenna (ILA) [34].

Simulations and measurements have been made on the same model of an implant as for the wire antenna: a short brass cylinder with a diameter of 50 mm and a length of 10 mm. The circumference antenna was placed in a plastic insulator outlined in Figure 5.13. The insulator had a thickness of 10 mm and the antenna was placed in the center of it. The length of the antenna wire was 94 mm. The antenna was simulated with a feed between the end of the wire and the case. It was simulated as inserted in the muscle tissue liquid, which was terminated with an absorbing boundary condition of perfectly matched layers.

From Figure 5.15 we get that the bandwidth with the Standing Wave Ratio satisfying SWR<2, is 42 MHz. This is larger than the MICS allocation, which is only 3 MHz. The antenna was manufactured and measured immersed in the muscle tissue simulating liquid. The results are shown in Table 5.2.
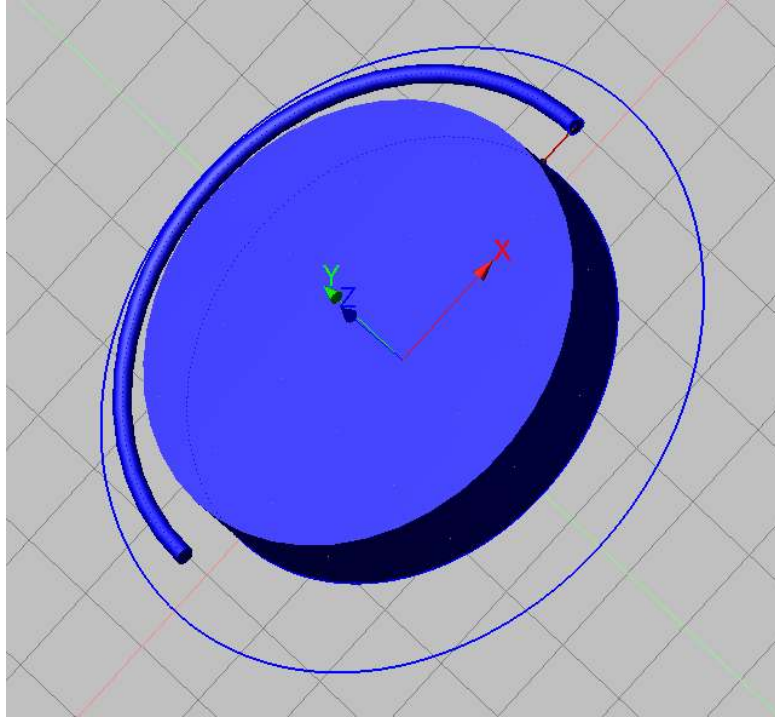
Figure 5.13: The CAD model of the circumference wire antenna. The thin circle is the radial extent of the isolation

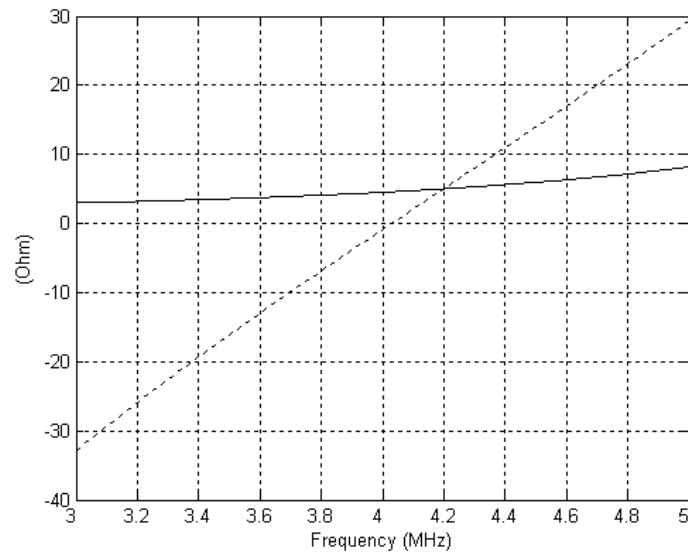|	$\mathbf{Re}[\mathbf{Z}_0]$	$\mathbf{f}_0$
Simulation	5 Ω	403.5 MHz
Measurement	7 Ω	403.5 MHz

Table 5.2: Impedance of the circumference wire antenna.

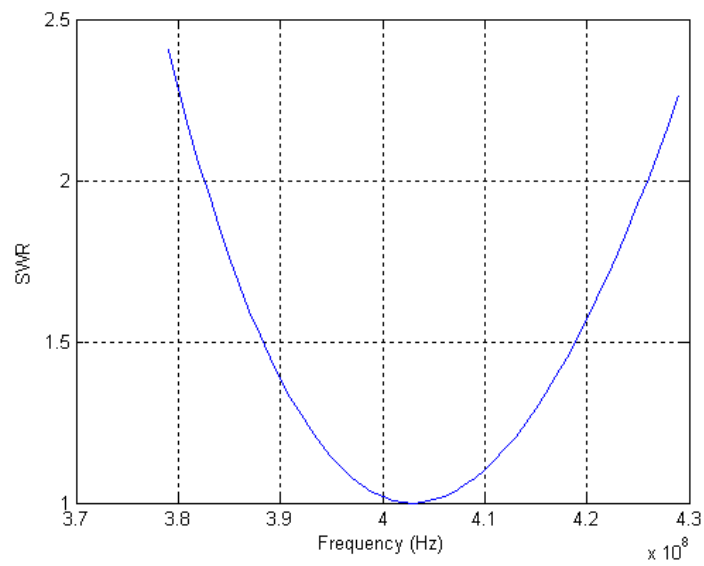Figure 5.14: The real and imaginary parts of the impedance of the circumference antenna in simulated muslce tissue, cf. Table 4.3.

Figure 5.15: The SWR of the circumference antenna in simulated muscle tissue. $Z_0 = 4.8\Omega$
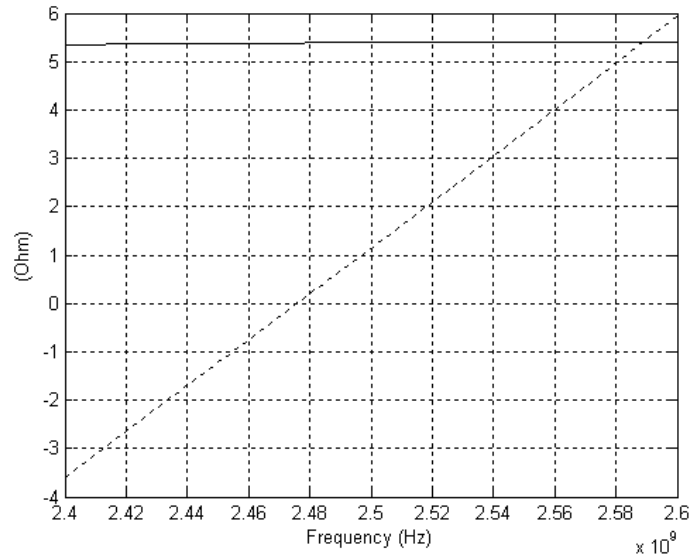
Figure 5.16: The real and imaginary parts of the impedance of the 2.45GHz circumference antenna.

Version for the 2.45 GHz ISM band

The design of the circumference antenna was modified to a resonance frequency of 2.45 GHz. The resulting antenna has a length of 11 mm. The impedance plot of the simulated antenna is given in Figure 5.16 and the SWR in Figure 5.17.

From Figure 5.17 we get that the bandwidth of SWR<2 is wider than the ISM band, which is allocated between 2.4 GHz and 2.5 GHz. As the SWR for a bandwidth of 100 MHz is below 1.1, the antenna has a margin for the movement of the center frequency due to near-field interference of the body interface. The simulation was done with the same dielectric properties as for 403.5 MHz

5.3.4   Circumference plate antenna

In order to increase the bandwidth of the antenna we replaced the wire by a thin metallic plate. The plate was placed at the same distance from the model implant as the wire, and encased in the same plastic. The width of the plate was 8 mm. The impedance plot from the simulation can be seen in Figure 5.19. The SWR is given in Figure 5.20.

From Figure 5.20 we get the bandwidth at SWR<2 to 56 MHz. This is an increase of 33% compared with the circumference wire antenna. The rule from classical antenna design that a wider radiator has a larger bandwidth is thus confirmed in this case for a radiator in a lossy matter.
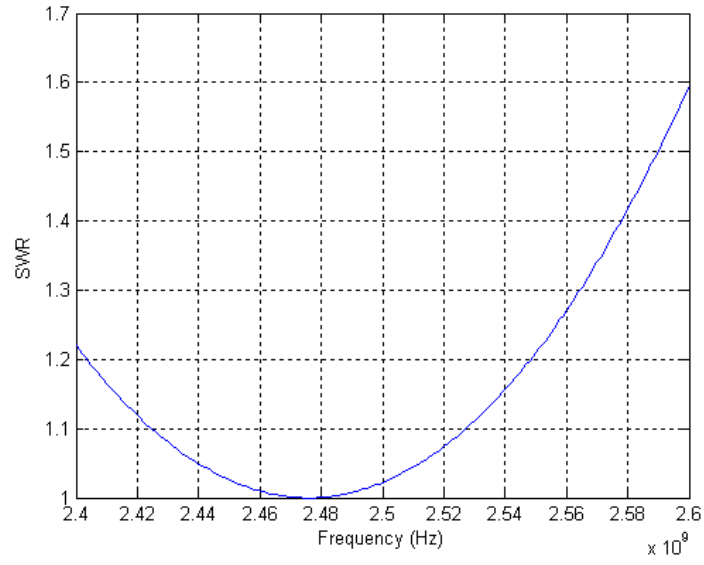
Figure 5.17: The SWR of the 2.45GHz circumference antenna. $Z_0 = 5.5\Omega$

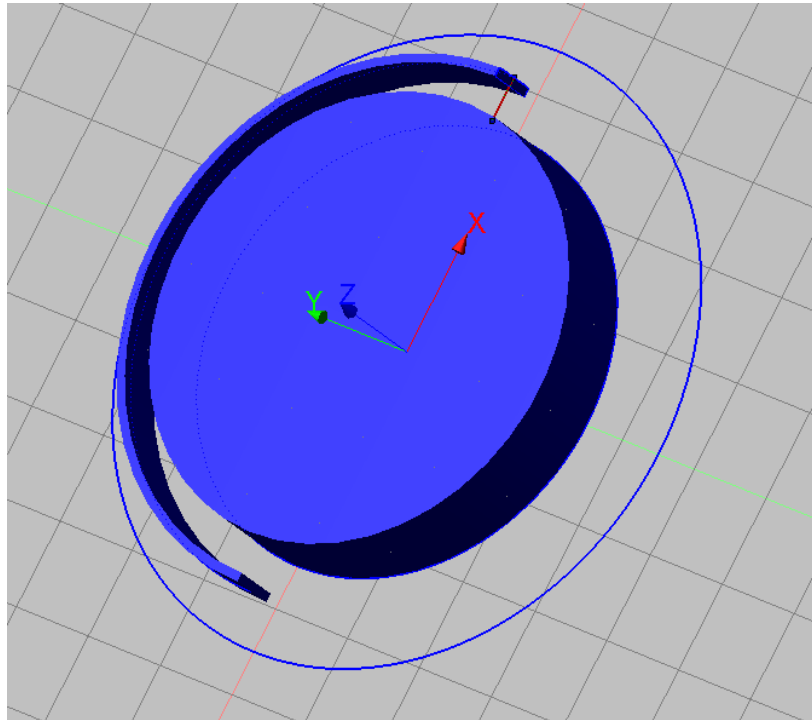|	$\mathbf{Re[Z_0]}$	$\mathbf{f_0}$
Simulation	4 Ω	404 MHz
Measurement	5 Ω	403.5 MHz

Table 5.3: Impedance of the circumference plate antenna.

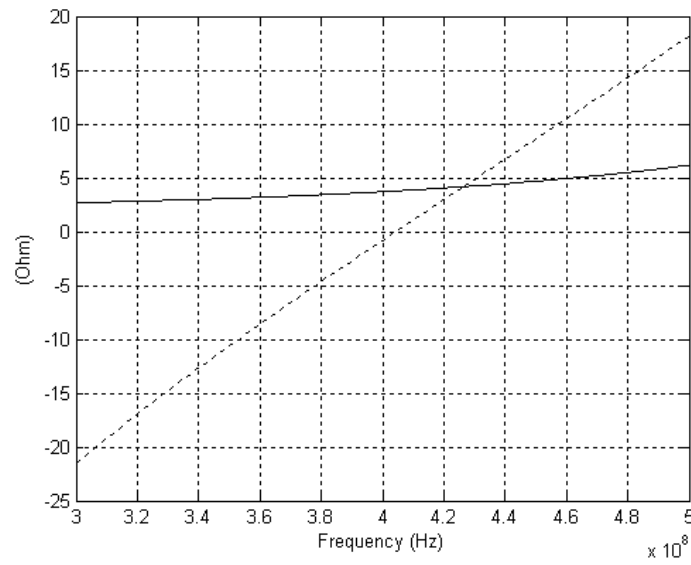Figure 5.18: The CAD drawing of the circumference plate antenna. The thin circle is the radial extent of the isolation

Figure 5.19: Real and imaginary parts of the impedance of the circumference plate antenna in simulated muscle tissue.
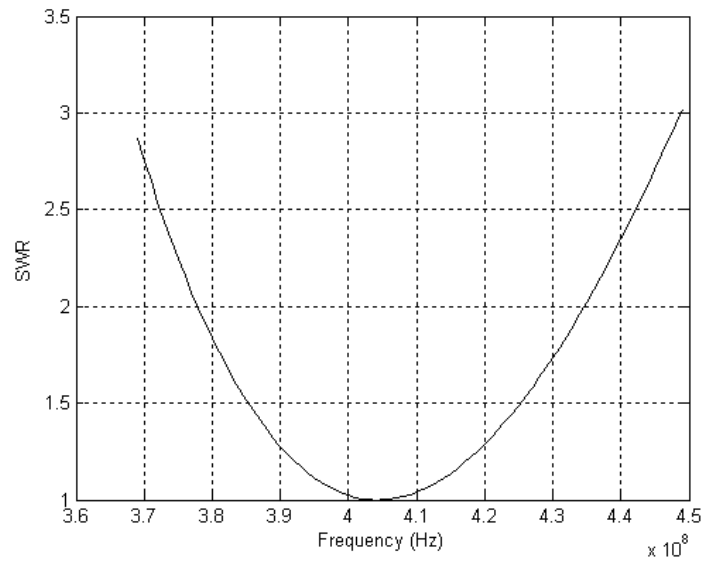
Figure 5.20: The SWR of the circumference plate antenna. $Z_0 = 4 \ \Omega$
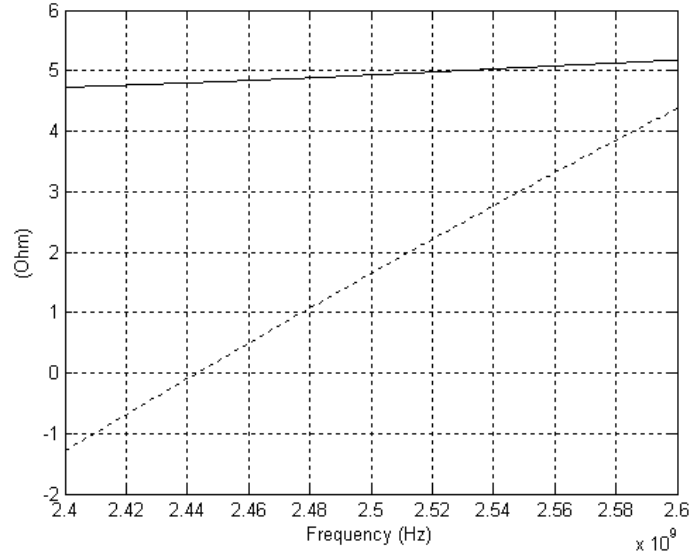
Figure 5.21: Real and imaginary part of the impedance of the 2.45 GHz circumference plate antenna in simulated muscle tissue.

Version for the 2.45 GHz ISM band

The circumference plate antenna was also adapted to the 2.45 GHz band. The results are given in Figure 5.21 and Figure 5.22. The increased bandwidth of the circumference plate antenna in comparison with the circumference wire antenna is visible also at this frequency. The simulation was done with the same dielectric properties as for 403.5 MHz

5.3.5   Circumference PIFA

The circumference PIFA (Planar Inverted F-Antenna) antenna is an adaptation of the Inverted F-antenna (IFA) [34] to the circumference geometry. We implemented it by modifying the circumference plate antenna described above. The result is depicted in Figure 5.23. The added part of the antenna will behave as if an inductance to ground was added at the feed point. . This antenna has the benefit of having an impedance close to 50 ohm, and is thus easy to match to the classical RF impedance standard of $Z_0 = 50\Omega$. The bandwidth is large compared with the circumference antenna. The small oscillations visible in the figures are due to the truncated execution time for the FDTD calculation.
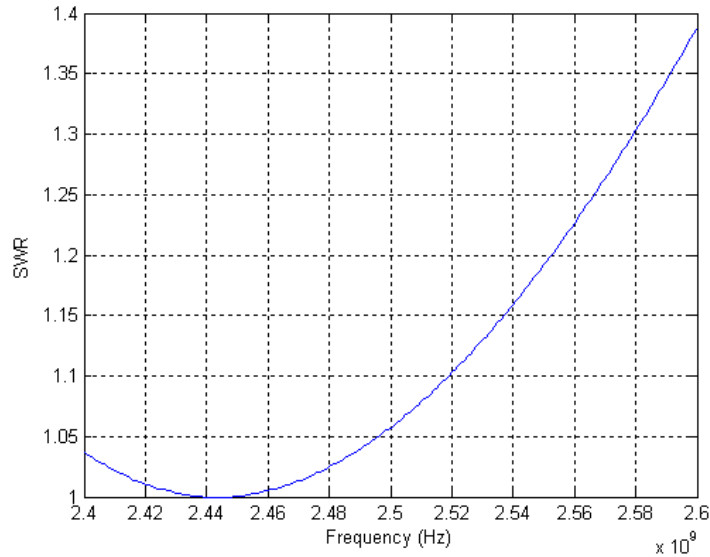
Figure 5.22: The SWR for the 2.45 GHz circumference plate antenna. $Z_0 = 4.8\Omega$

5.3.6 Patch antenna

The patch antenna, at first, seems to be the perfect match for the medical implant. It is compact, small compared with the wavelength, and can be placed on the side of the implant. Unfortunately, we have found that it is difficult to make it to work properly inside a lossy material. Its use as an implant antenna has been patented [45]. In this patent application, there is a reported gain of approximately -32dBi, but it is not clear to us whether this is a calculated, simulated or measured value. In the patent it is reported that the patch antenna has 8 dB better gain than wire and loop antennas, but how these were realized is not reported. The gain is reported as calculated with the body loss subtracted. That method is not useful, as is shown in this thesis.

Our simulations show that a patch antenna placed in a lossy medium does not work well as an antenna. The patch antenna is a resonant structure, with a plate placed over a ground plane. The plate has such dimensions that there will be a standing wave across the patch. It is fed at a position that excites the resonating modes and has a matching impedance to the antenna feed. The space between the patch and the ground plane is often loaded with a dielectric substrate in order to reduce the wavelength and the size of the patch. In our experiments the dielectric has covered the entire ground plane. The patch antenna used in our simulations had a size of 37.4 mm by 28.8 mm on a 1.55 mm thick FR-4 substrate. It was fed by a probe-feed at a point with an impedance of 50 Ω when the patch was in the air.
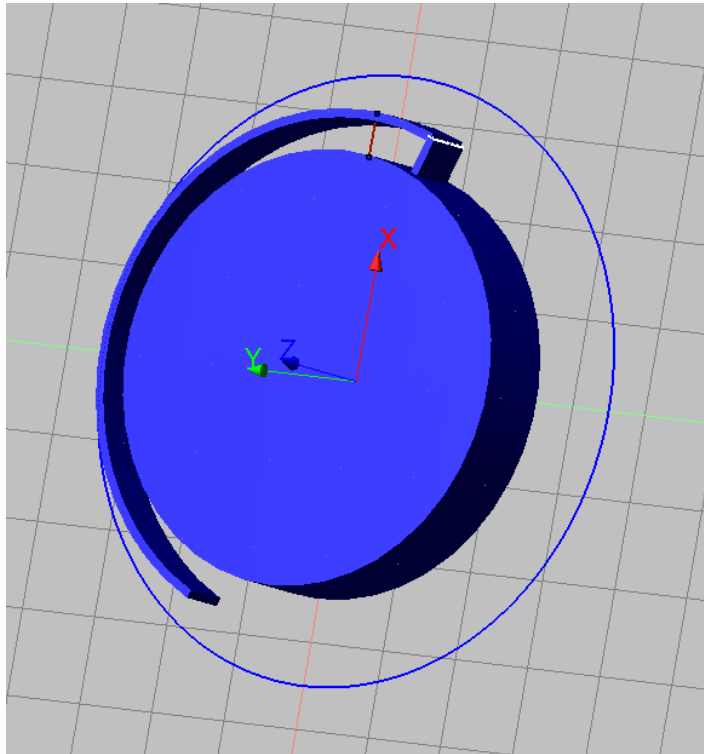
Figure 5.23: The CAD drawing of the circumference PIFA antenna. The thin circle is the radial extent of the isolation
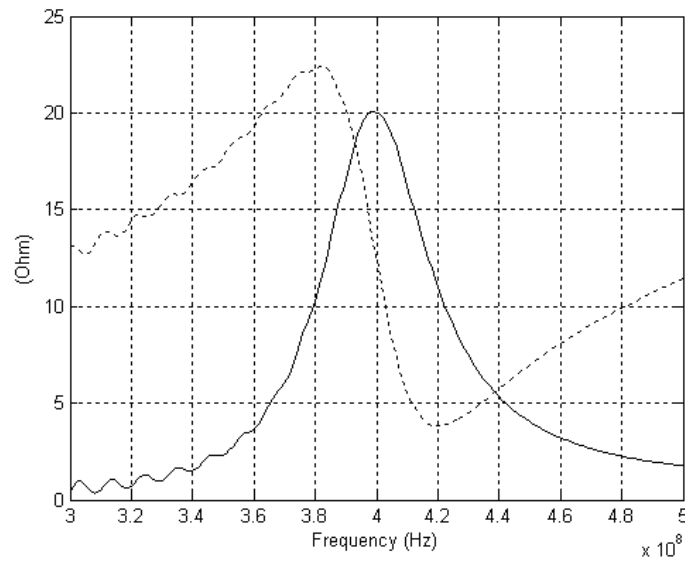
Figure 5.24: Real and imaginary part of the impedance of the PIFA circumference antenna in simulated muscle tissue.
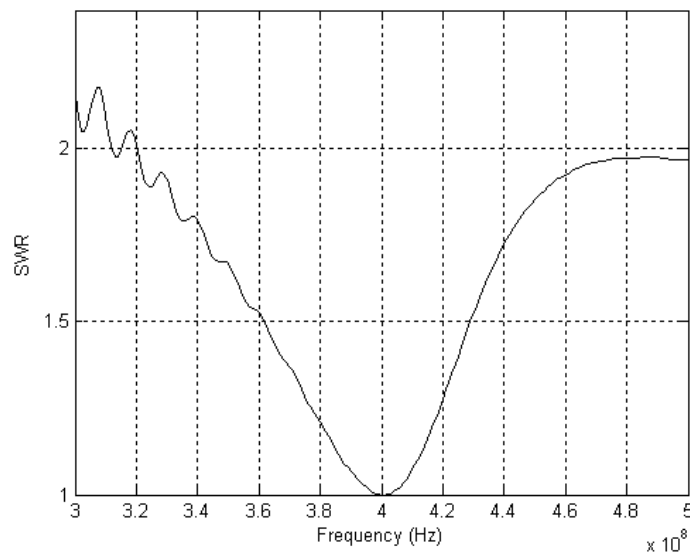

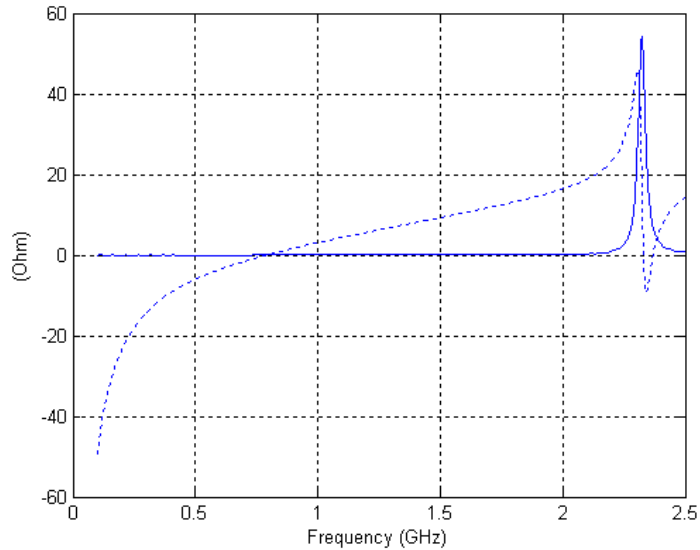Figure 5.25: SWR of the PIFA circumference antenna. $Z_0 = 20\Omega$

Figure 5.26: The impedance of the bare patch antenna in air.

If we place the simple patch antenna in a conducting medium the reflections at the ends of the patch are reduced, since the patch surface is essentially extended infinitely by the lossy matter. The wave propagating between the patch and the ground plane is a surface wave. It is not reflected at the edges of the patch but continues to propagate as an attenuated surface wave. The radiation from this is very small. We thus lose the resonant structure of the patch. The wave propagating into space gives rise to a far-field, but if the wave impedance of the space between the patch and the ground plane does not equal the wave impedance of the matter the efficiency of this "horn"-like antenna will be low.

Figure 5.26 shows the simulated impedance of the patch antenna in air. The antenna is designed to be resonant at 2.45 GHz. This is confirmed by the simulation and measurements. Figure 5.27 shows the same patch antenna in the muscle tissue. There are no resonance phenomena taking place anymore. This has also been confirmed by measurements. Figure 5.28 shows the simulated impedance when we have covered the patch and dielectric with a thin insulation, h=1.5mm. No useful resonance is present. If we cover the antenna with a thicker insulation, h=5 mm, we get the result shown in Figure 5.29. We now have a resonance, but we have no benefit of the high permittivity in the tissue. The patch has a resonance when the length equals half a wave-length. Care must be taken to calculate the correct effective permittivity, as the electric field will be both above and beneath the patch[28]. If we have a thick insulation, we can use the permittivity of the insulation as a rough estimate, in this case $\varepsilon_r = 4$.
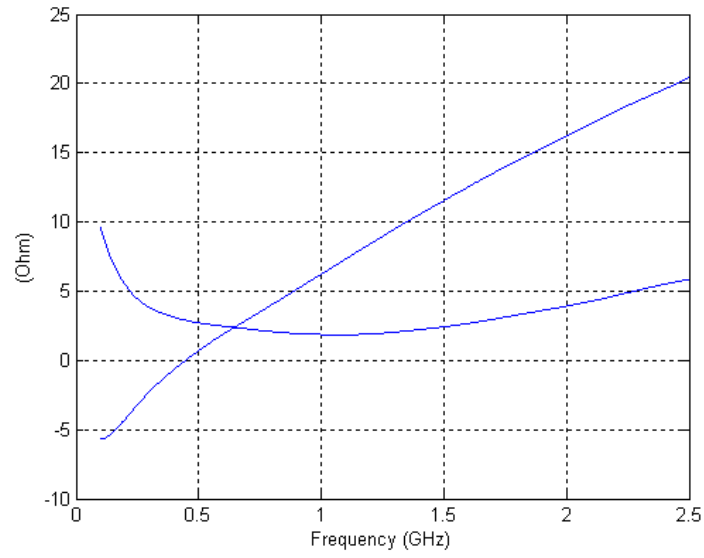
Figure 5.27: The bare patch antenna in the muscle tissue.
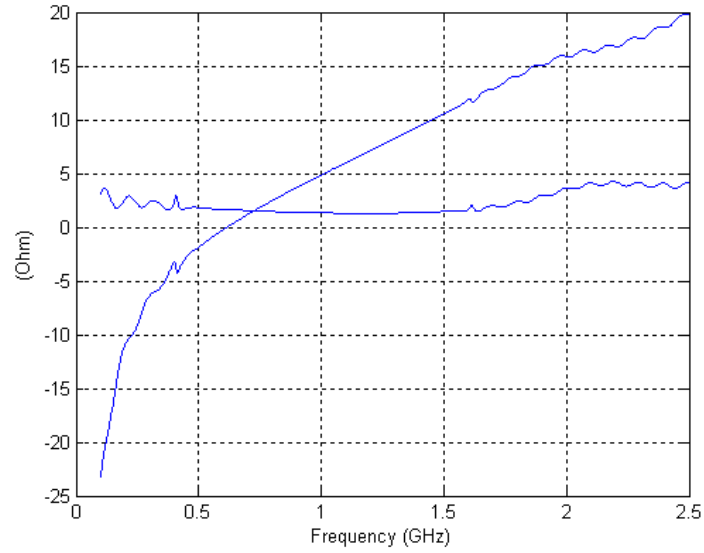

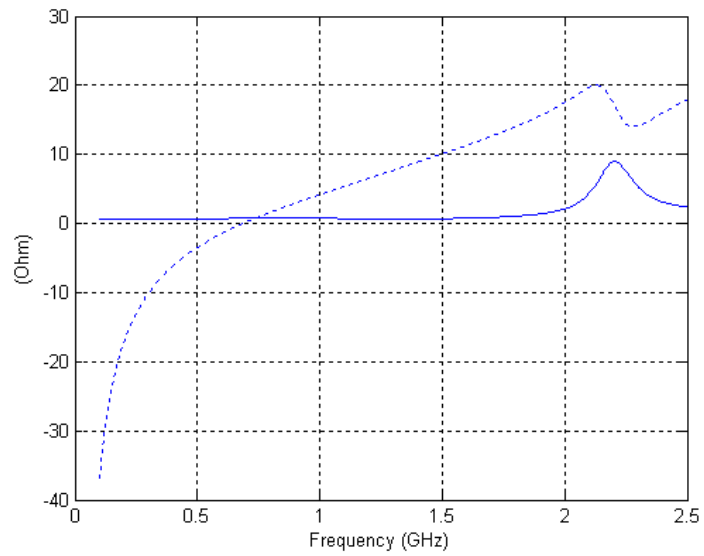Figure 5.28: The patch antenna with thin isolation in muscle tissue.

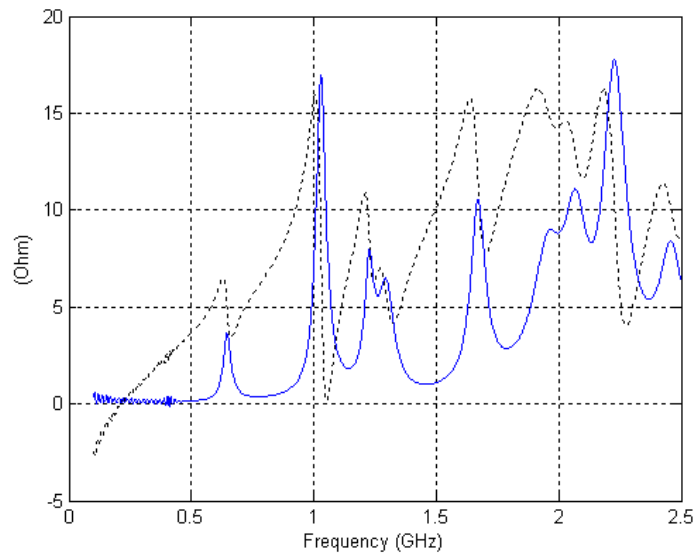Figure 5.29: The patch antenna with thick (5mm) isolation in muscle tissue.

Figure 5.30: The patch antenna with thick isolation in the muscle tissue. The dielectric has a high permittivity: $\varepsilon_r = 50$.

That gives a length of the patch at 403.5 MHz of 18 cm, which is too large to be useful in a medical implant. If we increase the permittivity of the dielectric to $\varepsilon_r = 50$, we get the result in Figure 5.30. Here we have a reduction of the resonant frequency. There are a couple of drawbacks with this solution. One is that it requires high epsilon materials, a second is that the antenna makes the implant thicker. Most implants today are designed to be flat rather than compact. There are examples of patch antennas being used for hyperthermia applications in the literature [60], and they use a thick insulation between the patch and the lossy tissue.

It is possible to get a compact patch design if the dielectric is confined to the space beneath the patch, and the muscle tissue is allowed to flow around and down to the ground plane. This requires a dielectricum with a higher permittivity than the muscle tissue, or $\varepsilon_r > 60$. This patch will have a very low efficiency, since the lossy muscle tissue is in contact with the near-field of the radiating sides of the patch.

5.3.7 Magnetic antenna

As shown in Chapter 4, the magnetic field is increased at the interface between the air and the body, and an antenna operating as a magnetic antenna should then be advantageous. This is further emphasized by the discussions in section 4.3, where it was shown that the magnetic dipole has low ohmic losses in the surrounding media. Ferrites are often used to improve the performance of magnetic antennas. The ferrite material has an upper frequency limit, over which the permeability of the material falls. We found that the frequency limits of the available ferrites were below 400 MHz, and a design without a ferrite core was made.

A magnetic coil antenna is inductive at low frequencies. There is a capacitive coupling between adjacent turns of the coil. Thus, each turn constitutes a resonant circuit. The self-resonance frequency of each turn of the coil is proportional to

$$f_r \propto \frac{1}{2\pi\sqrt{L_e C_t}} \tag{5.36}$$

where C_t and L_e in a homogenous non-conducting medium are approximately given by, cf. [61].

$$C_t = \frac{2\pi^2 a \varepsilon_r \varepsilon_0}{\cosh^{-1}\left(\frac{c}{b}\right)} \tag{5.37}$$

$$L_e = \mu_0 \frac{N^2 A}{l} \tag{5.38}$$

Here a is the radius of the loop, b is the wire radius, c is the distance between turns, N is the number of turns, $l = Nc$ is the length of the coil and $A = \pi a^2$ is the area of the loop. Below the frequency f_r the coil is inductive, above it is

capacitive. In order to have an effective magnetic antenna it should be used at a frequency below the self-resonance. The self-resonance frequency is dependent on the product $L_e C_t$. We expand the product $C_t L_e$ in 5.36

$$C_t L_e \propto \frac{N a^3}{c \cosh^{-1}\left(\frac{c}{b}\right)} \tag{5.39}$$

The radiation resistance in free space is given as [28]

$$R_{rad} = 20\pi^2 \left(\frac{2\pi a}{\lambda}\right)^4 N^2 \tag{5.40}$$

In order to get an efficient antenna the radiation resistance R_{rad} should be as high as possible. Then both N and a should be large. However, in Equation 5.39 we see that this increases the product $C_t L_e$, and thus reduces the resonance frequency. Thus, the radius should be made as large as possible. The relative permittivity ε_r should be minimized. The turns should be placed with a large distance c and the number of turns should be as large as possible in order to increase the radiation resistance.

The loop antenna is inductive and must be resonated with a capacitance in series. The design was taken to resonate with a capacitance of 2 pF, for practical reasons. This gave a design with a total inductance of 78 nH, following

$$\omega = \frac{1}{\sqrt{LC}} \tag{5.41}$$

With a wire diameter of 0.3 mm and a radius of the coil of 2.5 mm, this gives a total number of 7 turns. This antenna was built. The coil was wound around a plastic core and isolated with plastic on the outside to isolate it from the surrounding medium. When the impedance was measured with the coil immersed in the simulated muscle tissue, we obtained an impedance of $Z = 21 + j198$ Ω. The 2 pF capacitor has a reactance at 403.5 MHz of -197 Ω. A second capacitor was added in series and the values were adjusted to impedance match the antenna to 50 Ω. If the antenna was adjusted to a resonance frequency of 403.5 MHz in air the resonance frequency was reduced by 6 MHz when the antenna was placed in the tissue. The impedance was also dependent on the depth at which the antenna was placed. The values given are for a deep placement where the values were constant. Qualitative measurements of the power radiated from the MICS phantom, which showed that it was radiating energy, and the performance was as good as for the circumference antenna.

5.4 Dependence on insulation thickness

The thickness of a non-conducting insulation has a major impact on the antenna performance of all antenna types. Simulations were done to investigate this effect. The circumference PIFA antenna was simulated with different thickness of the radial insulation. The result is shown in Figure 5.31. As can be expected the

Thickness	Frequency	Efficiency
5mm	403.5 MHz	100%
4mm	373 MHz	92%
3mm	358 MHz	83%
2mm	321 MHz	62%
1mm	233 MHz	12%

Table 5.4: Center frequency and efficiency variation with covering isolation thickness in the PIFA antenna. The efficiencies are given relative to the case with 5 mm of insulation thickness.

resonant frequency of the antennas was lowered, due to an increased effective permittivity in the medium surrounding the antenna. Simulations were then repeated in order to evaluate the difference in radiation efficiency between the different antennas and frequencies. (The antenna was not redesigned to 403.5 MHz for all the insulation thickness.) The resonant frequencies and the corresponding relative radiation efficiencies are given in Table 5.4. The result is that an insulation thickness of at least 3 mm is required for the PIFA antenna in order to get good radiation efficiency.

5.5 Dependence on surrounding matter

A series of simulations were done with the circumference antenna where it was placed in different layered structures in order to test the sensitivity of the antenna to the immediate surrounding tissues. The geometries are shown in Figure 5.32. The main reason for the investigation was to analyze the influence of the surrounding matter on the resonant frequency. A large variation of the resonant frequency would require a larger bandwidth of the antenna in order to get the same performance over different surroundings. The resulting SWR curves are shown in Figure 5.33. There is a marked dependency on the surrounding tissue. A closer investigation of the sensitivity has been postponed until more realistic human phantoms have become available to us.

5.6 SAR

The Specific Absorption Rate (SAR) was calculated for the circumference antenna variants and the wire antennas. SAR is the absorbed power, in W/kg, averaged over a certain volume. This volume is moved around the antenna and the maximum value is recorded. The values were calculated according to a draft of the specification SCC-34, SC-2, WG-2, IEEE-P1529/D0.0 [62]. The standard for mobile phone certification in Sweden [63] prescribes SAR to be calculated over the maximum 10 g volume. The limit for SAR is 2 W/kg over 10 g. In USA the FCC has set the limit to 1 W/kg over 1 g. If we take the density of the tissues to be 1 kg/dm^3, 10 g corresponds to an integration over a cube with a
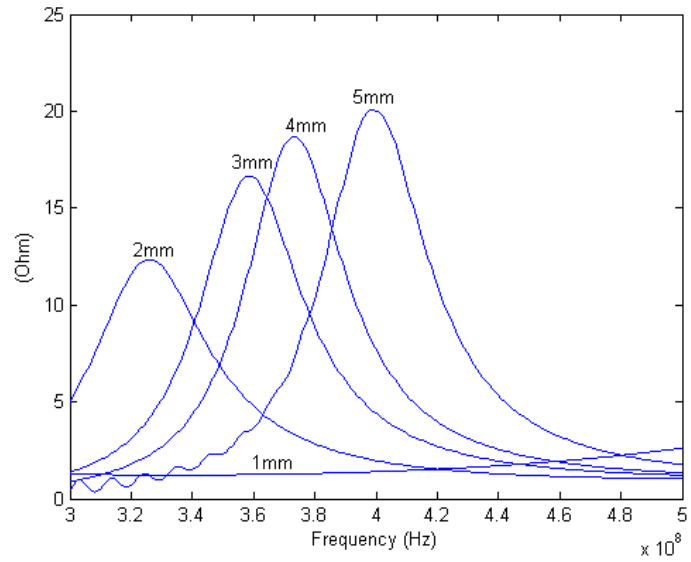
Figure 5.31: Variation of the real part of the PIFA impedance with the insulating thickness on the outside of the antenna.
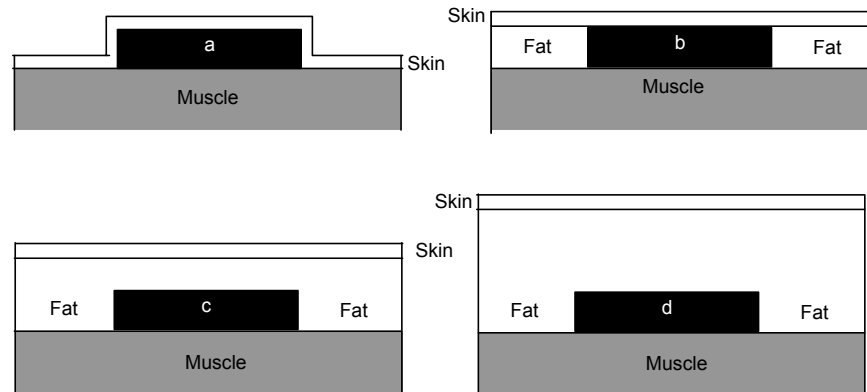

Figure 5.32: The four test cases for the circumference wire antenna. The skin layer is 3 mm thick. The fat layer is 0 mm, 10 mm, 20 mm, 50 mm, respectively.
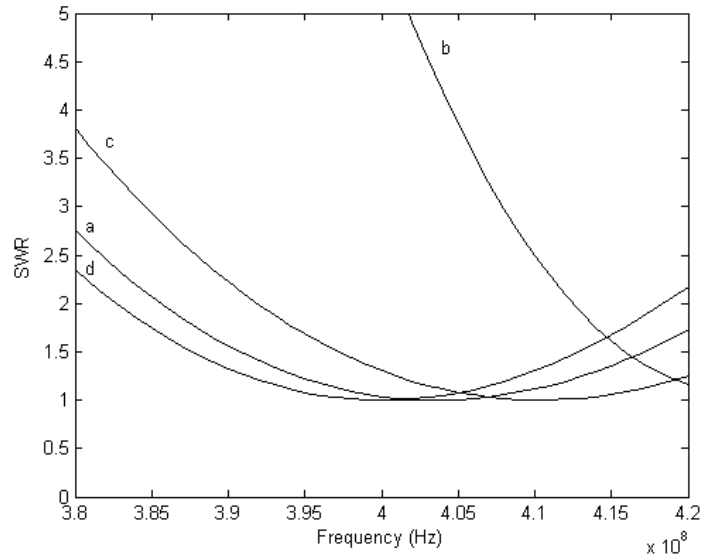
Figure 5.33: The dependency of the resonance frequency on the surrounding tissues.

side of 2.15 cm and a volume of 10 cm^3. This is four times the thickness of our model implant. In order to investigate the very local peaks of the absorption, SAR was calculated over three different volumes, 10 g, 1 g and 1 mg, where the 1 mg corresponds to a cube with a side of 1 mm. The results are presented in Table 5.5 and the table is normalized to 1 W input power into the antenna. If 1 mW, or 0 dBm, is used as the power to the antenna, all values should be divided by a factor of 1000. All the antennas are then below the Swedish limit. Devices with a mean output power below 0.02 W do not need to be tested in Sweden, as they are not assumed to give a SAR above the limit [63]. Our simulations verify this assumption in the tested antennas, as the antenna with the highest SAR, the un-insulated wire antenna, gives a SAR of 1.0 W/kg in 10 g when fed with 20 mW of continuous power. The FCC has a proposal [64] that devices worn at the body with an output below 2 mW should be exempt from licensing. This would give the un-insulated wire antenna a SAR of 0.6 W/kg over 1 g when fed with 2 mW of continuous power. This is below the FCC limit of 1.6 W/kg.

5.7   Conclusion

The result from this chapter is that the circumference type antennas and the magnetic coil antenna are the most interesting ones for medical implant applications. The patch antenna is not very well suited for placement inside a lossy

	SAR (W/kg)		
Antenna	**10 g**	**1 g**	**1 mg**
Un-insulated Wire	52	300	7900
Isolated Wire	4.3	12	47
Circumference Wire	8.1	14	150
Circumference Plate	8.3	22	260
Circumference PIFA	8.0	21	240

Table 5.5: SAR levels of the implanted antennas.

matter, unless it is well insulated from the matter. It will then loose the benefit of having a small volume.

The circumference antenna is more conforming to an existing antenna shape than the coil antenna, which, on the other hand, has a smaller total volume. The theoretical calculations point in the direction that the magnetic antenna should have a larger gain in the case of a perfectly conducting antenna coil. On the other hand, it has larger resistive losses in the coil wire in an actual implementation than the wire type antennas.

Chapter 6

Influence of Patient

When we place a medical implant with an antenna inside a patient, the antenna will be affected by the immediate surroundings. Thus, the antenna behaves differently if placed in an arm, deep in the abdomen or just beneath the skin in the chest. In addition to this there will be a dependency on the surrounding tissue type, for example variations in the subcutaneous fat layer. This layer varies in thickness between patients and varies also over time, when a patient gains or loses weight. As will be shown, the far-field from the antenna is affected by the patient's size, body shape and position. We have investigated some of these effects by numerical simulations for an implant placed in the chest region of a human. This has been done in order to characterize the magnitude of the variations and to be able to set levels for the excess loss in the link budget calculations. We have also investigated the influence of the shape of the body depending on age and sex.

Movements of the patient change the immediate surrounding of the implanted antenna. The MICS frequency band, 402-405 MHz, corresponds to a wavelength of approximately 74 cm in air and approximately 9 cm inside the body. The body surface is in the near-field of the implanted antenna. Any change of the permittivity or conductivity of materials placed in the near-field of an antenna changes its radiation characteristics. Thus, a change in posture changes the far-field pattern and affects the radio channel between the medical implant and the external base station. This variation of the channel corresponds to a kind of slow fading. It was known at an early stage of the project that the posture of the patient influences the far-field of an implanted antenna [65].

The gain, directivity and efficiency of an antenna were defined in Chapter 5. The antenna has an efficiency factor η, $0 \leq \eta \leq 1$,which is a measure of how much power is lost in ohmic losses in the antenna and in the body. If the antenna is lossless then $\eta = 1$, which is impossible to get for an implanted antenna. The antenna is taken to be perfectly matched. Thus, reflection losses due to mismatch are not included in the gain. In this chapter the gain is determined in the far-zone of the body, which is in air, and this makes the gain and the directivity independent of the origin. The gain taken from simulations

in this thesis is scaled in dBi, or decibels relative an isotropic antenna. An isotropic antenna is a theoretical construction that radiates equally well in all directions.

6.1   Method

We built the different phantoms as described in Appendix E. As excitation we used the wire antenna connected to our standard pacemaker model, or the circumference wire antenna. The simulations were done in SEMCAD, as in the previous chapter. As absorbing boundary condition Mur [66] was used in order to reduce the simulation time.

6.2   Gain variation from movement of the arms

The variation of the gain pattern of the antenna from arm movement has been simulated with the FDTD method in SEMCAD. The phantom's arms were adjusted to the eight different positions shown in Figure 6.1 in order to get an estimate of the variation. We investigated the movement of the arms since they are very movable and close to the implant and thus close to radiating parts of the body, as can be seen in Figure 6.2. Large movements of the arms were chosen in order to maximize the possible influence of the position on the antenna gain.

The first antenna to be investigated was a straight wire antenna through the vertical axis of the male phantom. This is not a very realistic representation of an implanted antenna, but it is a position of the antenna that is easy to keep constant between different postures and different phantoms. In this way it reduces the influence of the placement of the antenna on the results. The antenna is illustrated in Figure 6.3. The cylindrical implant is 50 mm in diameter and has a thickness of 10 mm. An un-insulated wire antenna goes straight down (inferior direction) for 370 mm. A 50 ohm voltage source is placed between the antenna and the implant. The resulting far-fields are shown in Figures 6.4, 6.5 and 6.6. The sagittal, frontal and transversal planes are defined in Appendix A.

The variation of the gain between the different arm positions is given in Table 6.1. The maximum gains in each of three primary cuts are given (transversal, sagittal and frontal). In addition, the maximum gain for the complete unit sphere is also shown. The variation of the maximum gain between arm positions is not larger than 1 dB, except in the frontal plane where the variation is 4 dB. Both the arms are, in position 1, placed in the frontal plane, as can be seen in Appendix 2. When the arms move the geometry of the phantom in this plane vary significantly, which is a plausible explanation for the increased sensitivity of the far-field pattern in the frontal plane. The mean gain for each position is also given in Table 6.1. The variation of the mean gain is larger, and gives position 7 as the most disadvantageous one.

The radiation efficiency for an implanted antenna is defined as in Chapter 5:
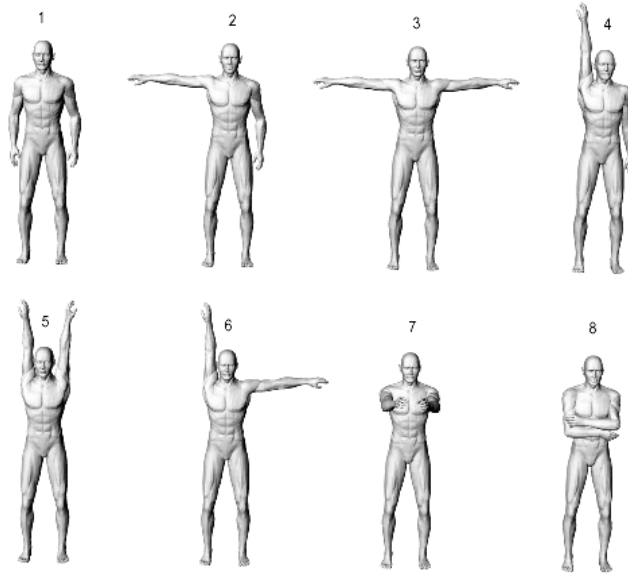
Figure 6.1: The eight arm positions used in the evaluation of the directive gain pattern variation.

$$Radiation\ efficiency = \frac{Total\ radiated\ power\ from\ the\ body}{Accepted\ power\ into\ the\ antenna} \qquad (6.1)$$

Notice that this radiation efficiency is taken in a loss-free surrounding, and thus it is independent of the origin. From this definition it is concluded that position 7 is the least efficient one. This may be explained by noticing that the maximum radiation from the phantom is in the forward direction, as can be seen in Figure 6.7. Thus, the position of the arms in position 7 is the one where the arms most directly interfere with the main lobe of the gain pattern. This position also shows the worst radiation efficiency of the eight, as can be seen in Table 6.2.

From the data in Figures 6.9, 6.10 and 6.11 we obtained the results in Table 6.3. It follows that the necessary reduction of the gain is 12 dB, in order to cover 95% of the circle in the three planes. If we consider a standing or sitting patient the transversal plane is the dominant radiation direction to a base station in chest height, and the 95% coverage reduction is 4 dB. The deepest nulls are placed in the posterior part of the radiation pattern and will be relevant if we consider continuous monitoring of an ambulant patient in a room.
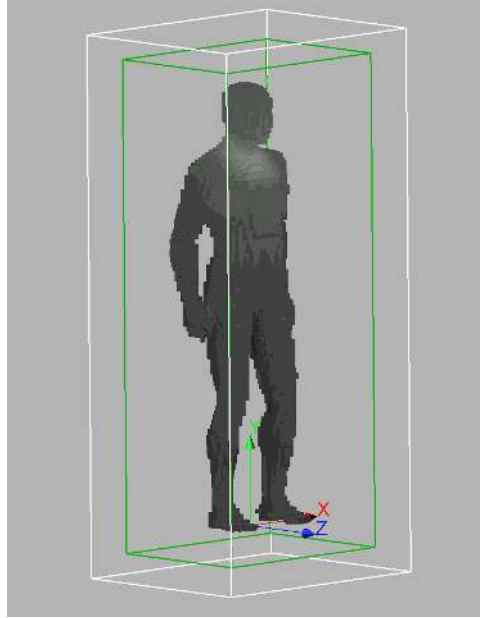
Figure 6.2: The currents on the surface of the body generated by the antenna in position 1. Light parts correspond to strong currents.

Position	Transversal Max/Mean(dBi)	Sagittal Max/Mean(dBi)	Frontal Max/Mean(dBi)
1	-31/-33	-29/-33	-30/-33
2	-31/-32	-29/-33	-30/-33
3	-31/-32	-29/-33	-30/-33
4	-31/-33	-29/-33	-29/-33
5	-32/-34	-28/-33	-28/-33
6	-31/-33	-29/-33	-29/-33
7	-31/-34	-29/-35	-32/-35
8	-31/-32	-30/-34	-30/-32

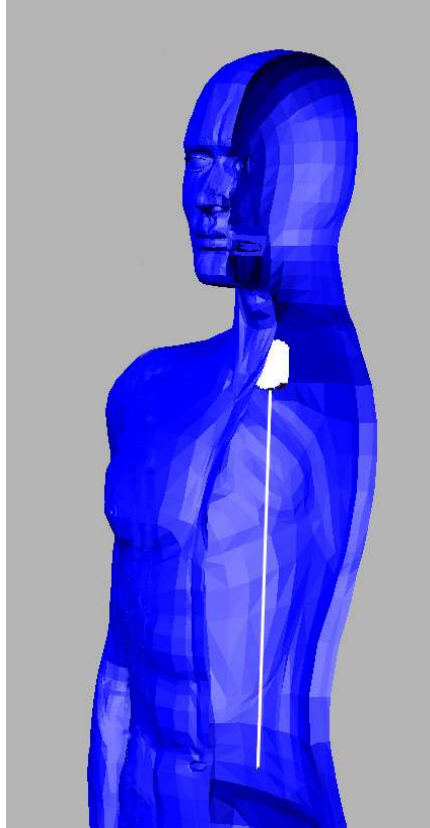Table 6.1: Maximum gain and mean gain in dBi for the different cuts.

Figure 6.3: The position of the simulated implant with wire antenna.

Position	Total Sphere Max (dBi)	Radiation Efficiency 10^{-4}
1	-29	5.1
2	-29	5.1
3	-29	5.1
4	-29	4.7
5	-28	4.4
6	-29	4.6
7	-29	3.8
8	-30	4.5

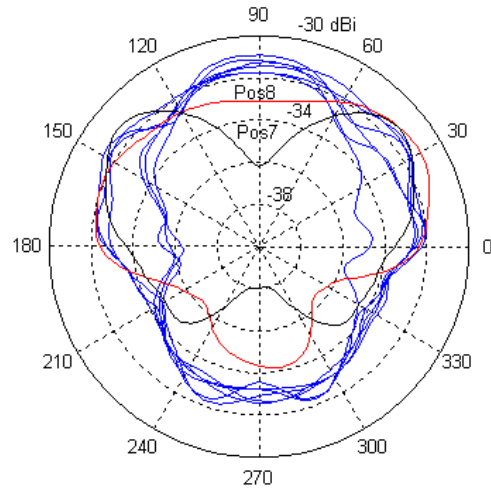Table 6.2: The maximum gain and the radiation efficiency for the 8 arm positions.

Figure 6.4: The gain of the 8 different arm positions in the transversal plane of the phantom.
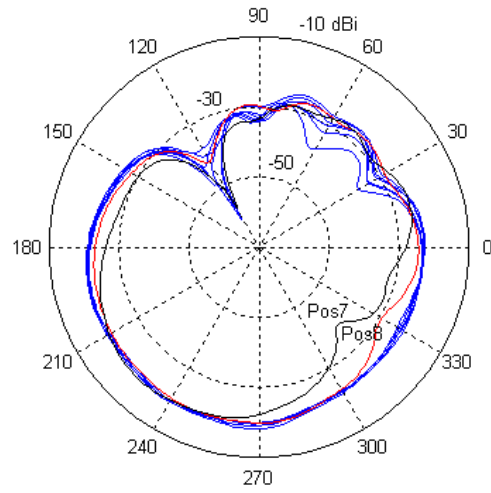

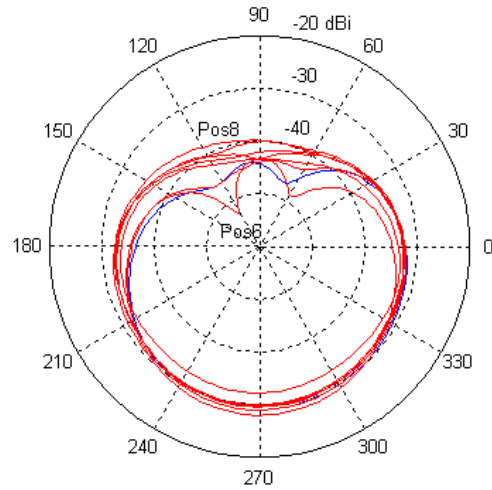Figure 6.5: The gain of the 8 different arm positions in the sagittal plane.

Figure 6.6: The gain of the 8 different arm positions in the frontal plane.

Plane	Coverage			
	90%	95%	97%	99%
Transversal	4.4 dB	4.5 dB	4.5 dB	4.6 dB
Sagittal	8.7 dB	11.4 dB	13.2 dB	14.9 dB
entry	6.7 dB	8.0 dB	9.0 dB	10.7 dB

Table 6.3: Necessary reduction of the gain in order to account for a given percentage of the angles in given planes.
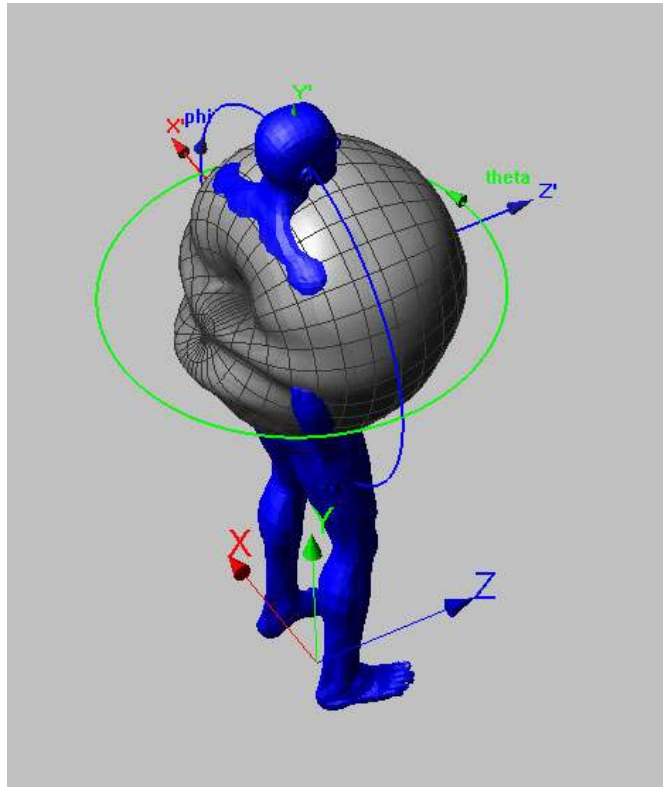
Figure 6.7: 3D presentation of the Gain pattern from position 1. The main lobe is in the forward, anterior, direction of the phantom.
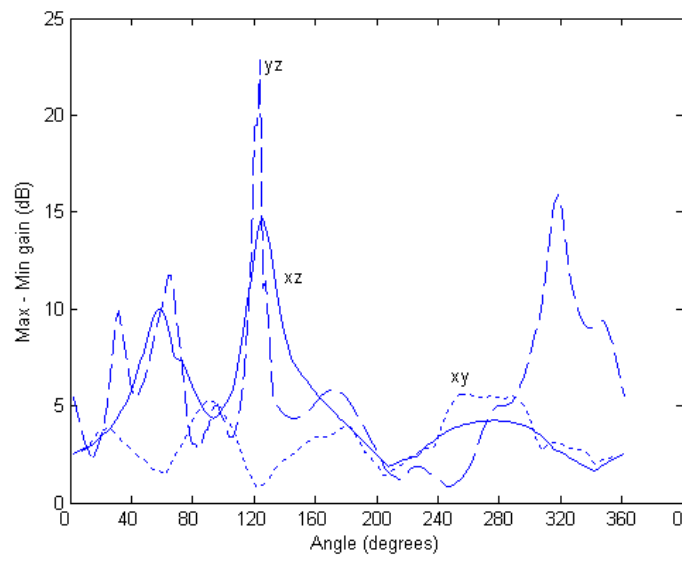
Figure 6.8: Gain variations between the 8 positions at each angle. The three curves correspond to the three cuts: transversal (xy), sagittal (yz) and frontal (xz).
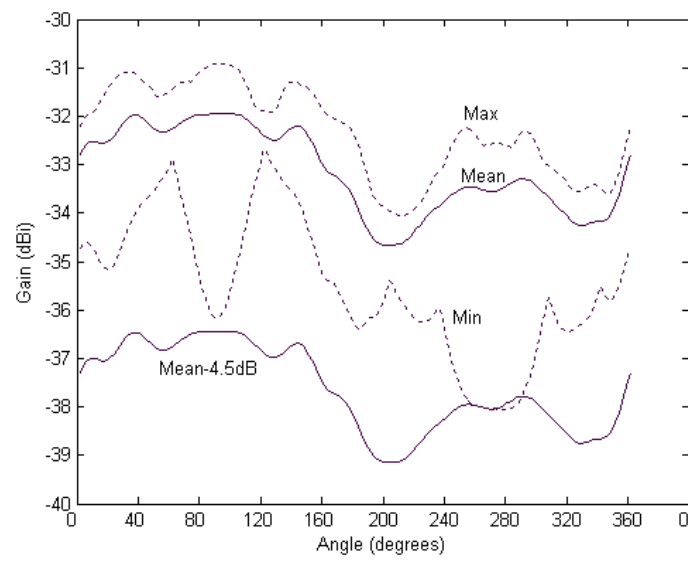
Figure 6.9: The variation of the gain in the transversal plane. The mean, maximum and minimum gain over the different arm positions are plotted. The margin for 5% angle outage probability is also plotted.

Figure 6.10: The variation of the gain in the sagittal plane. The mean, maximum and minimum gain over the different arm positions are plotted. The margin for 5% angle outage probability is also plotted.

Figure 6.11: The variation of the gain in the frontal plane. The mean, maximum and minimum gain over the different arm positions are plotted. The margin for 5% angle outage probability is also plotted.
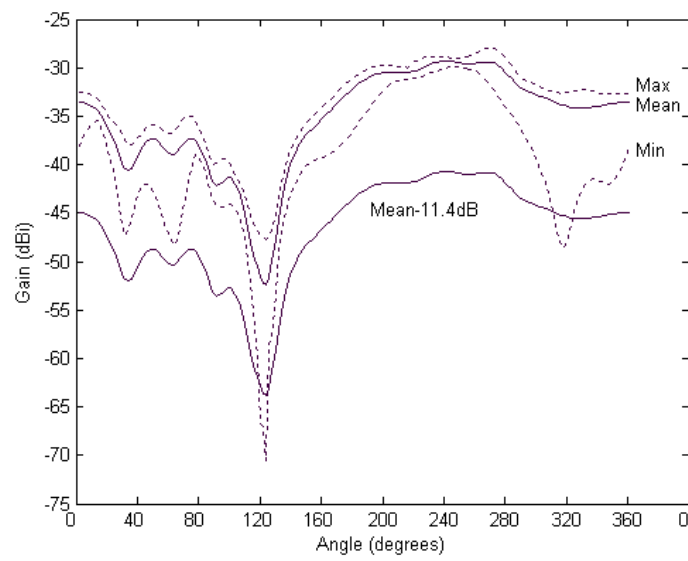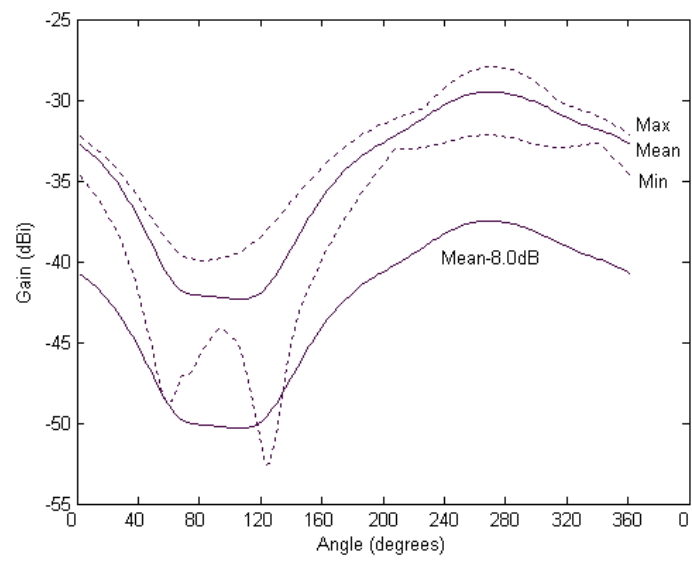
6.3 Gain dependence on body size and shape

Body size and shape of the patient depend on the sex and the age of the patient. In order to investigate the influence of these on the gain pattern, simulations were done with the same antenna inserted into different phantoms. We use the same configuration, with the straight wire antenna, as was used to investigate the dependence on arm movements above. The antenna was inserted into three different phantoms: a male, a female and a child, shown in Figure 6.12. All were of the initial Poser configuration, i.e., an idealized human shape. Their respective lengths are given in Table 6.4. The table also gives the radiation efficiency of the three phantoms. They vary +/-10% around the mean efficiency of 0.057%. This shows that we have a strong dependence on the phantom size and shape. The maximum gain from the phantoms is within 1 dB.
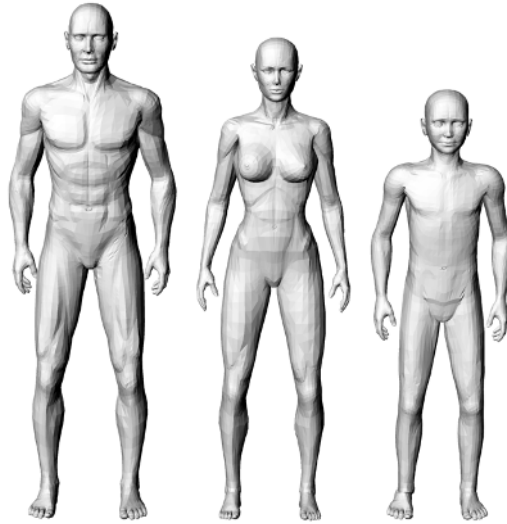

Figure 6.12: Male, Female and Boy phantom used in the simulations.

Phantom	Length	Radiation Efficiency	Max Gain (3D)
Man	179.4 cm	$5.1 \cdot 10^{-4}$	-29 dBi
Woman	168.5 cm	$6.1 \cdot 10^{-4}$	-28 dBi
Boy	151.0 cm	$5.8 \cdot 10^{-4}$	-29 dBi

Table 6.4: Scaled size of the phantoms.

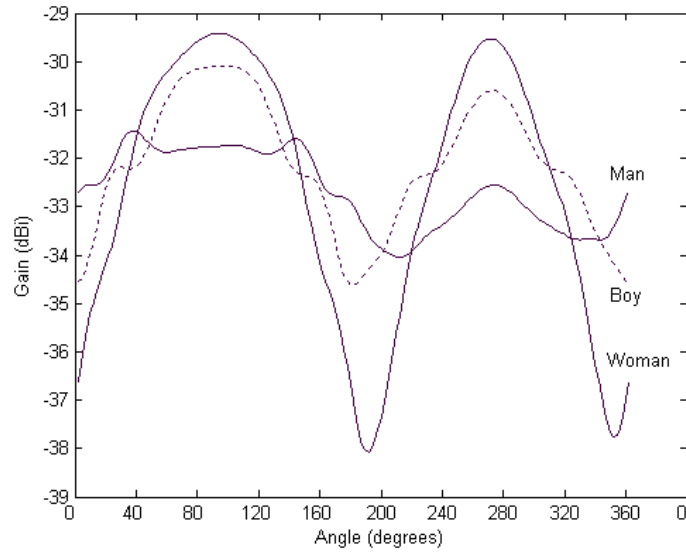The polar gain plots are shown in Figures 6.13, 6.14 and 6.15. The gains

Figure 6.13: Gain variations between phantoms in the transversal plane.

of all three phantoms in the same plane are plotted in each figure. The large variation is very noticeably. The placement of a null influences these graphs a lot. Hence, the deepest nulls should be left aside. In the lobe directions there are variations up to 3-6 dB between the different phantoms.

Plane	Gain variation
Transversal	4.6 dB
Sagittal	0.8 dB
Frontal	4.2 dB

Table 6.5: The gain variations with the male phantom as reference.

The gain variation with the male phantom as reference is given in Table 6.5. The largest difference is seen in the transversal plane, which is also the plane where the line of sight component of the link is, when the patient is standing up or sitting down, and with the base station antenna at chest height.

6.4   Circumference antenna in phantoms

The circumference antenna described in Chapter 5 was inserted into the male, woman, boy and baby phantoms. An evaluation of the MICS standardized phantom was one of the goals of the investigation. The phantoms were simulated
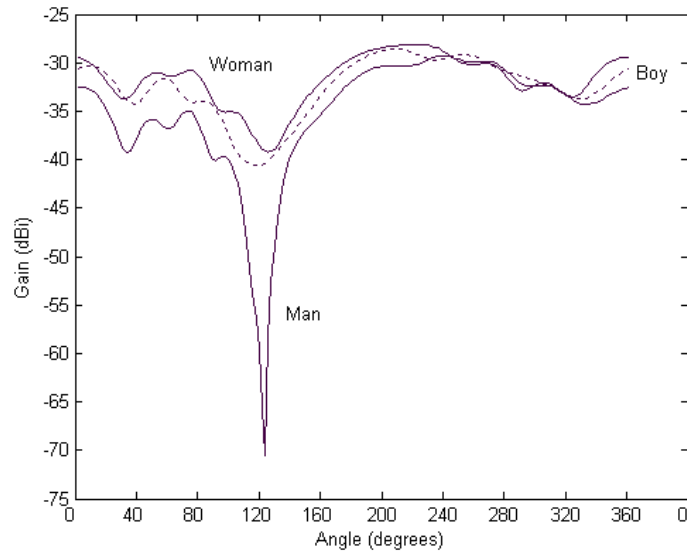
Figure 6.14: Gain variations between phantoms in the sagittal plane.
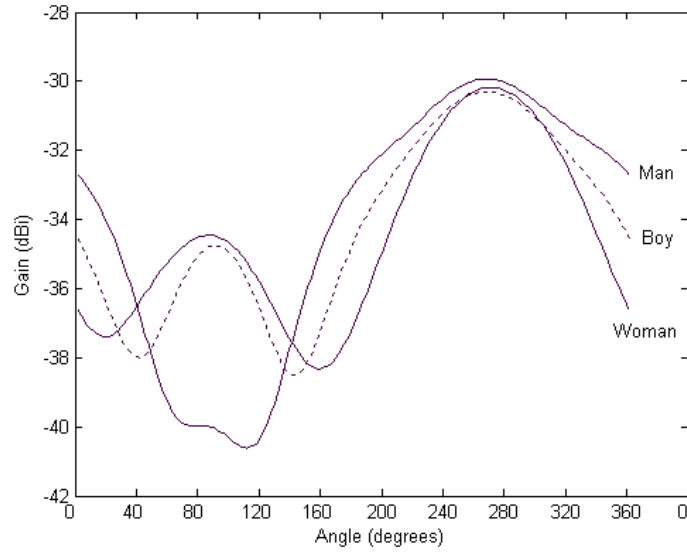

Figure 6.15: Gain variations between phantoms in the frontal plane.

as filled with a substance with the same characteristics as the muscle simulating liquid described in Chapter 4. The legs and arms beneath the elbow of the phantoms were not included, in order to reduce the simulation time. The size of the baby phantom was small enough for it to be simulated without reduction, as can be seen in Figure 6.16. The pacemaker was implanted at approximately the same place in the male, female and boy phantoms. The placement in the male phantom is shown in Figure 6.17. In the baby phantom the implant was placed in the abdomen, as illustrated in Figure 6.18. The size of the implant made it impossible to place it realistically in this small phantom below the left clavicle. The lower abdomen is also used in real life implantation as an implantation spot for pacemakers [4]. The implants were placed at least 10 mm from the surface of the phantoms. The scaled heights of the phantoms are given in Table 6.6. The comparisons are here made in the XY, YZ, and XZ planes of the pacemaker. From the simulations we see that the direction of maximum radiation is related to the pacemaker axis. The orientation of the pacemaker varies between the phantoms with regard to the planes of the phantoms. From this follows that the performance is improved relative to the straight wire antenna. This is expected, since the antenna now is closer to the surface of the phantoms than the centrally placed wire antenna. The maximum gain is increased by 3-6 dB and the radiation efficiency by 1.5 to 3 times. The difference can be reduced by increasing the phantom size. The far-field radiation pattern is also dependent on the size and shape of the phantom. The variation between the largest and the smallest gain in a certain direction is between 1 dB and 9 dB in the recorded radiation planes, as can be seen in Figure 6.26. From the gain plots in Figures 6.23, 6.24 and 6.25 it can be noted that the gain pattern from the male phantom is the lowest at most points. If we use the male phantom as the reference, we need to add 3.4 dB of margin to account for body size variations, according to this study.

Phantom	Full Height	Phantom Reductions
Baby	75 cm	
Boy	151 cm	Legs
Woman	169 cm	Legs, arms below elbow
Man	179 cm	Legs, arms below elbow

Table 6.6: Height of the phantoms including legs.

6.5 Validation of MICS phantom

The MICS standard defines a phantom to be used in order to measure compliance with the limit of -16dBm or 25μW EIRP. The MICS phantom consists of a cylinder with a diameter of 30 cm that is filled to a height of 76cm with a tissue simulating liquid. The liquid has the same electromagnetic properties as muscle, at the frequency band of interest. The ETSI standard [14] gives a
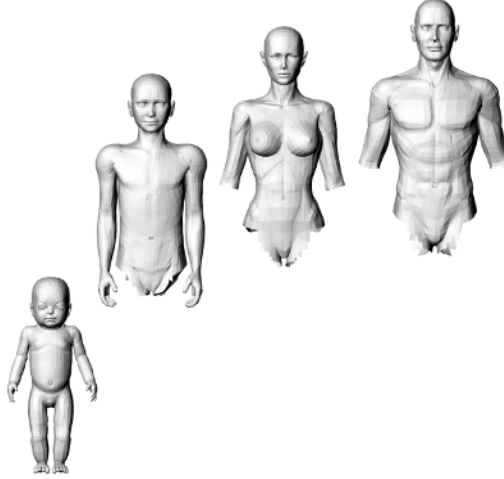
Figure 6.16: The reduced phantoms used in the simulations with the circumference antenna.

Phantom	Max Gain	Radiation Efficiency	Gain difference
Baby	-25.5 dBi	$1.31 \cdot 10^{-3}$	NA
Boy	-23.0 dBi	$1.83 \cdot 10^{-3}$	+6 dB
Woman	-23.6 dBi	$1.36 \cdot 10^{-3}$	+4 dB
Man	-26.3 dBi	$0.78 \cdot 10^{-3}$	+3 dB

Table 6.7: Maximum gain and radiation efficiency from the circumference antenna implanted in the phantoms. The gain difference is relative the straight wire antenna.

Plane	Gain variation
XY	3.4 dB
YZ	2.4 dB
XZ	2.0 dB

Table 6.8: The reduction of the gain necessary to account for the different body sizes with the male phantom as the norm.
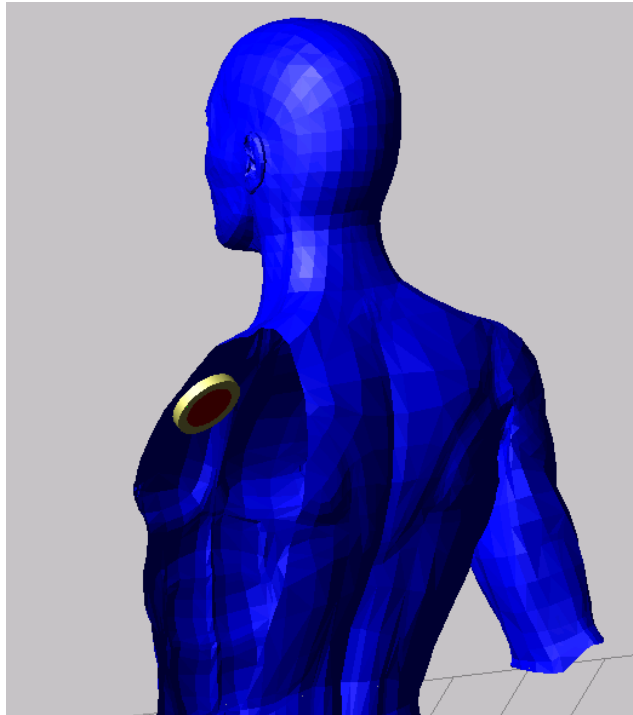
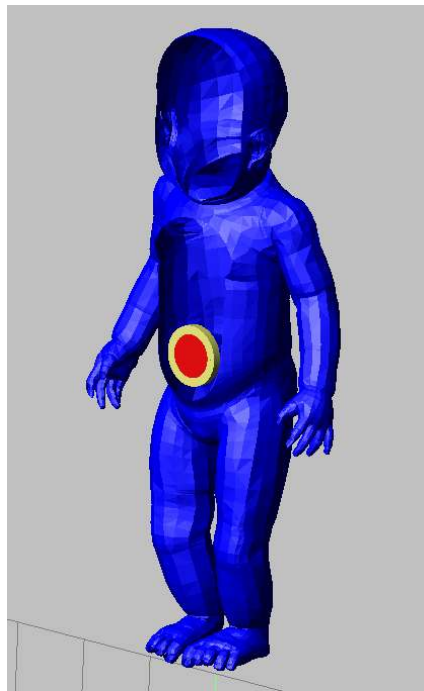Figure 6.17: The placement of the pacemaker in the male phantom.

Figure 6.18: The placement of the pacemaker model in the baby phantom. Part of the phantom is removed to show the implant.
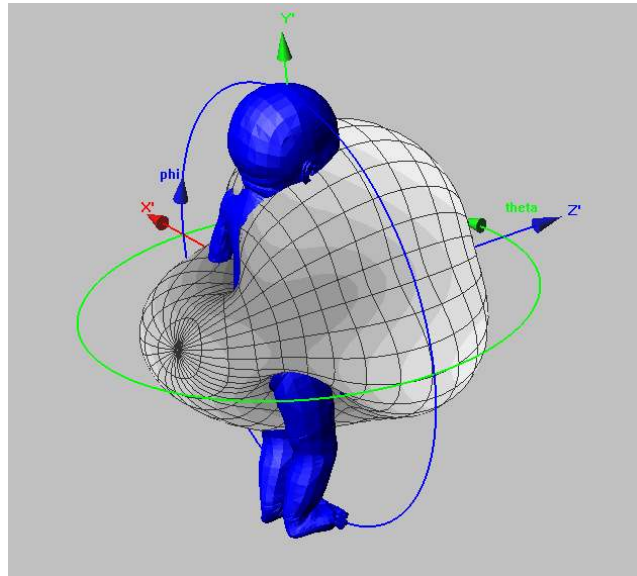
Figure 6.19: 3D visualisation of the radiation pattern from the baby phantom with implanted circumference antenna.

reference to a liquid described in [24]. The plastic cylinder should have a wall thickness of 6.35mm, or 1/4 inch.

As described in Section 2.6, the device under test (DUT) should be placed at a plastic grating 60 mm +/-5 mm from the sidewall with its center at a height of 38cm from the bottom. Any extending antenna should be placed at the same height and follow the sidewall of the cylinder at the same distance. Any other cables should be coiled and placed away from the antenna and 60 mm from the sidewall. The implant should be placed in the same orientation as it would have in a patient standing up. Since the distinction between the vertical and horizontal positions was unclear, they were excluded from the study. The MICS phantom is used for evaluating the EIRP of the DUT by measuring the field strength in the far-zone and relating it to an absolute level by a dipole substitution method. The direction of maximum radiation in horizontal or vertical polarization should be found and the EIRP in this direction recorded.

To validate the MICS model it was compared with two anthropomorphic phantoms. A nude male and a nude female phantom from the program Poser were used. These are the same phantoms as were used in the previous section and are shown in Figure 6.16. The models were truncated at the hip and below the elbow in order to reduce memory requirements and to reduce the simulation time. These models were scaled to a height of 185 cm for the male and 169 cm for the female. They were simulated as homogenous bodies consisting of the same liquid as in the MICS phantom.
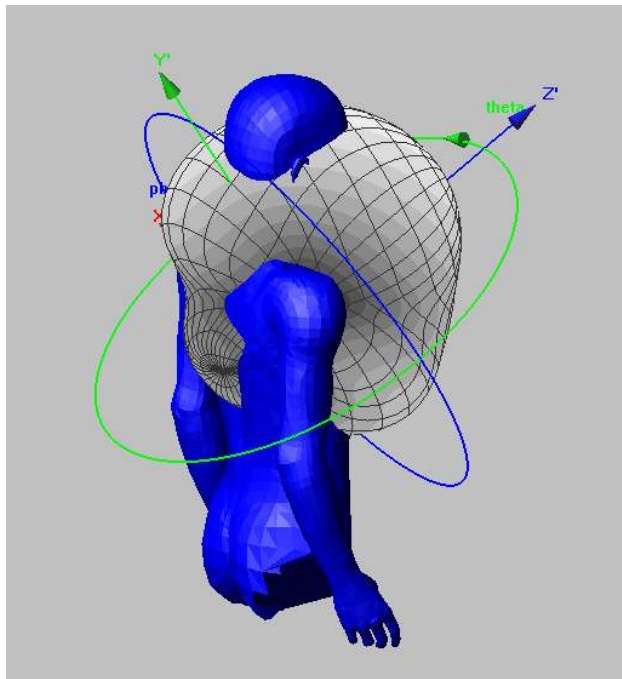
Figure 6.20: 3D visualisation of the radiation pattern from the boy phantom with implanted circumference antenna.
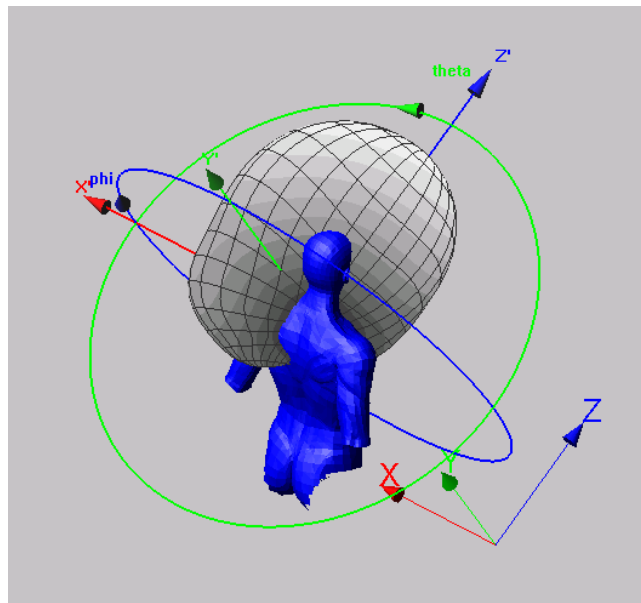
Figure 6.21: 3D visualisation of the radiation pattern from the male phantom with implanted circumference antenna.
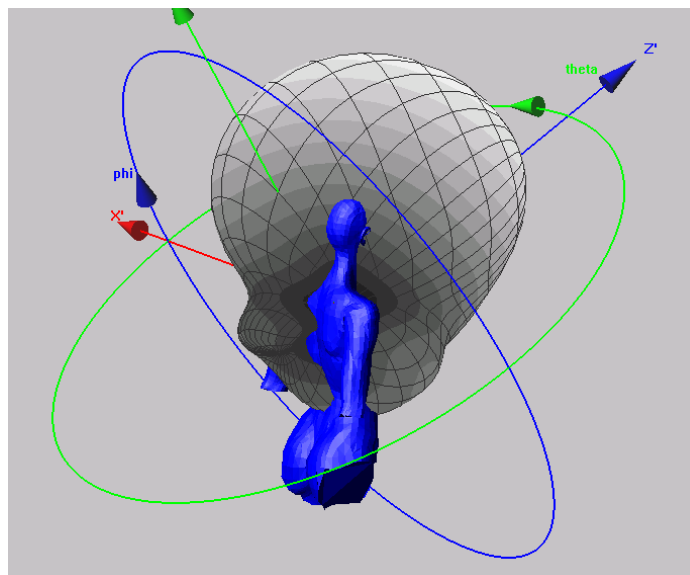
Figure 6.22: 3D visualisation of the radiation pattern from the female phantom with implanted circumference antenna.
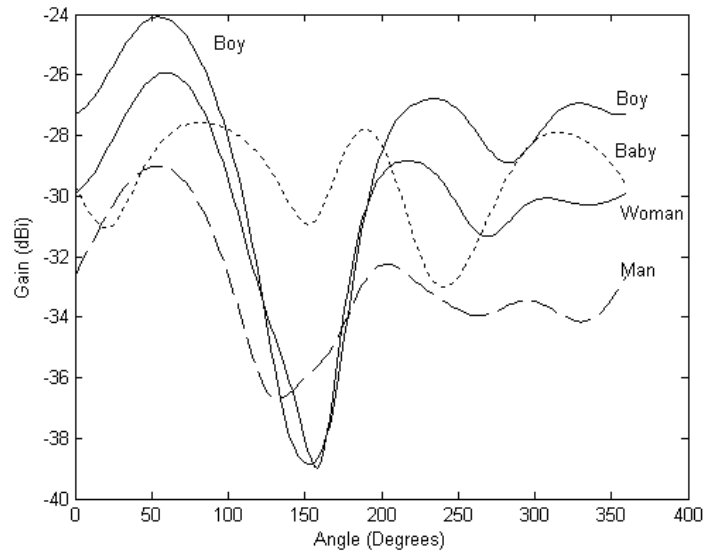
Figure 6.23: Gain from the implanted circumference antenna in the XY plane.
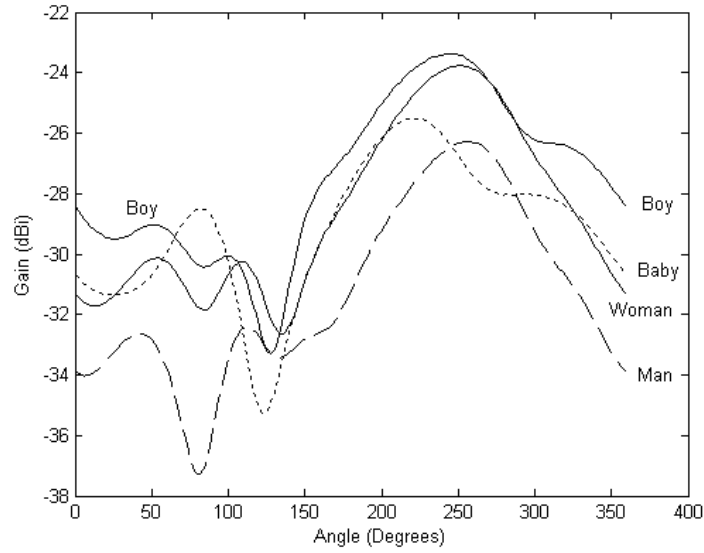
Figure 6.24: Gain from the implanted circumference antenna in the YZ plane.
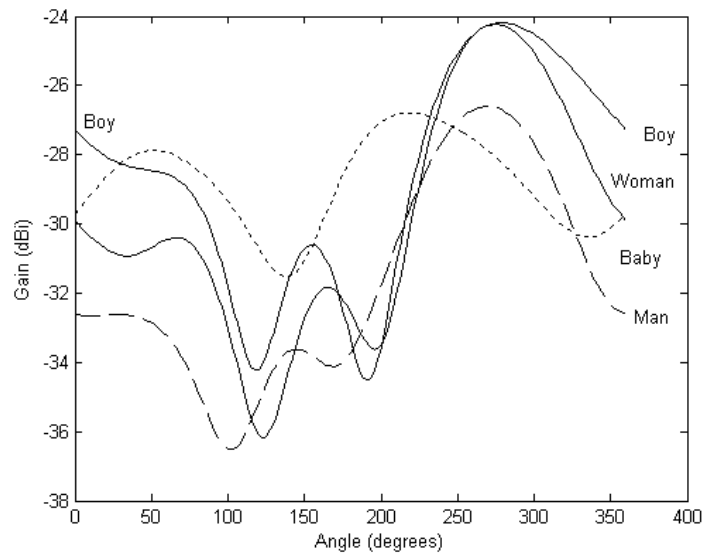
Figure 6.25: Gain from the implanted circumferential antenna in the XZ plane.
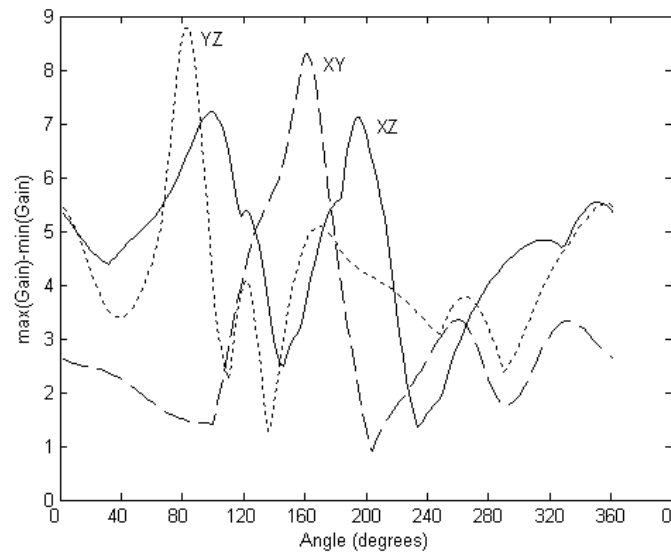
Figure 6.26: The difference between the maximum gain and the minimum gain within the four different phantoms as a function of radiation plane and angle.
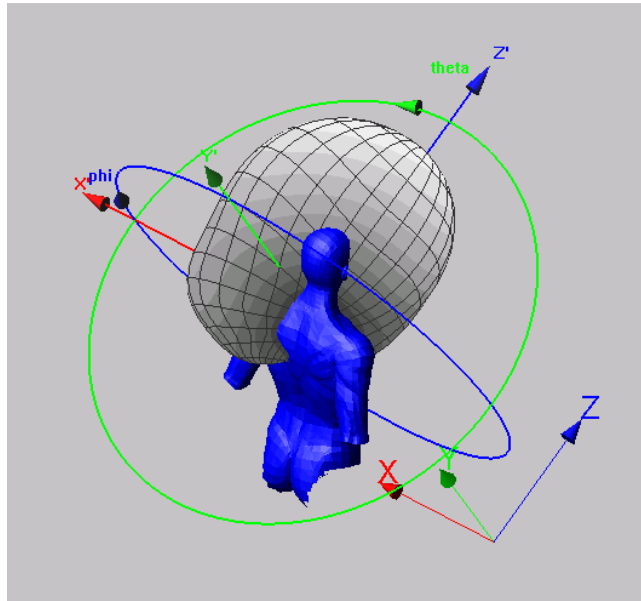
Figure 6.27:

The DUT used in the simulations was a 1cm high metal cylinder with a diameter of 5 cm, which was equipped with a circumferential antenna inside a plastic isolation along the perimeter. The antenna is described in more detail in Chapter 5. In the MICS phantom, the DUT was placed according to the specification. In the anthropomorphic phantoms, the DUT was placed in one of the positions used in actual pacemaker implantations: inferior to the left clavicle and oriented flat against the wall of the chest. To emulate a subcutaneous placement the DUT was placed 10 mm from the surface of the phantom. The placement in the male phantom is shown in Figure 6.17.

6.5.1   Simulations

To evaluate the different phantoms, the maximum gain of the antennas was calculated by a transient FDTD simulation. The gain was extracted at a frequency of 403.5MHz, which is the center frequency of the MICS band. Pictures of the resulting three dimensional gain plots are shown in Figures 6.27, 6.28 and 6.29. The plots are all shown from a vantage point above and behind the phantom in order to show more details of the gain variations.

Note that the y-direction is not "vertical" for the anthropomorphic phantoms. The coordinate system is oriented in relation to the implant, which is inserted at an angle in these phantoms, as can be seen in Figures 6.27 and 6.28. The interesting property to compare between the different phantoms is the value
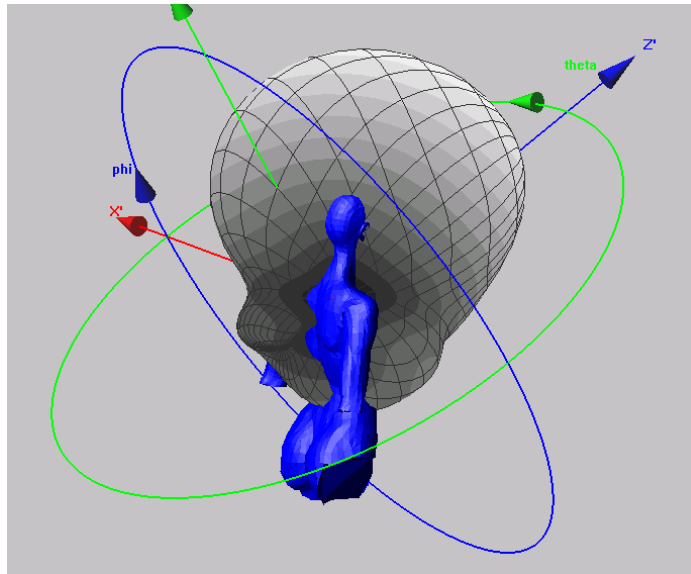
Figure 6.28:

Figure 6.29:

of the maximum gain. The values are shown in Table 6.9. The difference in gain between the anthropomorphic phantoms and the MICS phantom is 7 dB for the male phantom and 10 dB for the female phantom.

Phantom	MICS	Male	Female
Gain (max)	-33 dBi	-26 dBi	-23 dBi

Table 6.9: Maximum gain from different phantoms

6.5.2   Placement sensitivity

Three simulations were done with the pacemaker at different depths in order to investigate the sensitivity of the placement of the pacemaker in the anthropomorphic phanto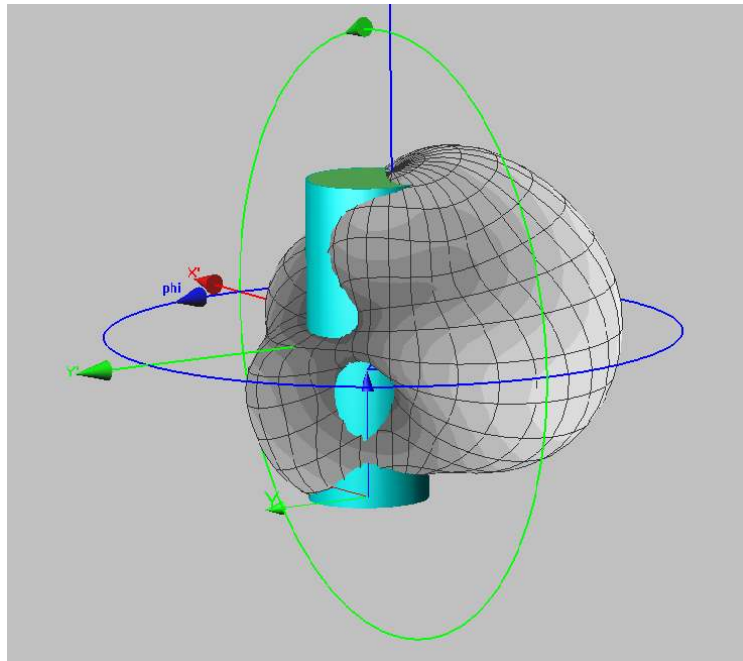ms. Then the position of the pacemaker was varied 5 mm towards and away from the surface of the male phantom. The results are shown in Table 6.10 and indicate that the variation with implantation depth is small (1 dB). A small error in the placement of the DUT in the anthropomorphic phantoms does not explain the large variation in the gain from the DUT between the different anthropomorphic phantoms.

Implantation Depth	Gain
5 mm	-25 dBi
10 mm	-26 dBi
15 mm	-26 dBi

Table 6.10: Gain variation with implantation depth in the male phantom

The reason for the lower gain in the MICS phantom can be attributed to the relatively large depth of the placement of the pacemaker. An additional series of simulations were done in order to investigate the dependence of the maximum gain on the depth of the placement of the pacemaker in the MICS phantom. The radial depth was changed between 65 mm and 5 mm. The resulting maximum gains are shown in Table 6.11, and the data is plotted in Figure 6.30. From this we can make some important observations. The gain is dependent on the depth of the placement. By reducing the depth of the placement, it is possible to get a maximum gain similar to that of the male phantom, but not to the female phantom. The shape of the phantom is still important. Furthermore, the increase in gain with the reduction of the insulation thickness falls off when we get close to the surface of the liquid. This is due to that the plastic wall and the air are in the reactive near-field region of the pacemaker antenna, and there is not a dominant propagating wave between the pacemaker and the wall. The closest distance was 5 mm between the edge of the pacemaker model and the plastic wall. This still gives a distance of 9 mm for the center of the pacemaker model. The lower gain in the MICS phantom than in the anthropomorphic phantoms suggests that a pacemaker that fulfils the MICS specification in the

Depth	$\mathbf{G}_{\max}(dBi)$
5 mm	-27.0
10 mm	-27.2
20 mm	-27.6
30 mm	-29.4
40 mm	-31.3
50 mm	-32.7
60 mm	-33.3
65 mm	-33.9

Table 6.11: Simulated values of maximum gain from implant in MICS phantom at different depths.

Position	Max. Gain	Variation 99%
Laying	-31 dBi	20 dB
Standing	-30 dBi	
Optimal	-30 dBi	12 dB

Table 6.12: Gain variation in the transversal plane, measured with vertical polarization.

test case may exceed the maximum EIRP when implanted into an actual human being.

6.6   Linear polarization

Up to now all of the results presented in this chapter have been calculated with the assumption of optimal polarization matching between the transmitter and the receiver. If instead we assume that the base station is fitted with a singular vertical polarized antenna, and that there is no rotation of the polarization plane in the propagation of the wave, we will get an additional polarization loss. To exemplify this the gain from the male phantom is shown in Figure 6.31. The gain is shown in the transversal plane of the phantom. It is given for optimal polarization and for vertical polarization for two different positions of the phantom: standing in front of the base station and laying on a bed at the same height as the base station. The difference between the optimum gain and the vertical polarization gain is given in Figure 6.32 and in Table 6.12.

A single polarization receiver has an excess loss of up to 20 dB. The data also shows that in this case (the male phantom in the transversal plane) a switching polarization receiver has a maximum excess loss of 3.0 dB.
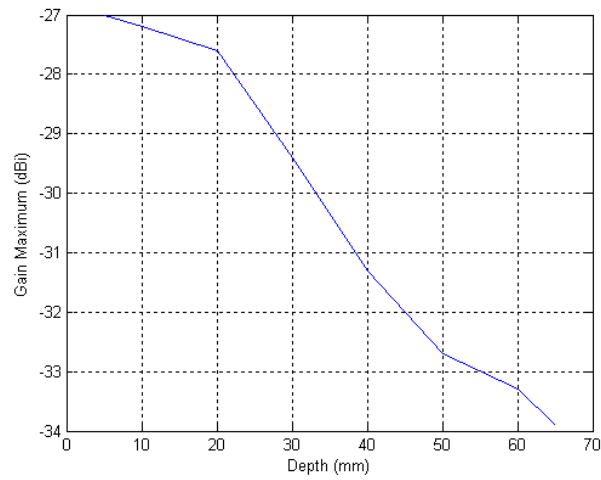
Figure 6.30: The variation of the maximum gain from the implant in the MICS phantom with the depth of the placement.
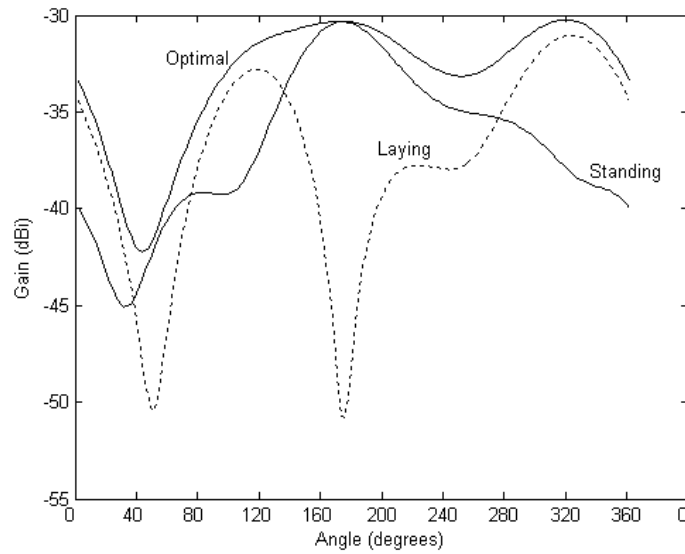
Figure 6.31: The gain from the circumference antenna in the male phantom in the transversal plane. The gain is given for optimum polarization, and vertical polarization for two positions of the man phantom.
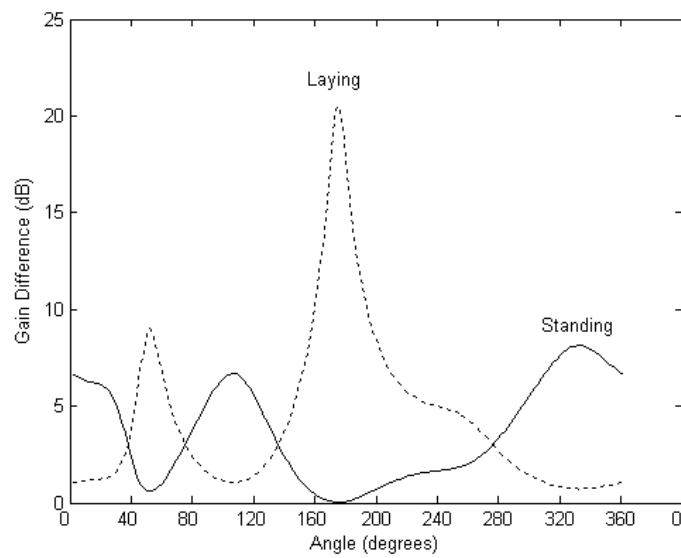
Figure 6.32: The difference in dB between the optimum polarization gain and vertical polarization gain for the male phantom, with the circumference antenna, for two positions in the transversal plane.

6.7 Conclusion

From the simulations in this chapter we conclude that one needs to add margins
to the link budget based on body movement and body size, as given in Table
6.13. The values are taken from Tables 6.3 and 6.8. The values are given
both for the isotropic case, simplified to the three orthogonal planes of sagittal,
frontal and transversal, and for the transversal plane only. The transversal
plane coincides with the horizontal plane with the patient standing up or sitting
down. The variation due to arm movements may affect a specific communication
session with a patient. On the other hand, the variation due to body size will not
affect a specific communication session. However, the latter must be included
in the link budget calculations in order to get a system that works over the
patient population. The most beneficial position of the patient for the link
is with the patient facing the base station. The base station should at least
incorporate polarization diversity. An additional margin of 3 dB has to be added
if only switching diversity is used to accommodate for the polarization loss. The
evaluation of the MICS phantom shows that it probably underestimates the gain
and thus the EIRP from the medical implant.

Case	Arm Movement 5% outage over angles	Body size
Isoptropic	11 dB	3 dB
Transversal	4 dB	3 dB

Table 6.13: Margins to be used in link budget calculations.

## 6.8 Comments on commercial layered numerical phantoms

There are layered phantoms available for FDTD simulations. The results from
this chapter show that care should be taken when using them: since the far-
field properties of an implanted radiator depend on the shape of the phantom,
sub-optimization may be the result if one relies only on one particular human
phantom. The male body from the Visible Human project [67] is the basis for
at least one of these available phantoms, and is a common data set to be used
in publications, c.f. [65]. This may not be the most typical shape of a human
body, and we reccomend that also other body shapes are investigated. The
same applies to the female data set from the same source. (These data sets
are available under a free license, and as such are an economical source of data.
They do not represent any typical or statistical average adult human proportions
but rather specific individuals who made themselves available to science. Thus,
they may be of limited use for development of medical technology.) We have not
had the possibility to use any of these phantoms in the investigations reported
in this thesis, due to constraints in our software. A larger investigation of the

range of body shapes taken from actual human data and the influence of this on radiation from implanted devices will also be necessary in order to give a definite verdict on the MICS phantom.

Chapter 7

Channel Modelling

7.1 Wave propagation

The indoor wave propagation at the MICS band has been studied with both measurements and simulations. The MICS radio channel at 400 MHz is a non-classical case of radio wave propagation in that it differs from the traditional mobile-phone channels. The system is intended for use indoors with both the patient and the base station in the same room. As the wavelength is around 74 cm, a typical room is only a few wavelengths in each dimension. The room characterized below is 3 by 4 by 5 wavelengths. The distance between the patient and the base-station is from a couple of decimeters to the length of the room, i.e., from 0.2 wavelengths up to maybe 10 wavelengths. This kind of link is not well characterized in the literature, since most indoor measurements and simulations are made at mobile phone frequencies and higher, i.e., from 800 MHz and up. Many of the simulations for mobile phone frequencies use ray-tracing algorithms, or hybrids of ray-tracing/FDTD. This is necessary when higher frequencies are investigated and for larger structures than a single room. For instance, at 2.45 GHz the wave propagation within a whole office is impossible to simulate in FDTD, without approximations with contemporary computers. The small dimensions and the long wavelength of our application make ray-tracing unsuitable. On the other hand, the combination of a low frequency and the limited range makes full FDTD simulations both possible and practical for the MICS band investigations. Few such full FDTD simulations of complete, furnished, interiors have been reported in the literature up to now.

7.1.1 Measurements in the MICS band

The measurements were made in order to characterize the radio channel for the MICS band. Since the band is narrow, 402 MHz - 405 MHz, or 0.7 % relative bandwidth, it was only measured at the mid-band frequency of 403.5 MHz. A room in the basement of the department of Electroscience, Lund University, was taken as a suitable model of a consultation room at a hospital. The room has

the dimensions of 225 cm by 343 cm, with a ceiling height of 302 cm. A CAD model of the room is shown in Figure 7.1. Two walls have doors in them, and are made of plaster. The other two walls are thicker and made of reinforced concrete. The floor and the ceiling are also made of concrete. One wall has a small window. The room is fitted with a metal radiator, a metal ventilation duct at the ceiling and a metal fire escape ladder leading up to the small window. The channel in the room was measured both without any furniture and furnished with a wooden bed, a wooden chair and a wooden table with metal frame and legs.

The channel was measured with two dipole antennas on plastic stands. The dipole antennas were made for the centre frequency of 403.5 MHz and fitted with bazooka baluns [28]. The stationary dipole was fed from a HP 8642B signal generator with a 1 dBm continuos wave (CW) signal. The power received by the movable dipole was measured with an Advantest R3131 spectrum analyzer in the zero span mode. Measurements were taken as averages of 20 measurements in time, the averaging being done by the spectrum analyzer. Only the power of the received signal was recorded.

The time delay properties of the channel were not measured. This was because the maximum usable bandwidth in the MICS system is 300 kHz. This corresponds to a maximum symbol time of 3.33 ms. During one symbol time the signal would propagate 999.3 m. This is much larger than the dimensions of the room we investigated. For a signal to propagate this distance it have to be reflected at least 291 times against the surfaces of the room. A signal reflected this many times would not have enough power to interfere with the detection of the symbol in the receiver. A practical modulation scheme will probably use a symbol time that is longer than 3.33 ms in order to keep the modulated signal within the allocated bandwidth, thus decreasing the risk of inter-symbol interference further.

7.1.2   Paths

Three main paths were measured in the room. These are shown as A, B and C in Figure 7.2. One additional path extending into a corridor, path D, was measured in order to investigate the behavior when line of sight conditions were not present. The channels along the paths were sampled every 25 mm by moving the antenna and measuring the received power in every point. The spectrum analyzer took a mean value of 20 consecutive measurements in time. This was done in order to reduce the influence of stochastic measurement noise on the results.

An area, E, above the bed was also measured by sampling in both the x- and the y-direction in order to evaluate the 2D field variations. This measurement also served as a further validation of the simulation results presented before. The area is marked E in Figure 7.2 and consists of 777 measurement points.
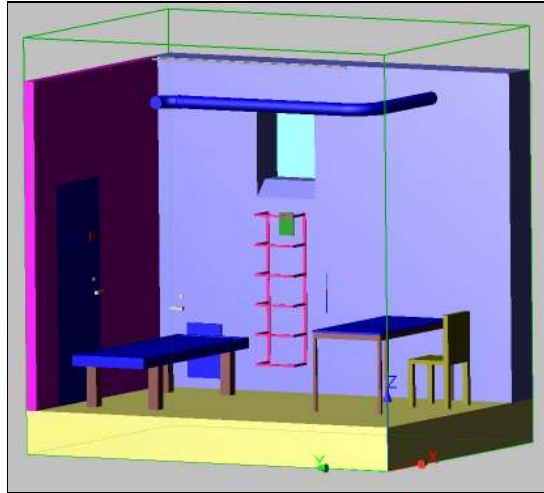
Figure 7.1: CAD model of the furnished room. Two walls and the ceiling are removed for clarity, the longer wall has the door to the corridor.

7.1.3 Test of stationarity

To test if the channel characteristics were stationary in time, path A was measured three times after each other during one day (measurements made morning, afternoon and night). Each curve consists of 77 measurement points. The points are connected by means of linear interpolation. The result is shown in Figure 7.3 and it leads to the conclusion that the channel is stationary in the long term. The mean over distance of the standard deviation between the curves was 0.31 dB. The maximum standard deviation at one point was 1.37 dB.

7.2 Measurement results

The channel was measured both with and without furniture. The transmitting antenna was placed both in vertical and horizontal polarization. The receiving antenna was moved to all three polarizations: co-polarization, cross-polarization and cross-90-polarization. Co-polarization here follows the standard definition, where the receiving antenna has the same orientation as the transmitting antenna. Cross-polarization also follows the standard definition, with the receiving antenna rotated 90 degrees around the axis going through the feed-point of both antennas. In cross-90 polarization the receiving antenna was perpendicular to both co- and cross-polarization, which places the arms of the movable dipole parallel to the floor and parallel to the measurement path A. In the far-field in free space this polarization is not present, but it was recorded since we were measuring in the near-field in a scattering environment. As will be shown below, the path loss for the cross-polarizations is higher than for the co-polarization.
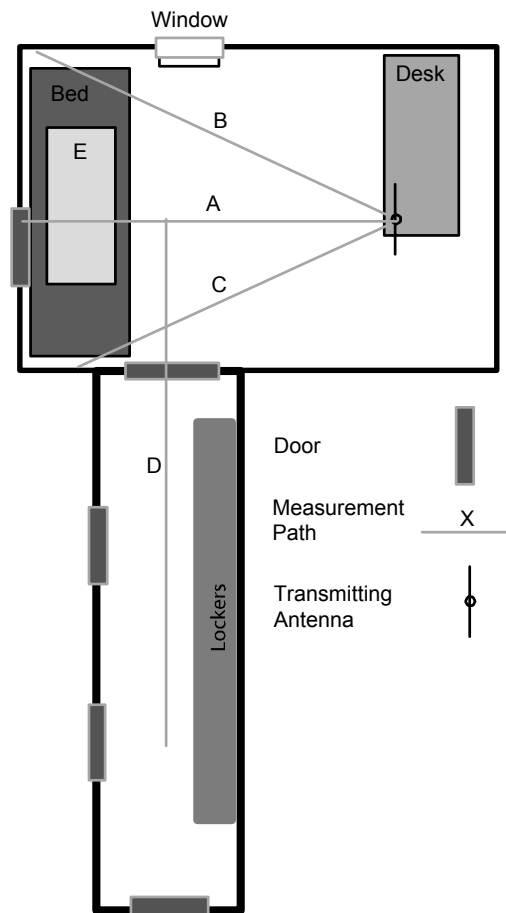
Figure 7.2: Drawing of the studied room with measurement paths A, B, C and D marked. The area E over the bed is also marked.
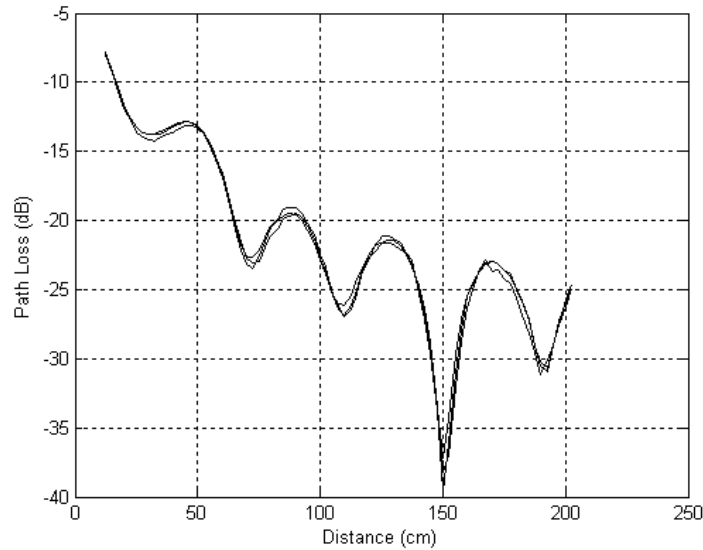
Figure 7.3: The received power measured along path A at three different times.

A spatial varying pattern is also clearly visible.

7.2.1 Empty Room

In order to evaluate if the backscattering from the antenna adds to the interference pattern in the room, we repeated the measurements with vertical transmitter polarization with an electrically small dipole as the receiving antenna. The result is shown in Figure 7.4. The curve from the small dipole has been adjusted in order to fit the other curve at the right side of the plot. The flat bottom of the dips measured with the small antenna is due to that the noise floor of the spectrum analyzer was reached. The spatially varying pattern is the same as in the case with the resonant dipole, which gave the conclusion that the backscattering from the antenna does not affect the measured channel characteristics to a significant degree.

Path A was measured both with vertical and horizontal transmitting antenna polarization. For each polarization 3 measurements were done: Co-polarized, cross-polarized and cross-90 polarized. The results are shown in Figures 7.5 and 7.6. Measurements were also done along the two diagonal paths B and C. These results are shown in Figure 7.7. Qualitatively they all have the same decrease and variations with distance.

Figure 7.4: Comparison of measurements along path A with small dipole (dotted curve) and standard half wavelength dipole antenna.
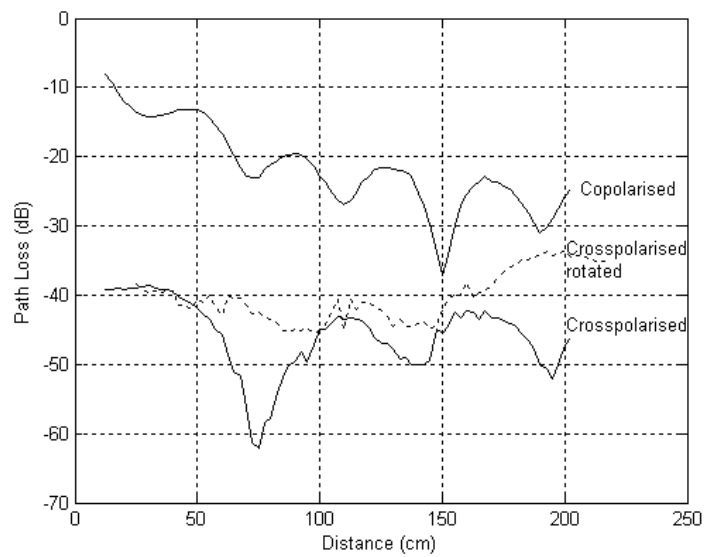
Figure 7.5: Measurement in an empty room with vertical polarization of the transmitting antenna.
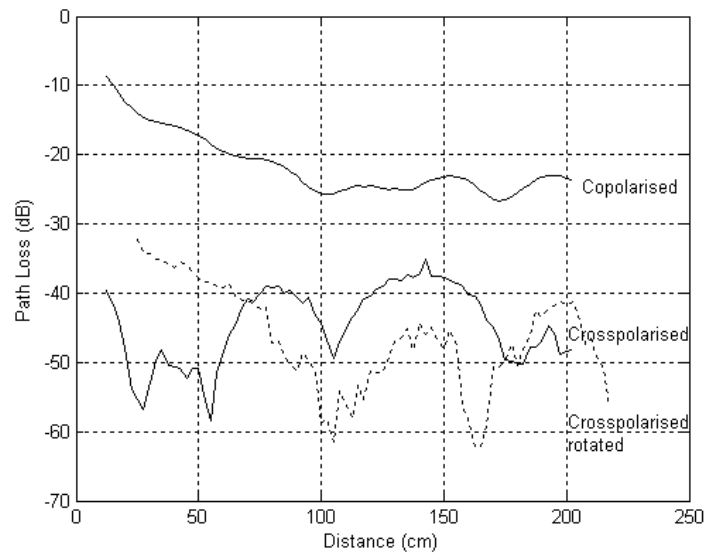
Figure 7.6: Measurements in an empty room with horisontal polarization of the transmitting antenna.
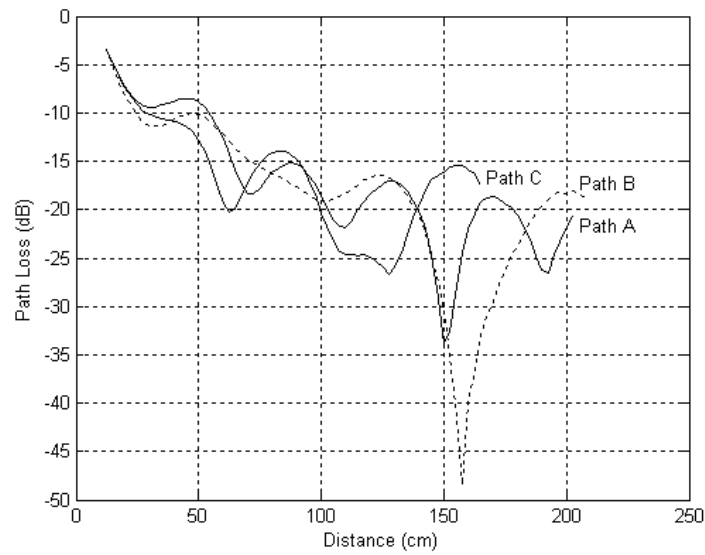
Figure 7.7: Measurement of path loss along paths A, B and C.
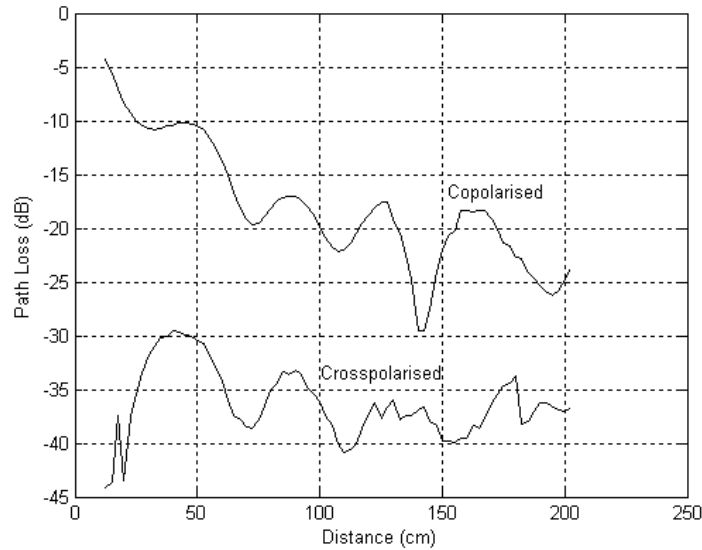
Figure 7.8: Measurements with vertical transmitter polarization in furnished room.

7.2.2   Furnished Room

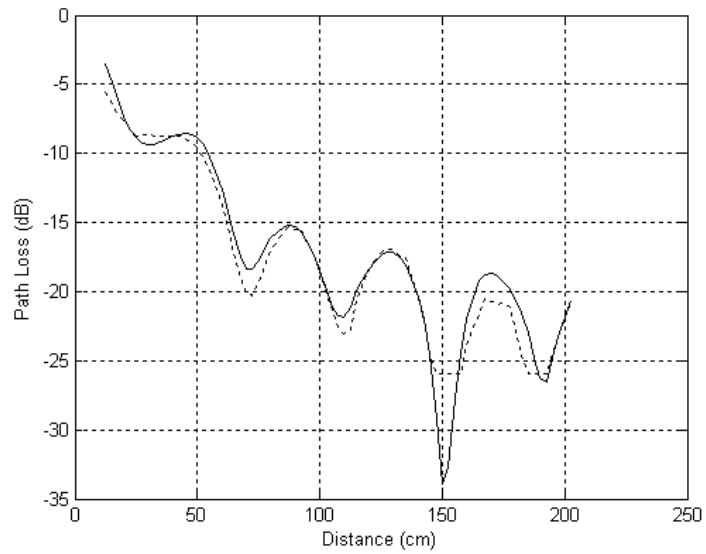The room was furnished with a wooden bed and a table, which consisted of a wooden top and with a metal frame around the edges of the top and metal legs. A wooden chair was also placed by the table. The placement of the furniture is shown in Figure 7.1. Measurements with vertical transmitting polarization were repeated in the furnished room. The results are depicted in Figure 7.8. Measurements were only taken for the co- and cross-polarizations. The exact shape of the spatially varying pattern is similar to that of the unfurnished room, but the overall level of the field is lower. This is shown in Figure 7.9, where we plot the vertically co-polarized measurements from the furnished and unfurnished room in the same plot. Here we can see that the levels are a bit lower in the furnished case, which can be attributed to the altered standing wave pattern in the room, and to absorption in the furniture.

The channels for co-polarization of the two diagonal paths were also measured. The result is shown in Figure 7.10 together with the result of path A for comparison. The curve that differs a lot at the furthest point from the transmitting antenna is the path that comes close to the metal fire escape ladder. This metal structure is probably the cause of this. The diagonal paths are shorter in this measurement as the bed interfered with the antenna stands and made the extension along the complete paths not possible.

A measurement with a slanted polarization was also performed. The trans-
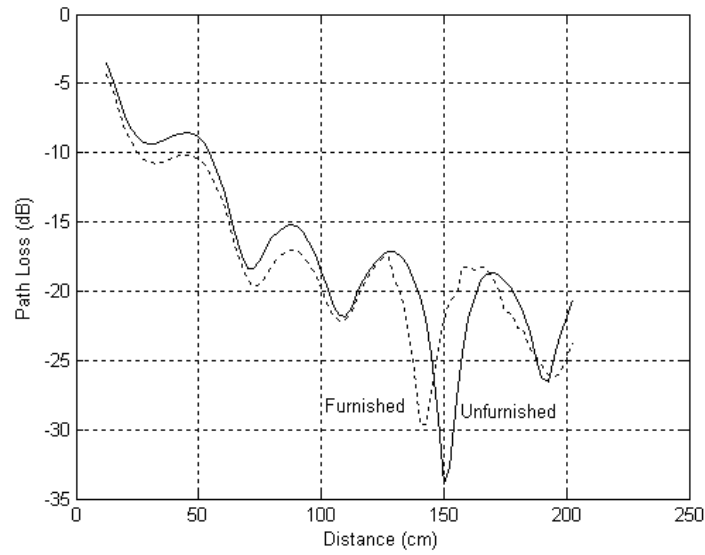
Figure 7.9: Comparison between furnished and unfurnished room.
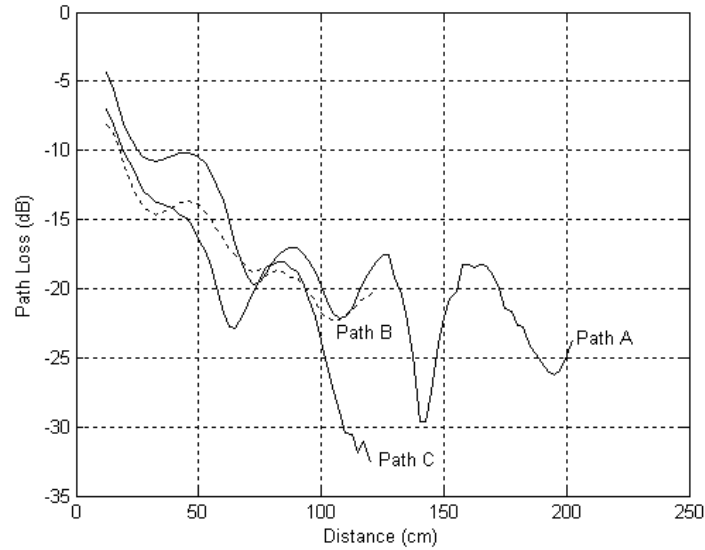
Figure 7.10: Measurements along path A, B and C in the furnished room.
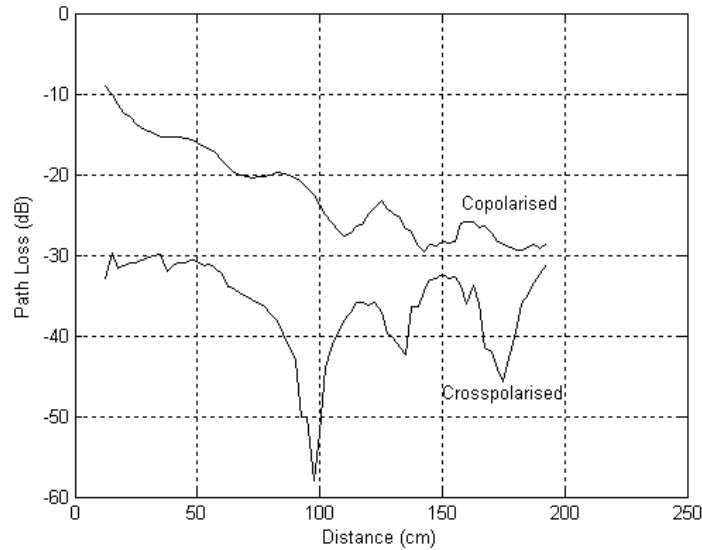
Figure 7.11: Measurement in the furnished room with transmitting antenna at 45 degrees to all planes.

mitting antenna was angled at 45 degrees to the path in the vertical and horizontal planes. The moveable receiving antenna was placed in both co- and cross-polarization. The results are shown in Figure 7.11. From the concept of superposition the result should be similar to that measured in the orthogonal polarization cases, this is also the case. The measurements show that co-polarization is necessary in order to minimize the path loss.

The final measurements were done over the area E which is a part of the area of the bed in the furnished room. The measurements were taken 66 cm above the floor, corresponding to a patient laying down on the bed. Figures 7.12 and 7.13 show the measured path loss across this area. The measured area corresponds to orthogonal distances of 137.5 cm to 190 cm from the antenna. The other axis is graded after the distance from the wall to the corridor. The difference between the measurements and the theoretical free space loss at the corresponding distances were calculated. The excess loss that needs to be added to the free space loss in order to cover a given percentage of the total area was calculated, and the result is presented in Figure 7.14. Table 7.1 summarizes this data for some given access levels, and gives the absolute levels corresponding to these.

Coverage	Absolute Level of path loss	Excess loss relative Free Space
90%	34 dB	-5 dB
95%	37 dB	-8 dB
97%	41 dB	-11 dB
99%	48 dB	-18 dB

Table 7.1: The maximum path loss over a given percentage of the area E.
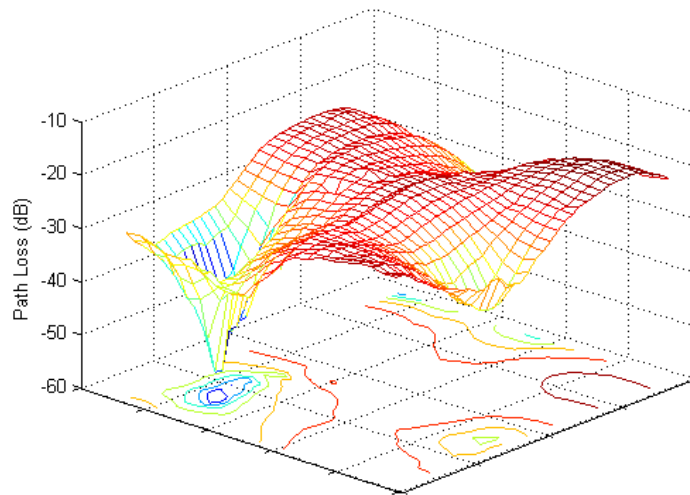
Figure 7.12: The path loss at different positions over the area E over the bed.
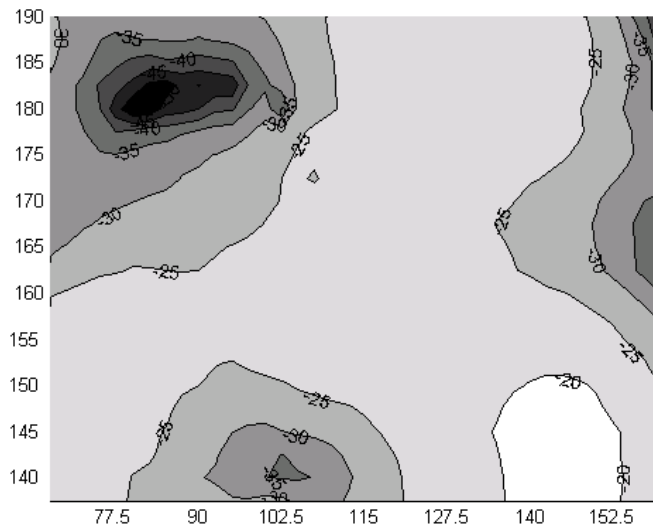
Figure 7.13: The path loss at different positions over the bed.
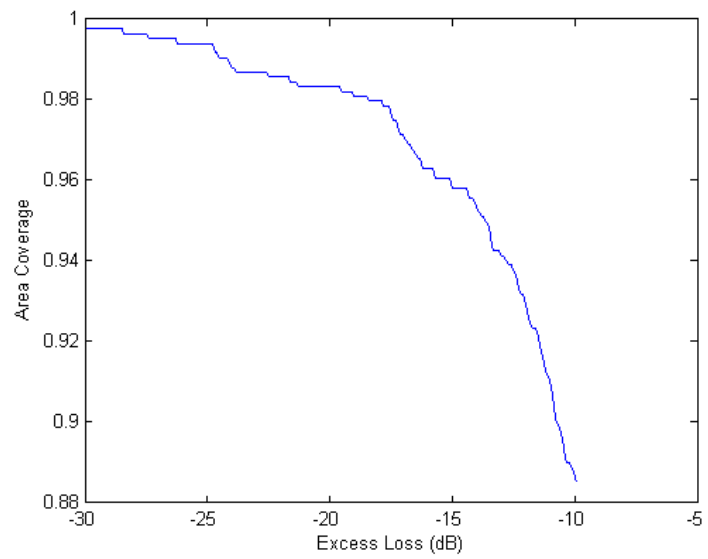
Figure 7.14: The excess loss over the free space loss, necessary to cover a given percentage of area E.

Material	Permittivity	Conductivity
Concrete	6.0	$1 \cdot 10^{-2}$
Gypsum	4.0	$1 \cdot 10^{-2}$
Wood	23.	$1 \cdot 10^{-11}$
Glass	5.5	$1 \cdot 10^{-12}$

Table 7.2: The dielectric parameters of the building materials used in the simulations.

Piece	Material
Wall a	Concrete
Wall b	Concrete
Wall c	Gypsum
Wall d	Gypsum
Floor	Concrete
Ceiling	Concrete
Heater	PEC
Ventilation Duct	PEC
Fire Escape Ladder	PEC
Window	Glass
Chair	Wood
Bed	Wood
Table Surface	Wood
Table Frame	PEC
Doors	Wood
Door Handles	PEC

Table 7.3: The materials used for the various parts of the room in the simulations.

7.3 Simulations

The room was modelled in the FDTD simulation tool SEMCAD, which is described in Appendix D. A detailed model was done in the program. It is shown in Figure 7.1. The model was sub-divided with a non-uniform grid with a maximum grid size of 25mm. The resulting mesh had up to 12 million voxels. Five different materials were used in the simulations: concrete, plaster, wood, glass and metal. They were all simulated as dielectrics, as in Table 7.2, except metal which was modelled as a perfect electric conductor, or PEC. The composition of the different objects in the room is given in Table 7.3.

The FDTD simulations give as result the RMS E-field in the room. From this the equivalent received power by a dipole antenna is calculated as

$$P_{rec} = \left(\frac{E^2}{Z_{air}} \cdot k_{dipole} \cdot \lambda^2 \right) \tag{7.1}$$

where k_{dipole} is 0.13 for a dipole antenna [28]. Here $Z_{air} = 377 \ \Omega$ is the im-
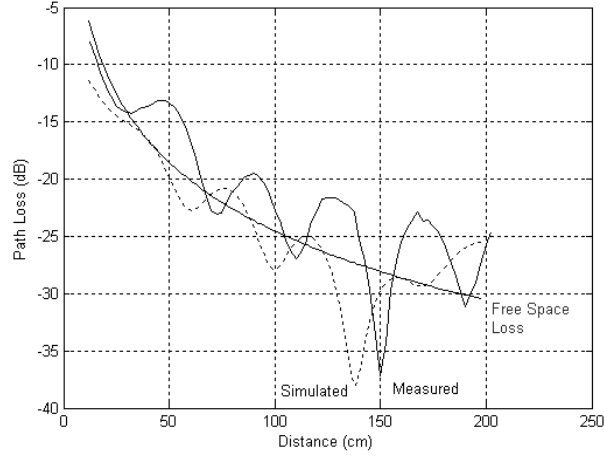
Figure 7.15: Comparison of measured and simulated path loss and theoretical free space loss along path A.

pedance of the air and $\lambda = 0.74$ m is the wavelength in air. From the value of the received power the path loss was calculated by subtracting two times the ideal dipole gain of 2.15 dBi and normalization of the transmitted power. In Figure 7.15 the simulated and measured values along path A are both plotted. In addition the ideal free space loss of

$$PL_{freespace} = \left(\frac{\lambda}{4\pi d}\right)^2 \tag{7.2}$$

is also plotted. Here d is the distance from the source.

The simulated and measured values agree well in their general trend. They also agree with the idealized model of free space loss. Closest to the source they differ from each other. This is partly due to that the measured data includes effects of coupling between the two antennas. In the simulated case there is no coupling, since we only simulate one antenna and calculate the idealized response of the other. The effects from the reactive near-field of the simulated antenna influence the calculated value. In addition, the simulated values make the assumption that the E-field is constant along the antenna, which it is not. The E-field in the room varies in all three dimensions. The ideal free space curve does not include effects from any antenna.

Further down along the path, the measured and the simulated antenna differ in the placement of the dips. This may be attributed to a number of error sources. The values of conductivity used in the simulation affect the phase of the reflection of the wave against the wall. If we change the conductivity of the walls, the spatially varying pattern will shift. This is shown in Figure 7.16
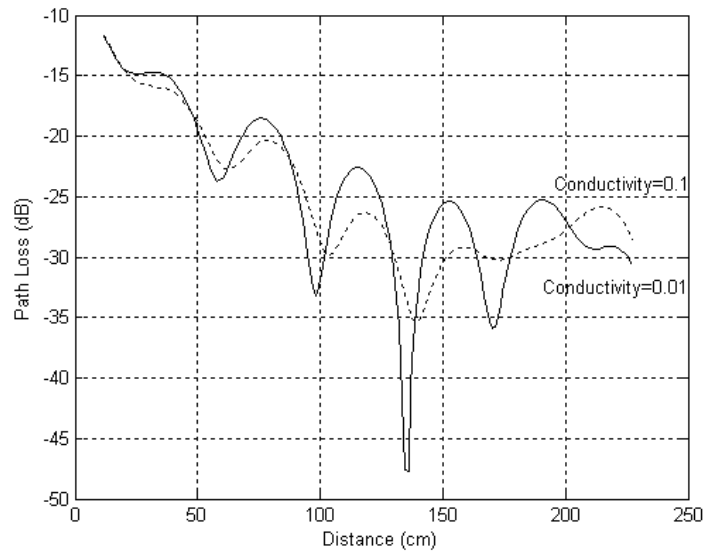
Figure 7.16: Path loss along path A with different conductivity in the surfaces of the room.

where the conductivity of all the surfaces of the room was increased by 10 times in the simulation. The spatially varying pattern then shifted 5cm.

Another source of error is the makeup of the concrete walls. A reinforced concrete wall consists of concrete and iron reinforcement bars. The iron bars are typically placed in a crisscross pattern at a depth of about 3 cm from the surface. A simulation was done where all the conductivity of the concrete surfaces was moved from the material itself to a perfectly conducting plate placed 3 cm from the surface. The resulting spatially varying pattern is shown in Figure 7.17. The position of the dips now moved 16 cm towards the transmitting antenna. This shows that a very detailed modelling of the room is necessary in order to simulate the spatially varying pattern with a very high degree of accuracy. The next simulation shows that this may not be necessary in order to design the system. The same room and antenna configuration was simulated at 402MHz and 405 MHz. The difference between the placement of the maximum dip is about 4 cm, as can be seen in Figure 7.18. To change a channel within the MICS allocation will thus be of limited use in order to reduce the effects of the standing wave pattern.

The same simulations have been made with the room furnished. As in the case with the measurements, no large qualitative difference in the wave propagation was seen. It is important to remember that the overall spatially varying pattern is not regular and symmetric, and the distance between the dips along an arbitrary path in the room is not necessarily half a wavelength. A plane
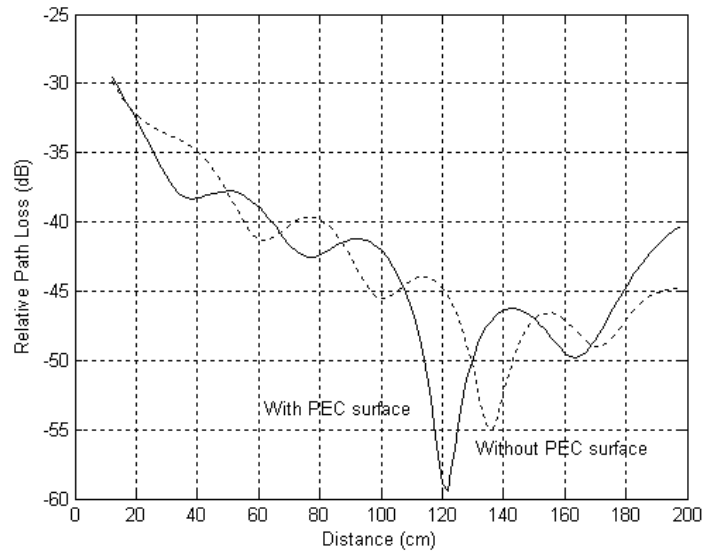
Figure 7.17: Path loss along path A with and without PEC surfaces in the concrete walls.
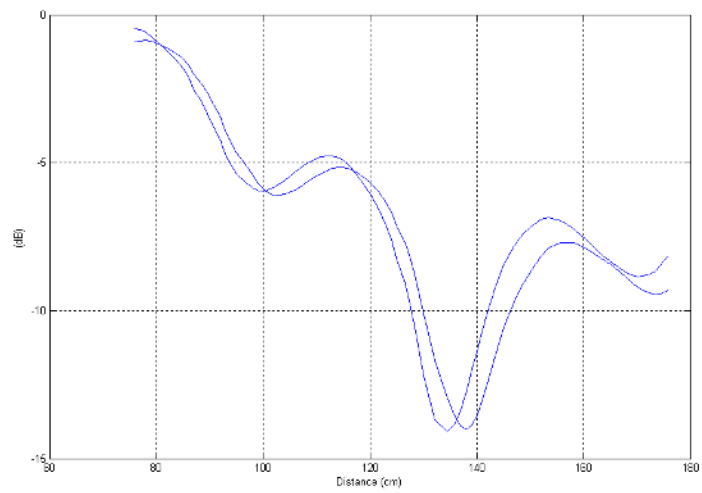
Figure 7.18: The difference betwen the standing wave pattern at 403 MHz and 405 MHz, taken along path A.

through the room at the height of the feed point of the dipole is illustrated in Figure 7.19. The frequency is 403.5MHz. The complex pattern is clearly visible.

The difference in the measurements between the horizontal and vertical co-polarized cases may be investigated by comparing the plots of the corresponding E-fields in a horizontal cut through the antenna feed. These are given in Figures 7.19 and 7.20. In both figures the the grayscale is 5 dB per graduation. There is a marked difference in the qualitative behavior of the standing wave pattern between the two polarizations. This is due to that the plane in the horizontal case is parallel to the dipole antenna, and in the vertical case perpendicular to it. Figure 7.21 shows the standing wave pattern in the plane parallel to the vertical dipole antenna. This plot also shows the wave propagation in the concrete walls, floor and ceiling.

The Figures 7.22 to 7.28 have been generated by drawing a shell at the iso-surfaces corresponding to the path losses given in each figure. From these it is obvious that the standing wave pattern in a small room is very complicated at the MICS band. In order to cover the whole 3D space of the room high path losses must be accepted. Figure 7.29 shows the iso-surfaces for a path loss of 30 dB, viewed from above. If only the free space loss formula was used, this surface should cover the complete path A. From the picture it is evident that the path loss is larger if full area coverage is to be assumed.
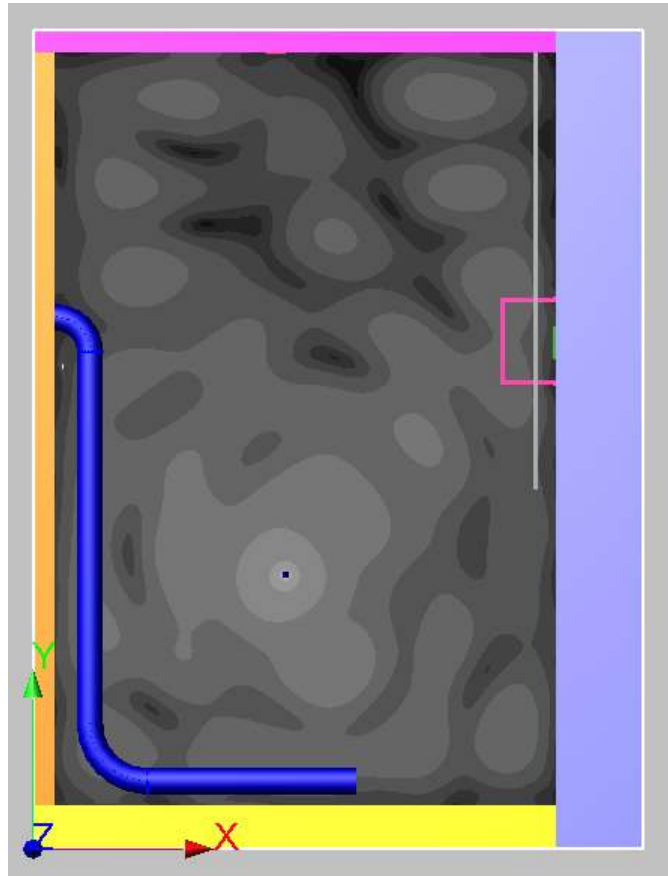
Figure 7.19: Standing wave pattern in the room with a vertical antenna. The field is plotted at the height of the feed of the antenna. Every graduation in the grayscale represents 5 dB of pathloss.
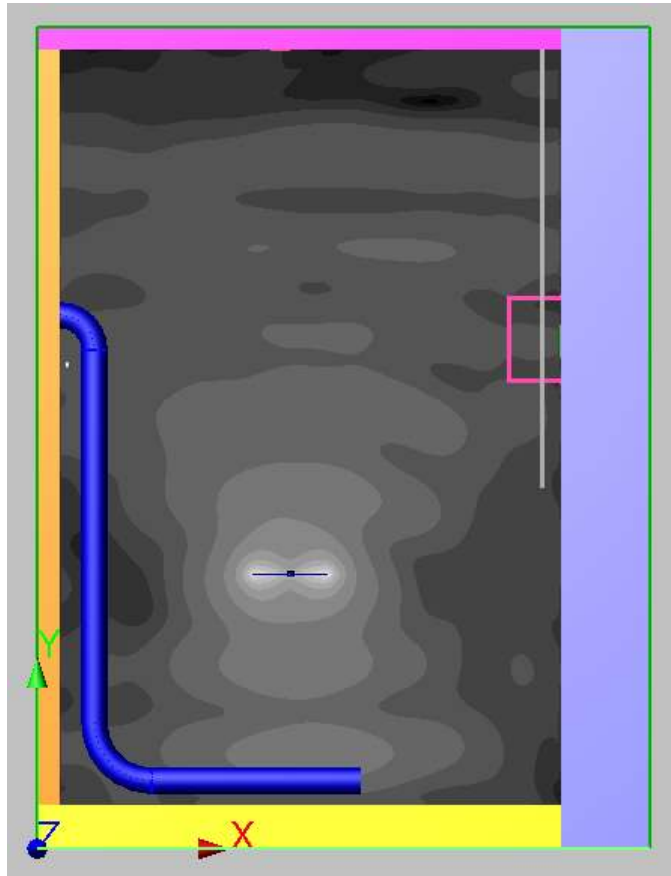
Figure 7.20: Standing wave pattern in the room with a horizontal antenna. The field is plotted at the height of the feed of the antenna feed. Every graduation in the grayscale represents 5 dB of pathloss.
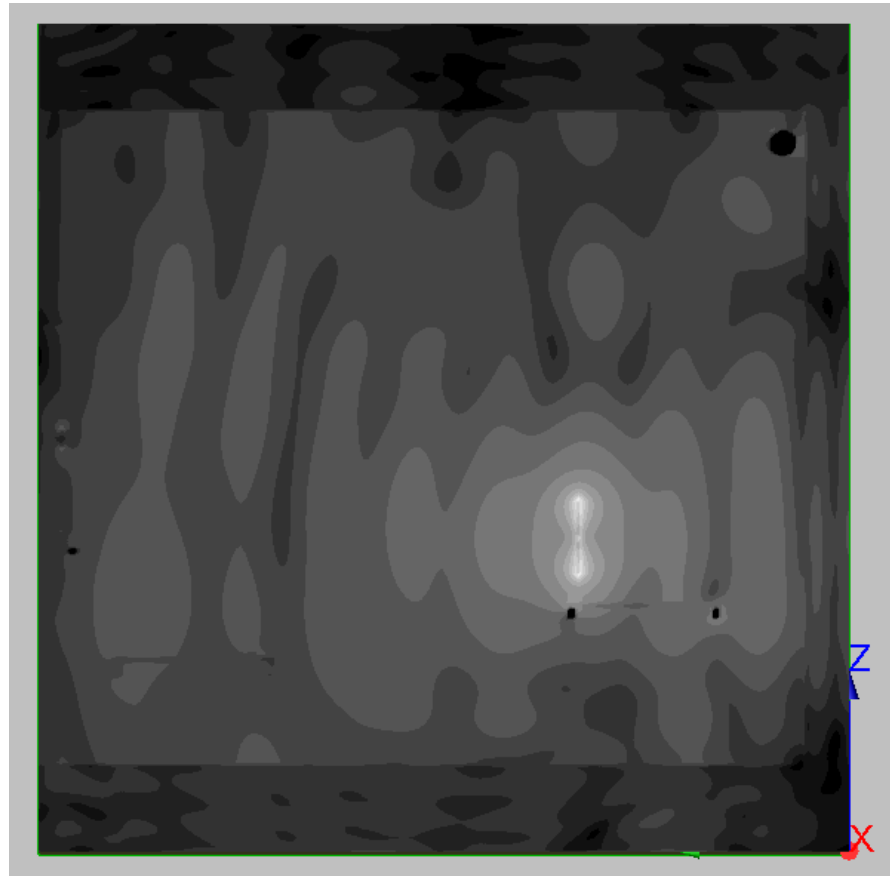
Figure 7.21: Standing wave pattern in the room with a vertical antenna. The field is plotted at a plane through the antenna along parallel to path A. Every graduation in the grayscale represents 5 dB of pathloss.
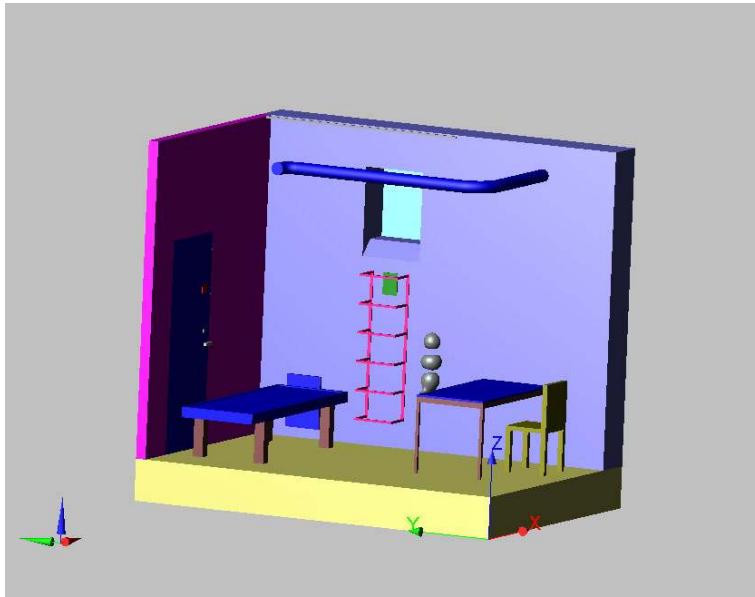
Figure 7.22: Path loss < 10dB
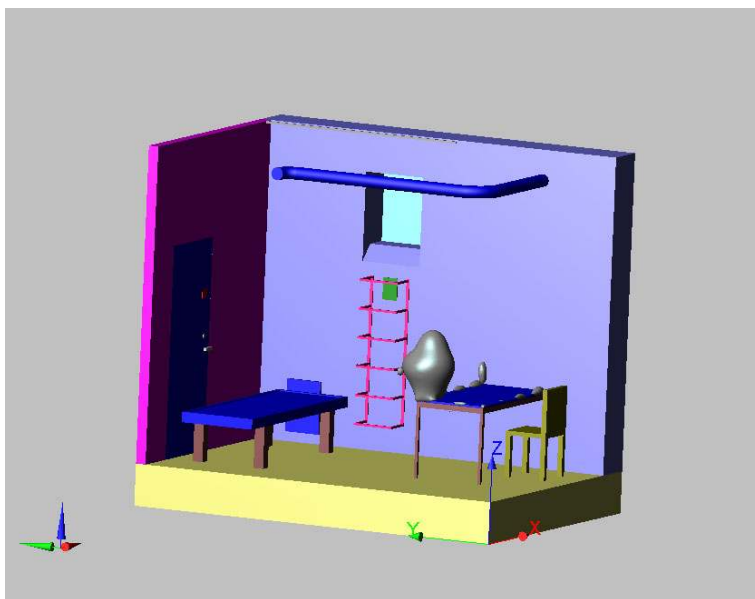
Figure 7.23: Path loss < 15 dB
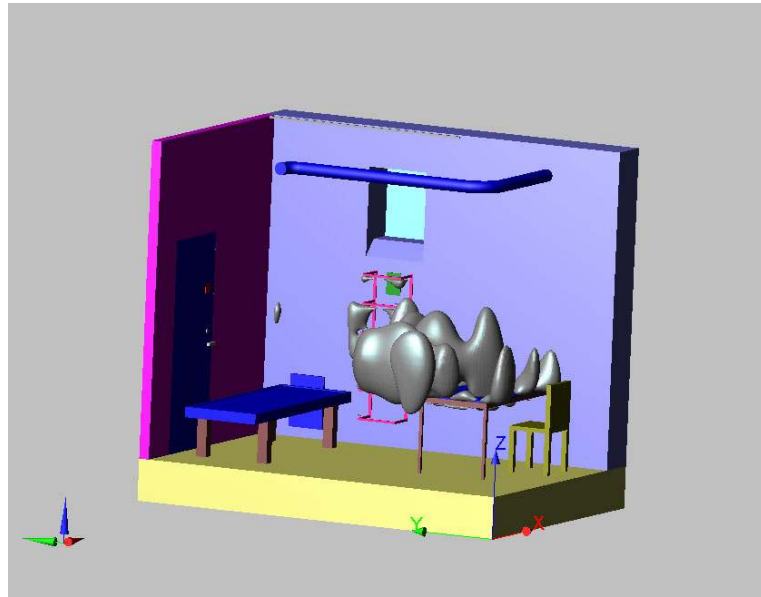
Figure 7.24: Path loss < 20 dB
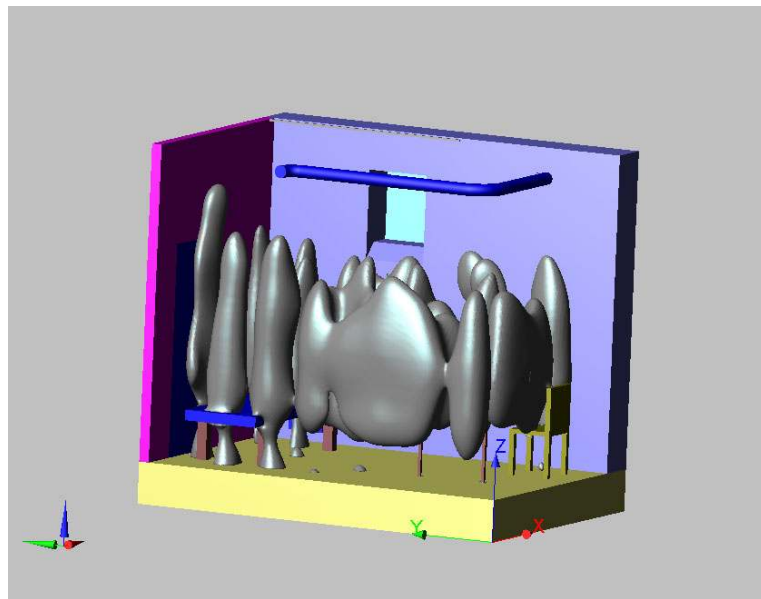
Figure 7.25: Path loss < 25 dB
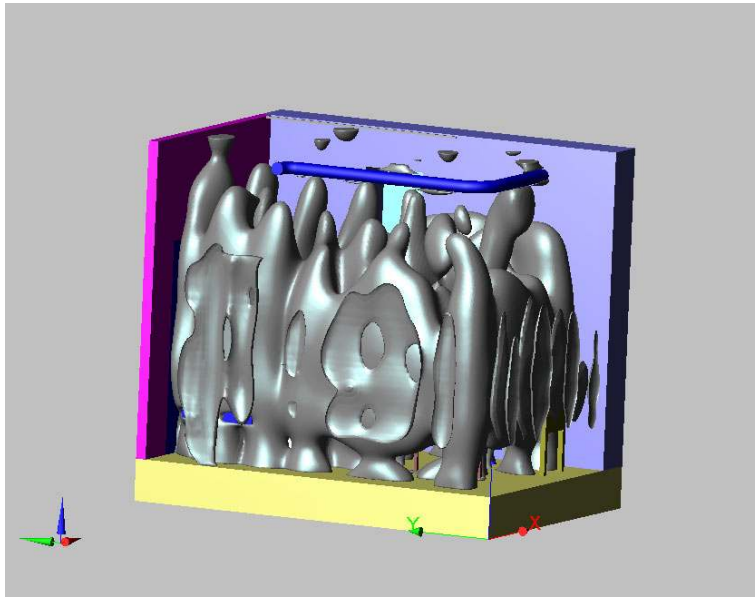
Figure 7.26: Path loss < 30 dB
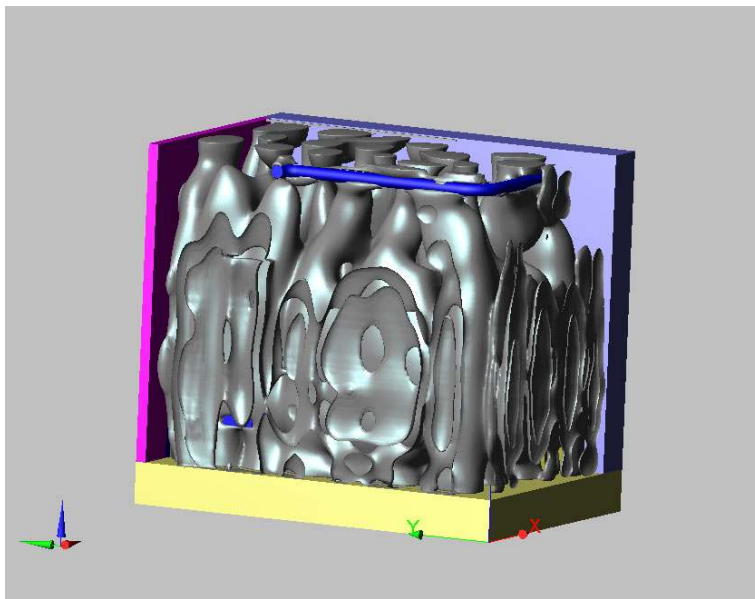
Figure 7.27: Path loss < 35 dB
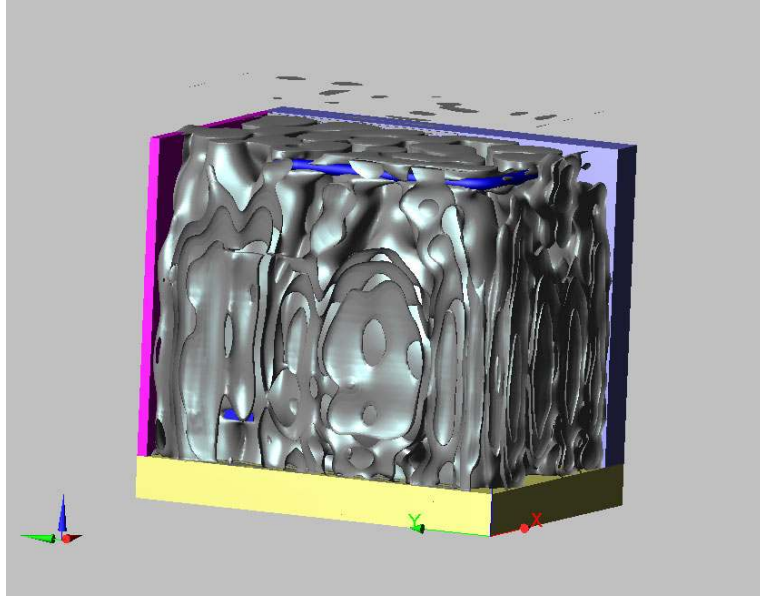
Figure 7.28: Path loss < 40 dB
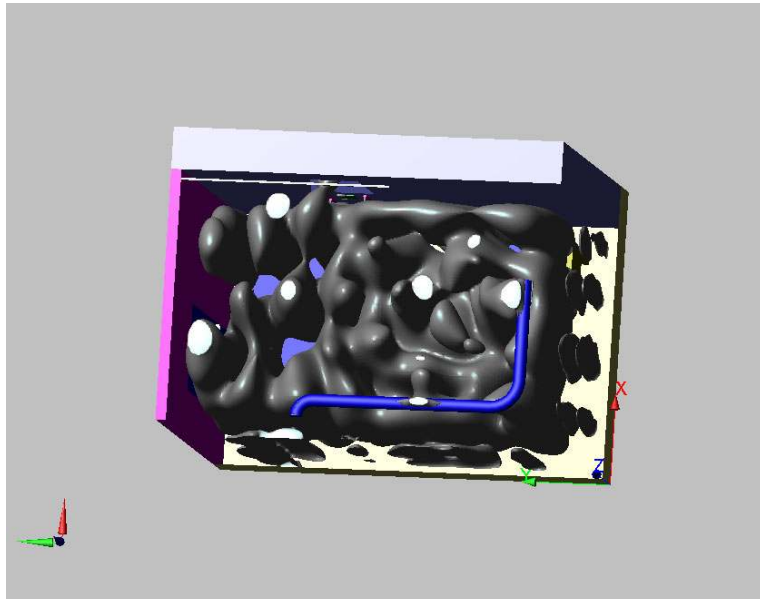
Figure 7.29: Path loss < 30 dB viewed from above.

Chapter 8

Link Budget II

We now return to the application and use the results from the previous chapters to estimate the performance of the link to the medical implant in some idealized cases. We will also tentatively incorporate our results in the link budget discussed in chapter 3.

The measurements of the standing wave pattern in the room in Chapter 7 were made with a dipole antenna at the patients position. If we would place an actual patient in the room, the pattern will look different as the patients body will influence the wave propagation. Thus, we can not simply add the results from the antenna pattern calculations, which implies that we receive the power as a plane wave from one single direction, to the variation in the room, which is calculated with signals arriving from all directions. One possibility is to make the measurements with an antenna inside a phantom that is placed in the room. This complicates the procedure, as not only the spatial position of the phantom will influence the result, but also the rotation of the phantom, i.e., if it is upright or on its side. Furthermore, the position of the antenna inside the phantom, and the type of antenna used, influence the result. This implies that a large number of measurements have to be made in order to be able to draw any general conclusions

The reliable results from the comparisons of the simulations and the measurements of the room indicate that a larger study of the impact of the patients body in the room can be made by simulations. A simulation study would make it practical to test different implanted antennas, body sizes, body postures and body positions. The problem is that our simulations with the furnished room are at the limit of what is reasonable in memory and time with our current computer setup (the simulations were done on a 2.8 GHz Pentium4 computer with 2 GB of RAM). The problem with including the body, or phantom, in the simulations is that the shorter wavelength inside the body requires a finer mesh in the simulation. That increases the memory requirements to exceed our present limit.

We can still use the results presented in the previous chapters to make calculations on a number of simplified cases. We then look at the impact of each

factor in isolation, such as the gain variation with rotation of the body and the wave propagation in the room. We can also make a calculation where we include all of the effects, but this does not represent any real case, as the introduction of the patient in the room will change the standing wave pattern, and the patient will receive power from many different directions due to reflections. However, such an investigation will give us an idea of how the system could behave and help us to identify the most critical parts in the system design.

8.1   Background noise level

The theoretical background noise in the MICS band is the thermal noise. If we assume that the devices are used indoors at a room temperature of 20° Celsius, we get an ambient noise density of

$$kT = 1.38 \cdot 10^{-23} \cdot 293 \text{ Ws} \simeq 4.0 \cdot 10^{-21} \text{Ws} = -203.9 \text{ dBW/Hz} \qquad (8.1)$$

For the implant the background noise temperature is the body temperature, or typically 37°Celsius. The thermal noise becomes

$$kT \simeq -203.7 \text{ dBW/Hz} = -173.7 \text{ dBm/Hz} \qquad (8.2)$$

Both of these levels are essentially the same, and -174 dBm/Hz will be used for the thermal noise hereafter. In the implant receiver the thermal noise dominates, since external noise sources are attenuated due to the reflection from the air to skin interface, as has been shown. The total noise into the implant receiver over a bandwidth of 250 kHz is

$$\begin{aligned} \text{N}_{input} &= -174 \text{ dBm/Hz} + 10\log(250 \text{ kHz}) \\ &= -174 \text{ dBm/Hz} + 54 \text{ dBHz} = -120 \text{ dBm} \end{aligned} \qquad (8.3)$$

The base station receiver gets additional noise from other sources, both natural and man-made. In the ITU-R document [15] the total noise was estimated to 20 dB above the noise floor. This results in a noise at the input of the base station of

$$\text{N}_{input} = -174 \text{ dBm/Hz} + 54 \text{ dBHz} + 20 \text{ dB} = -100 \text{ dBm} \qquad (8.4)$$

We have measured the noise level in one of the laboratories at the department. Measurements were made with a dipole antenna connected to a preamplifier and a spectrum analyzer. The spectrum analyzer was a Rhode & Schwarz Spectrum Analyzer with a MITEC preamplifier. The result from the measurement was a noise level with a mean of -158 dBm/Hz. This would give a total level of received noise at the input of -104 dBm in a bandwidth of 250 kHz. The ITU-R document estimates the noise to be 20 dB over the thermal noise level, which gives a noise level of -100 dBm at the input. The ITU-R estimated noise

	Downlink		
BW	25 kHz	250 kHz	300 kHz
$N_{antenna}$	-130 dBm	-120 dBm	-119dBm
NF	9 dB	9 dB	9 dB
N_{input}	-121 dBm	-111 dBm	-110 dBm
	Uplink		
BW	25 kHz	250 kHz	300 kHz
$N_{antenna}$	-110 dBm	-100 dBm	-99 dBm
NF	4 dB	4 dB	4 dB
N_{input}	-106 dBm	-96 dBm	-95 dBm

Table 8.1: Noise Levels at the input of the receiver.

level is thus higher than what was measured in the lab. The higher level will be used in the calculations, since a hospital will probably be noisier than the RF-laboratory at the department. The latter is designed to be quiet, in contrast to the hospital which is equipped with an assortment of high power RF machinery, such as X-ray machines, RF ablation equipment etc. Some initial measurements made at Lund University Hospital also point to that a number of narrow band interferers should be expected. The noise figures of 9 dB for the implant and 4 dB for the base station from the ITU-R initial link budget calculation will be used here. This gives the effective noise levels in up- and downlink presented in Table 8.1.

8.2 Base station output power

The maximum permitted EIRP from the base station is -16 dBm in the MICS standard. If a dipole antenna with a gain of 2 dBi is used as the base station antenna, the maximum power into the antenna is -18 dBm.

$$P_{basestation} = -18 \text{ dBm} \tag{8.5}$$
$$G_{base} = 2 \text{ dBi} \tag{8.6}$$

8.3 Implant output power

The transmitting system consisting of the implant, the antenna and the body has a limited EIRP of

$$EIRP = -16 \text{ dBm} \tag{8.7}$$

This is set not to cause interference, and is a maximum level. The power into the antenna used in the ITU-R calculations is -2 dBm. This gives an EIRP for the man phantom, cf. Table 6.7

$$P_{acc} + G_{antenna} = -2 \text{ dBm} - 26 \text{ dBi} = -28 \text{ dBi} \tag{8.8}$$

S/N	ITU-R	$C_{\max}$	With maximum EIRP	$C_{\max}$
Uplink	14 dB	1.4 Mbit/s	31 dB	3.1 Mbit/s
Downlink	15 dB	1.5 Mbit/s	19 dB	1.9 Mbit/s

Table 8.2: S/N ratios from ITU-R link budget as described in Chapter 3.

The simulations in Chapter 5 show that the boy phantom has the highest maximum gain, with a maximum gain that was 3 dB higher than the man phantom. Using this, the maximum allowed power into the antenna is calculated as

$$-16 \text{ dBm} + 26 \text{ dB} - 3 \text{ dB} = 7 \text{ dBm} \tag{8.9}$$

This is a high value for a medical implant with an internal battery. With a power amplifier efficiency of 50% and a battery voltage of 2.8 V it would equal a current drain of 3.6 mA. A typical pacemaker battery today is of lithium-iodine technology and has a voltage of 2.8 V, when delivering a current drain of 20 μA [4]. The capacity is typically around 2 Ah, which gives the pacemaker a lifetime of 10 years. Each second of communication at a power level of 7 dBm would equal running the pacemaker in normal operation for 3 minutes. To reduce the lifetime of the pacemaker with one year the transmitter has to be run for 56 hours. These calculations exclude the power needed for other parts of the transmitter, such as modulation and coding. One problem is that the large internal resistance in the lithium-iodine batteries makes them unsuitable for current drains larger than 20-30 μA [4]. There are other technologies which give the same capacity and that allow for higher currents, for example Lithium-polyflourcarbon, which has been proposed for use in pacemakers and allows a current drain of up to 10 mA [68].

8.4   Bit-rate

The maximum bit-rate in a given channel depends on the minimum signal to noise ratio, S/N. It can be shown [69] that the maximum channel capacity $C_{\max}$ for the bandlimited additive white gaussian noise channel is

$$C_{\max} = BW \log_2 \left(1 + \frac{S}{N}\right) \tag{8.10}$$

where S is the mean power, N is the mean noise, BW is the bandwidth of the channel in Hz and $C_{\max}$ is the maximum capcacity in bits/Hz. We set the bandwidth to the maximum allowed in the MICS standard, $BW = 300$ kHz. The theoretical maximum bitrates corresponding to the ITU-R calculations are given in Table 8.2. Thus, these represent the theoretical absolute maximum bitrate with the corresponding signal to noise ratio. Actual bitrates will always be lower, since will be limited by finite size memory and finite processing power.

Free Space.	Downlink			
Angle Coverage	99%	99%	90%	90%
Distance	1m	10m	1m	10m
P_{out}	-18 dBm	-18 dBm	-18 dBm	-18 dBm
$G_{antenna}$	+2 dBi	+2 dBi	+2 dBi	+2 dBi
PL	-25 dB	-45 dB	-25 dB	-45 dB
G_{body}	-34 dBi	-34 dBi	-33 dBi	-33 dBi
$P_{reciever}$	-75 dBm	-95 dBm	-74 dBm	-94 dBm
N_{input}	-110 dBm	-110 dBm	-110 dBm	-110 dBm
S/N	35 dB	15 dB	36 dB	16 dB
C_{max}	3.5 Mbit/s	1.5 Mbit/s	3.6 Mbit/s	1.6 Mbit/s

Table 8.3: Link budget calculations for the downlink at 300 kHz BW in free space.

8.5 Link in free space

We will now calculate the link budget for some theoretical test cases. The simplest case is to use the radio link in an environment without any reflections. (A possible scenario would be a small space vehicle that checks the condition of an astronaut out on a spacewalk.) The only spatial variation of the received field will be the inverse square decrease of the free space loss. The free space loss is [29]

$$PL = \left(\frac{\lambda}{4\pi d}\right)^2 \tag{8.11}$$

As we only have the line of sight component of the wave propagation from the base station to the implant, the gain of the implant is dependent on the position of the patient. The link budget calculations for two distances, 1 m and 10 m, and for two coverage percentages, 90% and 99%, are given in Table 8.5 and 8.6. For the downlink, the output power from the transmitter is set to the maximum limit. For the uplink, the output is set to 0 dBm. This gives an EIRP well below the limit in the specification. Even as we are using a lower EIRP in the uplink than in the downlink, the uplink has the higher capacity. This is due to the higher ambient noise levels at the base station receiver.

8.6 Link with isotropic scattering

We now take the case where we assume isotropic scattering around the patient. That is, the path loss will be equal to the free space loss, but we assume that the power is coming from an arbitrary angle and with an arbitrary phase. We do not account for any multipath fading. We can then use the mean gain of the implanted antenna as the effective gain. The mean gain is calculated from the radiation efficiency in Table 6.4. For the male phantom it was $5.1 \cdot 10^{-4}$, or -33

Free Space	Uplink			
Angle Coverage	**99%**	**99%**	**90%**	**90%**
Distance	**1 m**	**10 m**	**1 m**	**10 m**
P_{out}	0 dBm	0 dBm	0 dBm	0 dBm
G_{body}	-34 dBi	-34 dBi	-33 dBi	-33 dBi
PL	-25 dB	-45 dB	-25 dB	-45 dB
G_{base}	+2 dBi	+2 dBi	+2 dBi	+2 dBi
P_{input}	-57 dBm	-77 dBm	-56 dBm	-76 dBm
N_{input}	-95 dBm	-95 dBm	-95 dBm	-95 dBm
S/N	38 dB	18 dB	39 dB	19 dB
$C_{\max}$	3.8 Mbit/s	1.8 Mbit/s	3.9 Mbit/s	1.9 Mbit/s

Table 8.4: Link budget calculations for the uplink at 300 kHz BW in free space

Isotropic	Downlink	
Distance	**1.6 m**	**Measured**
P_{out}	-18 dBm	-18 dBm
$G_{antenna}$	+2 dBi	+2 dBi
PL	-29 dB	-24 dB
G_{body}	-33 dBi	-33 dBi
$P_{reciever}$	-78 dBm	-73 dBm
N_{input}	-110 dBm	-110 dBm
S/N	32 dB	37 dB
$C_{\max}$	3.2 Mbit/s	3.7 Mbit/s

Table 8.5: Link budget calculations for the downlink at 300 kHz BW with isotropic scattering. The measured data is for area E over the be, with a mean distance equal to 1.6 m.

dB. This is the same gain as in the case for 90% angle coverage in the free space example above. It gives the same S/N-ratios and bitrates, if we assume that the losses in each scattering point is such that the total energy is equal to what we get in the case of free space loss. In Tables 8.5 and 8.6 the performance is given for the distance to the bed in our model room. Both the theoretical free space loss at 1.6 m of -29 dB, with the same assumptions as before, and the actual mean path loss according to our measurements are used. The difference between the two is 5 dB, where the measured values are higher due to that they sum power coming from many different directions in the room.

8.7   Link in the room

Here we use the case of the patient being in the studied room, described in Chapter 7. We assume that all the energy from the transmitting antenna reaches us in the direction of the maximum gain of the patient. Thus, we will include the spatially varying field strength of the room, but not the angular dependence

Isotropic	Uplink	
Distance	1.6 m	Measured
P_{out}	0 dBm	0 dBm
G_{body}	-33 dBi	-33 dBi
PL	-29 dB	-24 dB
G_{base}	+2 dB	+2 dB
P_{input}	-60 dBm	-55 dBm
N_{input}	-95 dBm	-95 dBm
S/N	35 dB	40 dB
C_{max}	3.5 Mbit/s	4.0 Mbit/s

Table 8.6: Link budget calculations for the uplink at 300 kHz BW with isotropic scattering. The measured data is for area E over the be, with a mean distance equal to 1.6 m.

Room	Downlink	
Space Coverage	99%	90%
P_{out}	-18 dBm	-18 dBm
$G_{antenna}$	+2 dBi	+2 dBi
PL	-47 dB	-34 dB
G_{body}	-26 dBi	-26 dBi
$P_{reciever}$	-89 dBm	-76 dBm
N_{input}	-110 dBm	-110 dBm
S/N	21 dB	34 dB
C_{max}	2.1 Mbit/s	3.4 Mbit/s

Table 8.7: Link budget calculations for the downlink at 300 kHz BW in the room.

of the gain of the implanted antenna. Furthermore, we assume that the patient is male, and is lying on the bed in the room. The link budget calculations are given in Table 8.7 and 8.8.

8.8 Link to the bed

If we assume that all of the energy is coming from the direction of the base station, even in the case with scattered waves inside the model room, we can calculate the combined effects of the variation with angle and the spatial variation. We take the case of a link between the base station on the table and a patient sitting on the bed. The base station is assumed to have a vertically polarized antenna. The patient is male, and is lying on the bed. We take the radiation in the transversal plane as the antenna gain. The vertical component of the antenna gain from the patient, which was given in Chapter 5, is -31dBi. The variation when the patient rotates in the bed is 20 dB for 99% angle coverage and 15 dB for 90% angle coverage.

Room	Uplink	
Space Coverage	**99%**	**90%**
P_{out}	0 dBm	0 dBm
G_{body}	-26 dBi	-26 dBi
PL	-47 dB	-34 dB
G_{base}	+2 dBi	+2 dBi
P_{input}	-71 dBm	-58 dBm
N_{input}	-95 dBm	-95 dBm
S/N	24 dB	37 dB
C_{max}	2.4 Mbit/s	3.7 Mbit/s

Table 8.8: Link budget calculations for the uplink at 300 kHz BW in the room.

Man on Bed	Downlink			
Space Coverage	**99%**	**99%**	**90%**	**90%**
Angle Coverage	**99%**	**90%**	**99%**	**90%**
P_{out}	-18 dBm		-18 dBm	
$G_{antenna}$	+2 dBi		+2 dBi	
PL	-47 dB	-47 dB	-34 dB	-34 dB
G_{body}	-49 dBi	-34 dBi	-49 dBi	-34 dBi
$P_{reciever}$	-112 dBm	-97 dBm	-99 dBm	-84 dBm
N_{input}	-110 dBm	-110 dBm	-110 dBm	-110 dBm
S/N	-2 dB	13 dB	11 dB	26 dB
C_{max}	210 kbit/s	1.3 Mbit/s	1.1 Mbit/s	2.6 Mbit/s

Table 8.9: Link budget calculations for the downlink at 300 kHz BW to the bed.

$$G_{99\%} = -31 \text{ dBi} - 20 \text{ dB} = -51 \text{ dBi} \qquad (8.12)$$
$$G_{90\%} = -31 \text{ dBi} - 15 \text{ dB} = -46 \text{ dBi} \qquad (8.13)$$

The free space loss to the bed is -29 dB. The variation over the bed is -47 dB for 99% spatial coverage and -34 dB for 90% spatial coverage as above. The down and uplink S/N are then given in Table 8.9 and 8.10.

8.9   Comparison with the ITU-R budget

It is interesting to compare our figures with those used in the ITU-R document. The document gives the gain of the implanted antenna as -31.5 dBi. This is worse than our simulations show, but in agreement with the gain obtained from the MICS phantom, which gave a maximum gain of -33 dBi with the circumference antenna. Furthermore, the ITU-R document gives a margin, with the assumption that spatial diversity is used, of 10 dB. Our measured spatially varying path loss needed an excess loss margin of 11 dB to cover 97% of the

Man on Bed	Uplink			
Space Coverage	**99%**	**99%**	**90%**	**90%**
Angle Coverage	**99%**	**90%**	**99%**	**90%**
P_{out}	0 dBm		0 dBm	
G_{body}	-49 dBi	-34 dBi	-49 dBi	-34 dBi
PL	-47 dB	-47 dB	-34 dB	-34 dB
G_{base}	+2 dBi	+2 dBi	+2 dBi	+2 dBi
P_{input}	-94 dBm	-79	-81 dBm	-66 dBm
N_{input}	-95 dBm	-95 dBm	-95 dBm	-95 dBm
S/N	1 dB	16 dB	14 dB	29 dB
$C_{\max}$	350 kbit/s	1.6 Mbit/s	1.4 Mbit/s	2.9 Mbit/s

Table 8.10: Link budget calculations for the downlink at 300 kHz BW to the bed.

Factor	Pol.Div	Pol&Spatial Div.
Patient arm movement	5 dB	5 dB
Patient age and sex	3 dB	3 dB
Excess loss over free space	18 dB	10 dB
Switching Pol. Div.	3 dB	3 dB
Patient orientation	2.5 dB	2.5 dB
Sum	**31.5 dB**	**23.5 dB**

Table 8.11: Summary of variables in the link budget.

area studied and 18 dB to cover 99% of the same area. These figures are given without any spatial diversity, and under the assumption of optimal polarization.

The ITU-R document uses an excess loss parameter, set to 15 dB, which should cover patient orientation, antenna misalignment, obstructions of line of sight and polarization losses. When the measurement of the room was performed the influence of another person in the room was only studied qualitatively, but an obstruction of the line of sight leads to an increased path loss of 10 dB. This only leaves 5 dB to cover for patient movements and polarization loss. The added margin for arm movement was quantified to 5 dB in Chapter 6. As the polarization of a signal is kept constant when it is scattered in the room, polarization diversity is a necessity at the base station, to be used both in the up- and the down-link. A switched polarization scheme ideally gives a maximum added loss of 3 dB relative the optimum combining case.

The two factors of fading margin and excess loss in the ITU-R document add up to 25 dB. If we add our corresponding factors as given in this thesis we get the results in Table 8.11. Judging from this table we have essentially the same result, but with one important difference: the ITU-R numbers are supposed to include influence of a second person in the room, which in our measurement leads to an added loss of 10 dB.

8.10   Conclusion

Our calculations indicate that a radio link using the MICS standard should work. The initial ITU-R calculation, though, is optimistic regarding the excess loss in the channel due to the interference pattern. The variation between different patients is not addressed in the ITU-R calculations. Furthermore, the ITU-R includes only spatial diversity. Our measurements and simulations show that the polarisation is not shifted by the channel. Thi indicates that introduction of polarization diversity is a necessity in order to get a reliable link to the patient, as we will have very little control of the polarisation of the implanted antenna.

The link budget analysis in this chapter has been done assuming a one-to-one antenna link. That is, it has considered a compact base station with a single or dual polarized antenna, but has not made use of any spatial diversity. If we increase the complexity of the base station to include a second set of antennas at a different position, it will reduce two of the terms given in the calculation: the excess loss to the path loss will be lowered, and also the gain dependence on the rotational position of the body will be reduced. The introduction of spatial diversity gives a limit on the minimal base station size, since the general ideal distance between the two antennas is $\lambda/2$, or 37 cm. This would give a base-station with four antennas, and at least switching diversity between them all. If the patient is stationary, the simplified version outlined in the ITU-R paper of using the same transmitting antenna as the one that received the best signal when receiving, should work satisfactory.

Chapter 9

Conclusions

Based on the calculations in the previous chapter we conclude the MICS system, as specified today, is working and gives the benefit of a larger communication distance then the contemporary systems. There is a possibility to increase the communication speed above 300 kbit/s. That would require complex modulation schemes, with higher power consumption. Another option is to revise the specification to allow for a higher bandwidth, but an increase of the bandwidth will increase the noise level at the input. An increase of the bandwidth by 10 times to 2.5 Mhz, giving an approximate raw bit rate of 2.5 Mbit/s with simple modulation, would also increase the noise by 10 dB. That effectively reduce the distance over which the link can be expected to work at a given quality level, when keeping the modulation, coding and receiver design the same.

The results from our investigations that we would like to stress are the following:

9.0.1 Regarding MICS

- Our simulations and measurements does not show that the current standard for the MICS system is unsuitable for implementation.

9.0.2 Regarding the antenna

- When analyzing a system including an implanted antenna, the antenna should not be viewed in isolation from the body; rather the body should be viewed as a part of the antenna, similar to a radome. This since the size, shape, and composition of the body influence the radiation pattern and the efficiency.

- The results from the theoretical analysis of antennas in matter combined with the characteristics of an electromagnetic wave going into the human body, show that magnetic dipole antennas and resonant dipole antennas are the most efficient ones for use in an implant.

- An implanted antenna should be insulated from the body tissues as much as possible.

- The low power of the MICS system gives SAR values well below the limits.

9.0.3   Regarding the wave propagation

- The polarization characteristics of a transmitted wave are retained in the reflections in a small room, which implies that a polarization diversity scheme should be used. This as we, in general, will not have any control of the polarization of the implanted antenna.

- There is a pronounced standing wave pattern in a small room at MICS frequencies, that at some positions constitutes an excess loss over free space loss. This makes spatial diversity at the base station beneficial.

9.0.4   Regarding methods

- At MICS frequencies FDTD is an effective tool for analyzing wave propagation in confined spaces, like a room. The fidelity of the simulations with actual measurements is good.

9.0.5   Regarding Implementation

- We reccomend that a basestation for the MICS system implements both spatial and polarization diversity.

9.1   Future work

There is today an ongoing investigation of the sizes of the population in Europe. When this data becomes available, it would be useful to make a statistical investigation of the dependence of the antenna gain on the body size and sex.

As FDTD was shown to be an effective tool for analyzing the wave propagation, it is well suited for analysis and characterization of the MICS channel, especially in places where actual measurements are complicated to perform, such as in the operating theatre during surgery. With refinement of the simulation tool, most notably the inclusion of the technique of sub-gridding, the impact of the body with the implant on the standing wave pattern at MICS frequencies can be investigated. The steady increase in available computing power will also aid this.

Simulated fat tissue and skin tissue are under development for use in measurements. The use of them requires new physical phantoms to be developed.

Appendix A

Definition of Reference Planes.

The transversal, sagittal and frontal planes are defined relative to the human torso, as illustrated in Figures A.1, A.2 and A.3. These are the same names and definitions that are used in medicine [70].The vertical and horizontal planes are defined relative to the ground. The transversal plane will coincide with the horizontal plane for a patient standing up, and with the frontal plane for a patient who is laying on his back in a bed. Vertical polarization is defined as a linearly polarized electromagnetic wave propagating with the electromagnetic field vector coinciding with the vertical plane. Horizontal polarization is defined as a linearly polarized electromagnetic wave propagating with the electromagnetic field vector parallel with the horizontal plane.
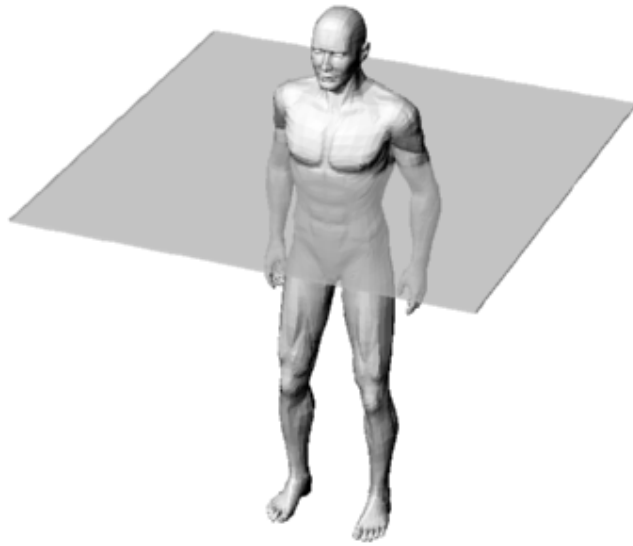
Figure A.1: The Transversal plane.

Figure A.2: The Sagittal plane.
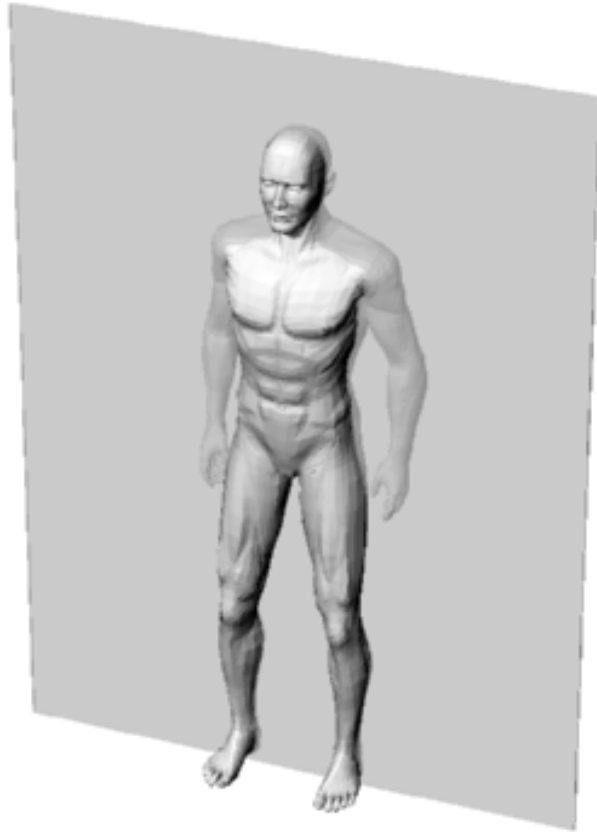
Figure A.3: The Frontal plane.

Appendix B

Vector Waves

The definition of spherical vector waves can be found in the different textbooks, [53]. Here we define them using spherical harmonics:

$$\vec{A}_{1\kappa ml}(\theta,\phi) = \frac{1}{\sqrt{l(l+1)}} \nabla \times (\vec{r}Y_{\kappa ml}(\theta,\phi)) \tag{B.1}$$

$$\vec{A}_{2\kappa ml}(\theta,\phi) = \frac{1}{\sqrt{l(l+1)}} r \nabla Y_{\kappa ml}(\theta,\phi) \tag{B.2}$$

$$\vec{A}_{3\kappa ml}(\theta,\phi) = \widehat{r}Y_{ml}(\theta,\phi) \tag{B.3}$$

The following definition of the spherical harmonics is used

$$Y_{\kappa ml}(\theta,\phi) = \sqrt{\frac{\varepsilon_m}{2\pi}}\sqrt{\frac{2l+1}{2}\frac{(l-m)!}{(l+m)!}}P_l^m(\cos\theta)\left\{ \begin{array}{c} \cos(m\phi) \\ \sin(m\phi) \end{array} \right\} \tag{B.4}$$

where $\varepsilon_m = 2 - \delta_{m0}$ and κ, l, m take the values

$$\kappa = \left\{ \begin{array}{c} even \\ odd \end{array} \right\} \tag{B.5}$$

$$m = 0, 1, 2, \ldots, l \tag{B.6}$$

$$l = 0, 1, 2, \ldots \tag{B.7}$$

In the current application the index l will never take the value 0, since there are no monopole antennas. The vector spherical harmonics constitute an orthogonal set of vector function on the unit sphere

$$\int_\Omega \vec{A}_{\tau n}(\theta,\phi) \cdot \vec{A}_{\tau'n'}(\theta,\phi)\,d\Omega = \delta_{\tau\tau'}\delta_{nn'} \tag{B.8}$$

where the integration is over the unit sphere and where $n = \kappa ml$. The outgoing divergence-free spherical vector waves are defined by

$$
\begin{aligned}
\vec{u}_{1n}\left(\vec{r}\right) &= h_l\left(kr\right)\vec{A}_{1n}\left(\theta,\phi\right) && \text{(B.9)}\\
\vec{u}_{2n}\left(\vec{r}\right) &= \frac{1}{k}\bigtriangledown\times\left(h_l\left(kr\right)\vec{A}_{1n}\left(\theta,\phi\right)\right)\\
&= h'_l\left(kr\right)\vec{A}_{2n}\left(\theta,\phi\right)+\frac{1}{kr}h_l\left(kr\right)\left(\vec{A}_{2n}\left(\theta,\phi\right)+\sqrt{l\left(l+1\right)}\vec{A}_{3n}\left(\theta,\phi\right)\right)
\end{aligned}
$$

where $h_l\left(kr\right)=h_l^{(2)}\left(kr\right)$ is the spherical Hankel function of the second kind. The asymptotic behavior in the far-zone and the limiting values in the near-zone of the spherical Hankel functions are

$$
h_l^{(2)}\left(kr\right)\rightarrow\begin{cases} j^{l+1}\frac{e^{-jkr}}{kr} & \text{when }\left|k\right|r\rightarrow\infty\\ j\left(2l+1\right)!\left(kr\right)^{-(l+1)} & \text{when }\left|k\right|r\rightarrow0 \end{cases} \tag{B.10}
$$

B.1   The dipole antennas

The most frequently described dipole antennas are the magnetic dipole with the dipole moment $\vec{m}=m\widehat{z}$ and the electric dipole antenna with the dipole moment $\vec{p}=p\widehat{z}$. These antennas radiate the partial waves $a_{1e01}\vec{u}_{1e01}\left(r\right)$ and $a_{2e01}\vec{u}_{2e01}\left(r\right)$, respectively. The explicit expressions for the electric fields are well known [71], and follow from the equations above. The electric field from the magnetic dipole reads

$$
\vec{E}\left(r,\theta\right)=\frac{j\omega k^2 m\mu_0}{4\pi}\sin\left(\theta\right)\left(\frac{1}{jkr}+\frac{1}{\left(jkr\right)^2}\right)e^{-jkr}\widehat{\phi} \tag{B.11}
$$

The electric field from an electric dipole reads

$$
\vec{E}\left(r,\theta\right)=E_r\left(r,\theta\right)\widehat{r}+E_\theta\left(r,\theta\right)\widehat{\theta} \tag{B.12}
$$

where

$$
\begin{aligned}
E_r\left(r,\theta\right) &= -\frac{j\omega p}{4\pi}Z_m k^2 2\cos\left(\theta\right)\left(\frac{1}{\left(jkr\right)^2}+\frac{1}{\left(jkr\right)^3}\right)e^{-jkr} && \text{(B.13)}\\
E_\theta\left(r,\theta\right) &= -\frac{j\omega p}{4\pi}Z_m k^2\sin\left(\theta\right)\left(\frac{1}{jkr}+\frac{1}{\left(jkr\right)^2}+\frac{1}{\left(jkr\right)^3}\right)e^{-jkr} && \text{(B.14)}
\end{aligned}
$$

where Z_m is the complex wave impedance and k is the complex wave number.

$$
\begin{aligned}
Z_m &= \sqrt{\frac{\mu_0}{\varepsilon_c}} && \text{(B.15)}\\
k &= \omega\sqrt{\mu\varepsilon_c} && \text{(B.16)}
\end{aligned}
$$

It is seen that in the near-zone, the electric field for the magnetic dipole is one order weaker than the electric field for the electric dipole. Thus the induced currents near the antenna are weaker for the magnetic dipole, $\vec{J}_{ind}(r) = \sigma \vec{E}(r)$.

Appendix C

Analytic Solutions

The analytic solutions to plane wave propagation through, and scattering from, stratified slabs, cylinders and spheres can be found in the literature. For completeness, we here present the analytic solutions for a plane wave propagation through a stratified slab and cylinder. This corresponds to a geometry in one and two dimensions, respectively. The solutions presented hold for lossy materials, but assume that the material is non-magnetic, for simplicity. All the materials discussed in the thesis are non-magnetic.

C.1   One-dimensional

Take an incident linear polarized plane wave

$$\vec{E}(z, \omega) = E_0 e^{-jk_0 z} \hat{y} \tag{C.1}$$

Let it impinge upon a layered structure with interfaces at $z = z_i, i = 1, ..., N$. There is vacuum for $z < z_1$ and a homogeneous medium for $z > z_N$. Outside the structure there is vacuum. Each layer has a constant relative permittivity ε_{eri} and conductivity σ_{ei}, which gives a constant wave-number k_i

$$k_i = \omega \sqrt{\mu_0 \left(\varepsilon_0 \varepsilon_{er,i} - \frac{j\sigma_{e,i}}{\omega} \right)} \tag{C.2}$$

and a constant wave impedance Z_i

$$Z_i = \sqrt{\frac{\mu_0}{\varepsilon_0 \varepsilon_{er,i} - \frac{j\sigma_{e,i}}{\omega}}} \tag{C.3}$$

The electric field in the different regions becomes

$$\begin{cases} E_{y0}(z, \omega) = E_0 \left(e^{-jk_0 z} + \Gamma_r e^{jk_0 z} \right) & -\infty < z < z_1 \\ E_{yn}(z, \omega) = C'_n e^{-jk_n z} + C''_n e^{jk_n z} & z_n < z < z_{n+1} \\ E_{yN}(z, \omega) = \Gamma_t E_0 e^{-jk_N z} & z_N < z < \infty \end{cases} \tag{C.4}$$

where Γ_r is the reflection coefficient and Γ_t is the transmission coefficient. The unknown coefficients are determined from the boundary conditions. Continuity of the electric and the magnetic fields at all interfaces gives

$$[L_n]\begin{pmatrix} C'_{n-1} \\ C''_{n-1} \end{pmatrix} = [K_n]\begin{pmatrix} C'_n \\ C''_n \end{pmatrix} \tag{C.5}$$

$$[L_n] = \begin{pmatrix} e^{-jk_{n-1}z_n} & e^{jk_{n-1}z_n} \\ Z_{n-1}^{-1}e^{-jk_{n-1}z_n} & -Z_{n-1}^{-1}e^{jk_{n-1}z_n} \end{pmatrix} \tag{C.6}$$

and

$$[K_n] = \begin{pmatrix} e^{-jk_n z_n} & e^{jk_n z_n} \\ Z_n^{-1}e^{-jk_n z_n} & -Z_n^{-1}e^{jk_n z_n} \end{pmatrix} \tag{C.7}$$

Here the coefficients are

$$C'_0 = E_0 \tag{C.8}$$
$$C''_0 = \Gamma_r E_0 \tag{C.9}$$
$$C'_N = \Gamma_t E_0 \tag{C.10}$$
$$C''_N = 0 \tag{C.11}$$

From Equation C.5 it is straightforward to compute all the coefficients. We relate C'_N and C''_0 to C'_0:

$$\begin{pmatrix} C'_0 \\ C''_0 \end{pmatrix} = [M]\begin{pmatrix} C'_N \\ 0 \end{pmatrix} \tag{C.12}$$

where

$$[M] = [L_1]^{-1}[K_1][L_2]^{-1}[K_2]\cdots[L_N]^{-1}[K_N] \tag{C.13}$$

From Equation C.12 we obtain C''_0 and C'_N in terms of the known amplitude $C'_0 = E_0$. The other amplitudes are then given by Equation C.5.

C.2 Two-dimensional

In two dimensions, we study the cylindrical case. The method is similar to the one used in the one-dimensional case. The fields in all regions are expanded in cylindrical waves and the relations between the coefficients are derived from boundary conditions.

Take an infinitely long stratified cylinder with the z-axis as the axis of symmetry. The cylinder is stratified with interfaces at the radii $\rho_i, i = 1, \cdots, N$ with $\rho_{n-1} < \rho_n$. In the region $\rho_{n-1} < \rho \leq \rho_n$ the complex permittivity is ε_{cn} and the wave-number is $k_n = \omega\sqrt{\mu_0\varepsilon_{cn}}$. In the region $\rho < \rho_1$ the corresponding values are ε_{c1} and k_1. Outside the cylinder, $\rho > \rho_N$ there is vacuum, $\varepsilon_{N+1} = \varepsilon_0$ and $k_{N+1} = k_0$.

In this case we solve the Maxwell equation in the planar coordinates, (ρ, ϕ). There are two cases: the TE-case, where $\vec{E}(\rho, \phi) = \hat{z}E(\rho, \phi)$, and the TM-case, where $\vec{H}(\rho, \phi) = \hat{z}H(\rho, \phi)$. Since only minor details differ between the two cases, we give the analysis in detail only for the TE-case.

The electric field in the $N + 1$ regions satisfy the two-dimensional Helmholtz equation

$$\bigtriangledown^2 E_n(\rho, \phi) + k_n^2 E_n(\rho, \phi) = 0; \ \rho_{n-1} < \rho \leq \rho_n \tag{C.14}$$

This equation has the following two independent sets of normalized solutions

$$\chi_m(\rho, \phi; k_n) = \sqrt{\frac{\epsilon_m}{2\pi}} J_m(k_n \rho) \cos(m\phi) \tag{C.15}$$

$$\Psi_m(\rho, \phi; k_n) = \sqrt{\frac{\epsilon_m}{2\pi}} H_m^{(2)}(k_n \rho) \cos(m\phi) \tag{C.16}$$

where $\epsilon_0 = 1$ and $\epsilon_m = 2$, if $m > 0$. These are the solutions that are even in ϕ. There are corresponding solutions that are odd in ϕ and have a $\sin(m\phi)$ dependence but they are not used here. The cylindrical Bessel functions $J_m(k\rho)$ are finite at $\rho = 0$, whereas the Hankel functions, $H_m^{(2)}(kr)$, are infinite. The Hankel functions satisfy a radiation condition at $\rho = \infty$. Outside the cylinder there is an incident plane wave $E^i(\rho, \phi)$ and a scattered cylindrical wave $E^s(\rho, \phi)$. In the other regions, $\rho \leq \rho_N$, the electrical fields are denoted $E_n(\rho, \phi)$. The following expansions of the fields are adopted

$$E^i(\rho, \phi) = \sum_{m=0}^{\infty} \alpha_m^{N+1} \chi_m(\rho, \phi; k_0) \tag{C.17}$$

$$E^s(\rho, \phi) = \sum_{m=0}^{\infty} \beta_m^{N+1} \Psi_m(\rho, \phi; k_0) \tag{C.18}$$

$$E_n(\rho, \phi) = \sum_{m=0}^{\infty} (\alpha_m^n \chi_m(\rho, \phi; k_n) + \beta_m^n \Psi_m(\rho, \phi; k_n)) \tag{C.19}$$

$$E_1(\rho, \phi) = \sum_{m=0}^{\infty} \alpha_m^1 \chi_m(\rho, \phi; k_1); \ 0 \leq \rho \leq \rho_1$$

where we have used the condition that the electrical field is bounded everywhere and that the reflected wave should satisfy a radiation conditions. The boundary conditions at the interfaces are that the tangential electric and magnetic fields are continuous at the interfaces, i.e.,

$$\begin{cases} E_n(\rho_n, \phi) = E_{n+1}(\rho_n, \phi) \\ \frac{\partial E_n(\rho_n, \phi)}{\partial \rho} = \frac{\partial E_{n+1}(\rho_n, \phi)}{\partial \rho} \end{cases} \tag{C.20}$$

From the orthogonality of the $\cos{(m\phi)}$ functions over the circle, the following relations are obtained:

$$[K_1]\begin{pmatrix} \alpha_m^1 \\ 0 \end{pmatrix} = [L_1]\begin{pmatrix} \alpha_m^2 \\ \beta_m^2 \end{pmatrix} \tag{C.21}$$

and for $n = 2, \ldots N$

$$[K_n]\begin{pmatrix} \alpha_m^n \\ \beta_m^n \end{pmatrix} = [L_n]\begin{pmatrix} \alpha_m^{n+1} \\ \beta_m^{n+1} \end{pmatrix} \tag{C.22}$$

where the azimuthal index m has been suppressed in the matrices. The matrices read

$$[K_n] = \begin{pmatrix} J_m\left(k_n\rho_n\right) & H_m^{(2)}\left(k_n\rho_n\right) \\ k_n J_m'\left(k_n\rho_n\right) & k_n H_m'\left(k_n\rho_n\right) \end{pmatrix} \tag{C.23}$$

$$[L_n] = \begin{pmatrix} J_m\left(k_{n+1}\rho_n\right) & H_m^{(2)}\left(k_{n+1}\rho_n\right) \\ k_{n+1} J_m'\left(k_{n+1}\rho_n\right) & k_{n+1} H_m'\left(k_{n+1}\rho_n\right) \end{pmatrix} \tag{C.24}$$

We now relate α_m^1 to α_m^{N+1} and β_m^{N+1}

$$\begin{pmatrix} \alpha_m^{N+1} \\ \beta_m^{N+1} \end{pmatrix} = [M]\begin{pmatrix} \alpha_m^1 \\ 0 \end{pmatrix} \tag{C.25}$$

where

$$[M] = \left[L^N\right]^{-1}\left[K^N\right]\left[L^{N-1}\right]^{-1}\left[K^{N-1}\right]\cdots\left[L^1\right]^{-1}\left[K^1\right] \tag{C.26}$$

The amplitude of the incident wave α_m^{N+1} is known. It is then easy to express β_m^{N+1} and α_m^1 in terms of α_m^{N+1}. From equation C.22 we get all of the other amplitudes.

The expansion coefficients α_m^{N+1} for an incident plane wave $\vec{E}^i\left(r\right) = E_0 e^{-jk_0 x}\widehat{z}$ are obtained from the expansion, cf., [72]

$$e^{-jkx} = e^{-jk\rho\cos(\phi)} = J_0\left(k\rho\right) + 2\sum_{m=1}^{\infty} j^{-m}J_m\left(k_0\rho\right)\cos{(m\phi)} \tag{C.27}$$

Hence,

$$\alpha_m^{N+1} = E_0\sqrt{2\pi\left(2 - \delta_{m,0}\right)}j^{-m} \tag{C.28}$$

Appendix D

FDTD

The Finite Difference in the Time Domain method, or FDTD, is a powerful method for solving Maxwell's equations in the three dimensions and in time. It was proposed by Yee in 1966 and is described in a number of publications [66]. It subdivides the volume to be investigated into small cubic volumes, each one called a voxel for *volume pixel*. In these voxels, Maxwell's equations are solved iteratively as time is stepped forward. The trick in FDTD is to update the E- and H-components in the grid in a leapfrog scheme using the finite difference form of the curl operators on the fields that surround the component. The time evolution of the electromagnetic fields are specified by

$$\nabla \times \vec{H} \quad = \quad \frac{\partial}{\partial t}\varepsilon\vec{E} + \sigma_E\vec{E} \qquad\qquad (D.1)$$

$$\nabla \times \vec{E} \quad = \quad -\frac{\partial}{\partial t}\mu\vec{H} - \sigma_H\vec{H} \qquad\qquad (D.2)$$

where σ_H is a term for the magnetic losses in the material. The equations are discretized by using finite-difference approximations in both time and space. The first partial space and time derivatives leads to

$$\frac{\partial F(i,j,k,n)}{\partial x} \quad = \quad \frac{F(i+1/2,j,k,n) - F(i-1/2,j,k,n)}{\Delta x} + O[(\Delta x)^2] \quad (D.3)$$

$$\frac{\partial F(i,j,k,n)}{\partial t} \quad = \quad \frac{F(i,j,k,n+\frac{1}{2}) - F(i,j,k,n-\frac{1}{2})}{\Delta t} + O[(\Delta t)^2] \quad (D.4)$$

where $F(i,j,k,n)$ is the electric or magnetic field at time $n \cdot \Delta t$ and i,j,k are indices to the three-dimensional grid. $O[(\Delta x)^2]$ and $O[(\Delta t)^2]$ are error terms. We apply this to the generic formulations of Maxwell's equation. We can then calculate the time progression of transient wave phenomena in a three-dimensional grid. An important aspect of FDTD is the numerical stability of the solutions. The time step is limited by the criteria in Equation D.5. This effectively puts a limit on the length of the signals that can be investigated. It

also puts a limit to the effective mesh size. A reduction of the mesh size by two gives an increase in memory requirements by 8 and in time by 16.

$$\Delta t \leq \frac{1}{c\sqrt{\frac{1}{(\Delta x)^2} + \frac{1}{(\Delta y)^2} + \frac{1}{(\Delta z)^2}}} \tag{D.5}$$

D.1   Boundary Conditions

At the bounds of the simulation space, we need to absorb the electromagnetic energy in order to simulate an infinite space. This is done by adding an absorbing boundary condition (ABC) on the outside of the simulation space. A typical ABC is the perfectly matched layer (PML) [66]. This has the form of a material that absorbs both electric and magnetic energy by having both an electrical conductivity σ and a magnetic conductivity σ_M. On the outside of the PML layer a perfect electric conductor (PEC) is placed. This reflects all energy back into the simulation space, but since this energy traverse the PML two times very little energy will be left when the wave re-enters the simulation space. The equations in the PML read

$$\varepsilon_0 \frac{\partial \vec{E}}{\partial t} + \sigma \vec{E} \quad = \quad \bigtriangledown \times \vec{H} \tag{D.6}$$

$$\mu_0 \frac{\partial \vec{H}}{\partial t} + \sigma_M \vec{H} \quad = \quad - \bigtriangledown \times \vec{E} \tag{D.7}$$

$$Z_{PML} = \left(\frac{\mu_0 + \sigma^*/j\omega}{\varepsilon_0 + \sigma/j\omega} \right)^{\frac{1}{2}} \tag{D.8}$$

D.2   SEMCAD

The implementation of FDTD used in our work has mainly been the commercial software package SEMCAD by Shmid & Partner Engineering AG [55]. This has implemented non-uniform grids, which saves memory by using a variable grid size to capture fine local structures. Verifications of the implementation have been published [56]. The program has been run on a dual-processor 2.8 GHz Pentium 4 equipped PC with 2 GB RAM memory per processor. All simulations have been discretized to at least 10 voxels per wavelength in the material.

Appendix E

Numerical Phantoms

The human phantoms used on this thesis were all generated by the Poser program. That program is written as a tool for artists and animators. It features human shapes that are possible to change, both the position of the body parts and the size and shape of the body. It includes a couple of human and animal figures, and additional ones are available from third party manufacturers.

When a figure is positioned as intended in Poser it is then exported as a DXF file, describing the figure as a shell. This shell will typically not be "watertight", or closed, which is a requirement for import of a shape into SEMCAD. It will consist of a shell of the body, and one or more additional shells: eyes, tongue etc., depending on the figure chosen. DXF is a format that originally comes from AutoDesk, and stands for Drawing eXchange Format. It uses vectors to describe the shape(s) in the file.

The DXF file of the phantom is imported into Rhinoceros, which is a NURBS modelling program. (NURBS reads as Non-Uniform Rational B-Splines, and is a general mathematical description of 3D shapes.) In Rhinoceros the shapes are scaled in order to get the desired height in SEMCAD. Rhinoceros is also used to generate some of the pictures of the phantoms used in this thesis. The desired shape is then exported as a STL file. STL is a format for stereo-lithography, and is mainly used for rapid prototyping.

The STL file is checked by the Unix-utility ADMesh in order to make sure that it is a closed surface. If the surface contains holes, the utility is used to close them. This is necessary when generating reduced phantoms, which are missing legs and/or arms. Care should be taken to make sure that all triangles in the STL file are defined in the same way, clockwise or counterclockwise. Otherwise SEMCAD will not be able to read the file correctly. The commands used for ADMesh is of the form

```
admesh -f -d -b 'newname.stl' oldname.stl
```

The checked STL file with the closed and corrected shape is then imported into SEMCAD to be used as a numerical phantom. Due to that only the shell of the figure is generated, the phantom is simulated as a homogenous structure.

The benefit of this procedure is that phantoms of different body positions and shapes can easily be generated, and that the process is repeatable. It is also possible to generate some animals in this way, e.g. dogs and rats.

The drawback is that the shapes are originally intended for marketing purposes, and are thus idealized versions of human shapes. They do probably not represent any mean or median human shape, neither man nor woman. In the thesis, the shapes have been used in their default proportions, in order to have a good repeatability of the generation process.

Appendix F

Tissue Simulation

F.1 Modelling of materials

Modelling of the electromagnetic properties of polar liquids is often done by the Debye model

$$\varepsilon_r^* = \varepsilon_\infty + \frac{\varepsilon_s - \varepsilon_\infty}{1 + j\omega\tau} = \varepsilon_\infty + \frac{\varepsilon_s - \varepsilon_\infty}{1 + \omega^2\tau^2} - j\left(\frac{\omega\tau\left(\varepsilon_s - \varepsilon_\infty\right)}{1 + \omega^2\tau^2}\right) \qquad \text{(F.1)}$$

Here ε_s is the static permittivity, ε_∞ is the high frequency permittivity and τ is the relaxation time. This models the general frequency dependence of the permittivity of the polar liquid, and is valid for water for the frequencies in this thesis. It is not a general model applicable to all materials, frequencies and temperatures. To get an accurate modelling of water over temperature and at high frequencies more advanced models have to be use, such as the bimodal relaxation time expression

$$\varepsilon_r = \varepsilon_\infty + \frac{\varepsilon_s - \varepsilon_2}{1 + j\omega\tau_D} + \frac{\varepsilon_2 - \varepsilon_\infty}{1 + j\omega\tau_2} \qquad \text{(F.2)}$$

where ε_s is the static permittivity at low frequencies, ε_∞ is the permittivity at high frequencies and τ_D, τ_2 are temperature dependent relaxation times [73].

To the Debye model we can add the conductivity from Equation 4.12

$$\varepsilon_r^* = \varepsilon_\infty + \frac{\varepsilon_s - \varepsilon_\infty}{1 + \omega^2\tau^2} - j\left(\frac{\omega\tau\left(\varepsilon_s - \varepsilon_\infty\right)}{1 + \omega^2\tau^2} + \frac{\sigma_{DC}}{\omega\varepsilon_0}\right) \qquad \text{(F.3)}$$

Sometimes the susceptibility is also used as a material parameter. This is defined as

$$\chi = \frac{\vec{P}}{\varepsilon_0\vec{E}} = \frac{\varepsilon}{\varepsilon_0} - 1 \qquad \text{(F.4)}$$

where $\vec{P} = \vec{D} - \varepsilon_0\vec{E}$ is the polarization of the material.

Material	ε'	σ_e
Muscle	62.5	9.0
Brain	50.3	7.5
Lung	32.6	4.3
Bone Cast	9.3	1.1
Bone Liquid	9.1	066

Table F.1: Table Caption

HEC, which is a part of published recipes of tissue equivalent liquids [24], is used to reduce the real part of the permittivity ε. In the Debye model ε is dependent on the relaxation time τ

$$\tau = \frac{4\pi\eta r^3}{kT} \tag{F.5}$$

where k is Bolzmans constant, T is the absolute temperature of the material, r is the mean distance between molecules and η is the viscosity. By increasing the viscosity by adding HEC we increase the time constant and decrease the real part of the permittivity as in equation F.1.

To simulate lung tissue micro-spheres are used. These are small spheres filled with an inert gas. The ratio proposed in [24] is 47% volume of muscle tissue liquid and 53% volume of micro-spheres. The micro-spheres used by Hartsgrove et.al. have a diameter of 30-180um. We have used micro-spheres made of plastic filled with hydrocarbon (typically isobutane or isopentane) from the manufacturer Expancel. They were mainly used in the experiments to make a low permittivity material with the same properties as fat tissue.

F.2   Calculation of mixtures

The effective electromagnetic properties of mixtures of materials are not trivial to calculate. An overview is given in [73]. We have investigated the use of these formulas to calculate a mixture that would simulate the electromagnetic properties of skin and fat. When these materials are available, preferable in a semi-rigid form, measurement of the dependence of antennas on the makeup of the air to body interface becomes possible. The Maxwell-Garnett formula was investigated. It models the mixture as spherical inclusions of one material inside a second, homogenous, background material. The inclusions have the complex permittivity ε_i and the background has the complex permittivity ε_b. The mixtures effective complex permittivity ε_{eff}, with the inclusions taking up a volume fraction of f, will then become

$$\varepsilon_{eff} = \varepsilon_b + 3f\varepsilon_b \frac{\varepsilon_i - \varepsilon_b}{\varepsilon_i + 2\varepsilon_b - f(\varepsilon_i - \varepsilon_b)} \tag{F.6}$$

This mixture model was shown to be valid for mixtures between water and sugar. However, when tested against mixtures between a background of dis-

tilled water and an inclusion of saline solution, the approximation of spherical inclusions did not work well. Following the same reasoning as in Equation F.3, a conductivity term was added to the Maxwell-Garnett formula

$$\varepsilon_{effH}\left(\omega\right) = \varepsilon_{eff}\left(\omega\right) - j\frac{\sigma_{ion}}{\omega\varepsilon_0} \tag{F.7}$$

This hybrid version of the Maxwell-Garnett formula has been tested and works well with mixtures of water-sugar-salt that are commonly used when simulating human tissue [74].

Bibliography

[1] C. Brunckhorst, R. Candinas, and S. Furman, "Obituary: Ake Senning1915-2000," *Journal of Pacing and Clinical Electrophysiology*, vol. 23, Nov. 2000.

[2] S. Furman, "The early history of cardiac pacing," *Pace*, vol. 26, pp. 2023–2032, Oct. 2003.

[3] W. Greatbatch, *The Making of the Pacemaker*. Prometheus Books, 2000.

[4] J. G. Webster, ed., *Design of Cardiac Pacemacers*. IEEE Press, 1995.

[5] "Organisation website." http://trc.telemed.org, 2004. Telemedicine Research Center.

[6] "Company website." http://www.biotronik.com. BIOTRONIK GmbH and Co.

[7] J. Cavuoto, "Neural engineering's image problem," *IEEE Spectrum*, Apr. 2004.

[8] "Company website." http://www.medtronic.com. Medtronic Inc.

[9] R. F. Weir, P. R. Troyk, G. DeMichele, and T. Kuiken, "Implantable myoelectric sensors (IMES) for upper-extremity prosthesis control," *Engineering in Medicine and Biology Society, 2003. Proceedings of the 25th Annual International Conference of the IEEE*, pp. 1562–1565, sep 2003.

[10] "Company website." http://www.cyberkineticsinc.com, 2004. Cyberkinetics Inc.

[11] R. Buchner, J. Barthel, and J. Stauber, "The dielectric relaxation of water between 0C and 35C," *Chem. Phys. Letters*, vol. 306, no. 1-2, 1999.

[12] C. Gabriel, "Compilation of the dielectric properties of body tissues at RF and microwave frequencies," technical report AL/OE-TR-1996-0037, Brooks Air Force.

[13] "ETSI website." http://www.etsi.org. European Telecommunication Standards Institute.

[14] European Telecommunications Standards Institute, *ETSI EN 301 839-1 Electromagnetic compatibility and Radio spectrum Matters (ERM);Radio equipment in the frequency range 402 MHz to 405 MHz for Ultra Low Power Active Medical Implants and Accessories;Part 1: Technical characteristics, including electromagnetic compatibility requirements, and test methods.*, 2002.

[15] International Telecommunication Union, *Recommendation ITU-R SA.1346*, 1998.

[16] "Planning for medical implant communications systems (MICS) and related devices," Proposals Paper SPP 6/03, Australian Communications Authority.

[17] European Telecommunications Standards Institute, *ETSI EN 300 328-1 Electromagnetic compatibility and Radio spectrum Matters (ERM); Wideband transmission systems; Data transmission equipment operating in the 2.45 GHz ISM band and using wide band modulation techniques; Harmonized EN covering essential requirements under article 3.2 of the RTTE Directive.*, Mar. 2004.

[18] Y. Porat, A. Penner, and E. Doron, "US Pat. No. 6,432,050 implantable acoustic bio-sensing system and method," 1999. USPTO.

[19] E. Doran and A. Penner, "US Pat. No. 6,486,588 acoustic biosensor for monitoring physiological conditions in a body implantation site," 2002. USPTO.

[20] R. W. Tennent and W. J. Fitzgerald, "Passband complex fractionally-spaced equalization of MSK signals over the mud pulse telemetry channel.," *Signal Processing Advances in Wireless Communications, 1997 First IEEE Signal Processing Workshop on*, pp. 5–8, apr 1997.

[21] "Company website." http://www.guidant.com, 2004. Guidant.

[22] "World Medical Association Declaration of Helsinki: Ethical Principles for Medical Research Involving Human Subjects." http://www.wma.net, 2000. WORLD MEDICAL ASSOCIATION.

[23] T. D. Fåhreus. Personal Communicatoin. Lund University Hospital, Lund, Sweden.

[24] G. Hartsgrove, A. Kraszewski, and A. Surowiec, "Simulated biological materials for electromagnetic radiation absorption studies," *Bioelectromagnetics*, no. 8, pp. 29–365, 1987.

[25] M. Bini, A. Ignesti, L. Millanta, R. Olmi, R. Rubino, and R. Vanni, "The polyacrylamide as a phantom material for electromagnetic hyperthermia studies," *IEEE Trans. on Biomedical Engineering*, vol. BME-31, Mar. 1984.

[26] S. Shibuya, *A Basic Atlas of Radio-Wave Propagation.* John Wiley and Sons, 1987.

[27] R. Pettai, *Noise in Reciving Systems.* John Wiley and Sons, 1984.

[28] C. A. Balanis, *Antenna Theory.* John Wiley and Sons, Inc., 2nd ed., 1982.

[29] R. Vaughan and J. B. Andersen, *Channels, Propagationa and Antennas for Mobile Communications.* Institution of Electrical Engineers, London, 2003.

[30] J. A. kong, *Electromagnetic Wave Theory.* John Wiley and Sons, 1986.

[31] R. W. P. King and S. G. S., *Antennas in Matter.* the MIT Press, 1981.

[32] P. Köpf-Maier, *Atlas of Human Anatomy.* Karger, 5th ed., 2000.

[33] A. H. Durney and D. A. Christen, *Basic Introduction to Bioelectromagnetics.* CRC Press, 1999.

[34] K. Fujimoto and J. R. James, eds., *Mobile Antenna Systems Handbook.* Artech House, London, 2nd ed., 2001.

[35] "Specification of the Bluetooth system (core) 1.1." http://www.bluetooth.com, Feb. 2001. Bluetooth SIG.

[36] M. S. Gast, *802.11 Wireless Networks - the Definitive Guide.* O'Reilly, 1st ed., 2002.

[37] R. W. P. King, S. Prasad, and B. H. Sandler, "Transponder antennas in and near a three-layered body," *IEEE Trans. on Microwave theory and Techniques*, vol. MTT-28, pp. 586–596, June 1980.

[38] J. D. Kraus, *Antennas.* McGraw-Hill, 1988.

[39] P.-S. Kildal, *Foundations of Antennas.* Studentlitteratur, 2000.

[40] R. C. Johnson, ed., *Antenna Engineering Handbook.* McGraw-Hill, Inc., 3rd ed., 1993.

[41] R. C. Hansen, "Radiation and reception with buried and submerged antennas," *IEEE Trans. Antennas and Propagation*, pp. 207–216, May 1963.

[42] "Submarine antenna systems." http://www.sippican.com, 2004. Sippican Inc.

[43] M. Annati, "Mine hunting and mine clearing revisited," *Military Technology*, vol. XXVII, no. 8-9, 2003.

[44] C. Furse, "Design of an antenna for pacemaker communication," *Microwaves and RF*, pp. 73–76, 2000.

[45] W. Sun, G. Haubrich, and G. Dublin, "US Pat. No. 5,861,091 implantable medical device microstrip telemetry antenna," 1999.

[46] M. D. Amundson, J. A. Von Arx, W. J. Linder, P. Rawat, and W. R. Mass, "US Pat. No. 6,456,256 circumferenctiual antenna for an implantable medical device," 2002. USPTO.

[47] J. A. Von Arx, W. R. Mass, S. T. Mazar, and M. D. Amundson, "US Pat. No. 6,708,065 antenna for an implantable pacemaker," 2004. USPTO.

[48] R. S. Mackay, *Bio-Medical Telemetry*. John Wiley and Sons, Inc., 1st ed., 1968.

[49] C. A. Caceres, ed., *Biomedical Telemetry*. Academic Press, 1965.

[50] "Product catalogue." http://www.atstrack.com, 2004. Advanced Telemtry Sytemss, Inc.

[51] R. K. Moore, "Effects of a surrounding conducting medium on antenna analysis," *IEEE trans. on Antennas and Propagation*, vol. 11, May 1963.

[52] A. Karlsson, "Physical limitations of antennas in a lossy medium," *IEEE trans. on Antennas and Propagation*, vol. In press, 2004.

[53] R. F. Harrington, *Time Harmonic Electromagnetic Fields*. McGraw-Hill, 1961.

[54] R. s. Mackay, *Bio-Medical Telemetry*. IEEE Press, 2nd ed., 1993.

[55] "Company website." http://www.speag.com, 2004. Schmid and Partner Engineering AG.

[56] N. Chavannes, R. Tay, N. Nikoloski, and N. Kuster, "Suitability of fdtd-based TCAD tools for RF design of mobile phones," *IEEE Antennas and Propagation Magazine*, pp. 52–66, Dec 2003.

[57] J. D. Kraus, *Electromagnetics*. Mc Graw Hill, 4th ed., 1992.

[58] R. C. Fenwick and W. L. Weeks, "Submerged antenna characteristics," *IEEE Trans. on Antennas and Propagation*, vol. 11, May 1963.

[59] G. A. Deschamps, "Impedance of an antenna in a conducting medium," *IEEE Trans. on Antennas and Propagation*, vol. 10, Sept. 1962.

[60] D. Andreuccetti, M. Bini, A. Ignesti, R. Olmi, S. Priori, and R. Vanni, "High permittivity patch radiator for single and mulit-element hyperthermia applicators," *IEEE trans. on Biomedical Engineering*, pp. 711–715, July 1993.

[61] W. Stutzman and G. Thiele, *Antenna theory and design*. John Wiley and Sons, 1998.

[62] "SEMCAD: addendum to the reference manual," manual, Shmid and Partner Engineering AG., 2004.

[63] "Mobiltelefoner och strålning," tech. rep., Swedens Radiation Protection Authority, 2003.

[64] "Proposed changes ion the comission's rules regarding human exposure to radiofrequency electromagnetic fileds.," tech. rep., Federal Communications Commission, USA, 2003.

[65] W. G. Scanlon, J. B. Burns, and N. E. Evans, "Radiowave propagation from a tissue-implanted source at 418 mhz and 916.5 mhz.," *IEEE trans. on Biomedical Engineering*, pp. 527–534, April 2000.

[66] A. Taflove, *Computational Electrodynamics*. Artech House, London, 1995.

[67] "The visible human project." http://www.nlm.nih.gov/research/visible/, 2004. United States National Librarty of Medicine.

[68] A. M. Skunidin, S. A. Fateev, and T. L. Kulova, "Battery for cardiac pacemaker: an alternative to lithium-iodine system," *Advanced Batteries and Accumulators*, vol. II, May 2001.

[69] C. E. Shannon and W. Weaver, *The Mathematical Theory of Communication*. University of Illinois Press, 1998.

[70] B. Sonesson and G. Sonesson, *Anatomi och Fysiologi*. Liber, 1993.

[71] K. D. Cheng, *Field and Wave Elecromagnetics*. Addison-Wesley Publishing Company, Inc., 2nd ed., 1989.

[72] M. Abramovitz and I. A. Stegun, eds., *Handbook of Mathematical Functions with Formulas, Graphs, and Mathematical Tables*. Dover Pubns., 1965.

[73] A. Sihvola, *Electromagnetic Mixing Formulas and Applications*. the Institution of Electrical Engineers, London, 1999.

[74] M. Kvistholm and V. Cukalevski, "Hybrid mixing model for biological tissue equivalent materials," Master's thesis, Dept. of Electroscience, Lund University.